Numerical study of wind farm gravity waves: Impact of wind farm configuration

Final Thesis

Bas Comuth

Faculty of Aerospace Engineering
Department of Wind Energy

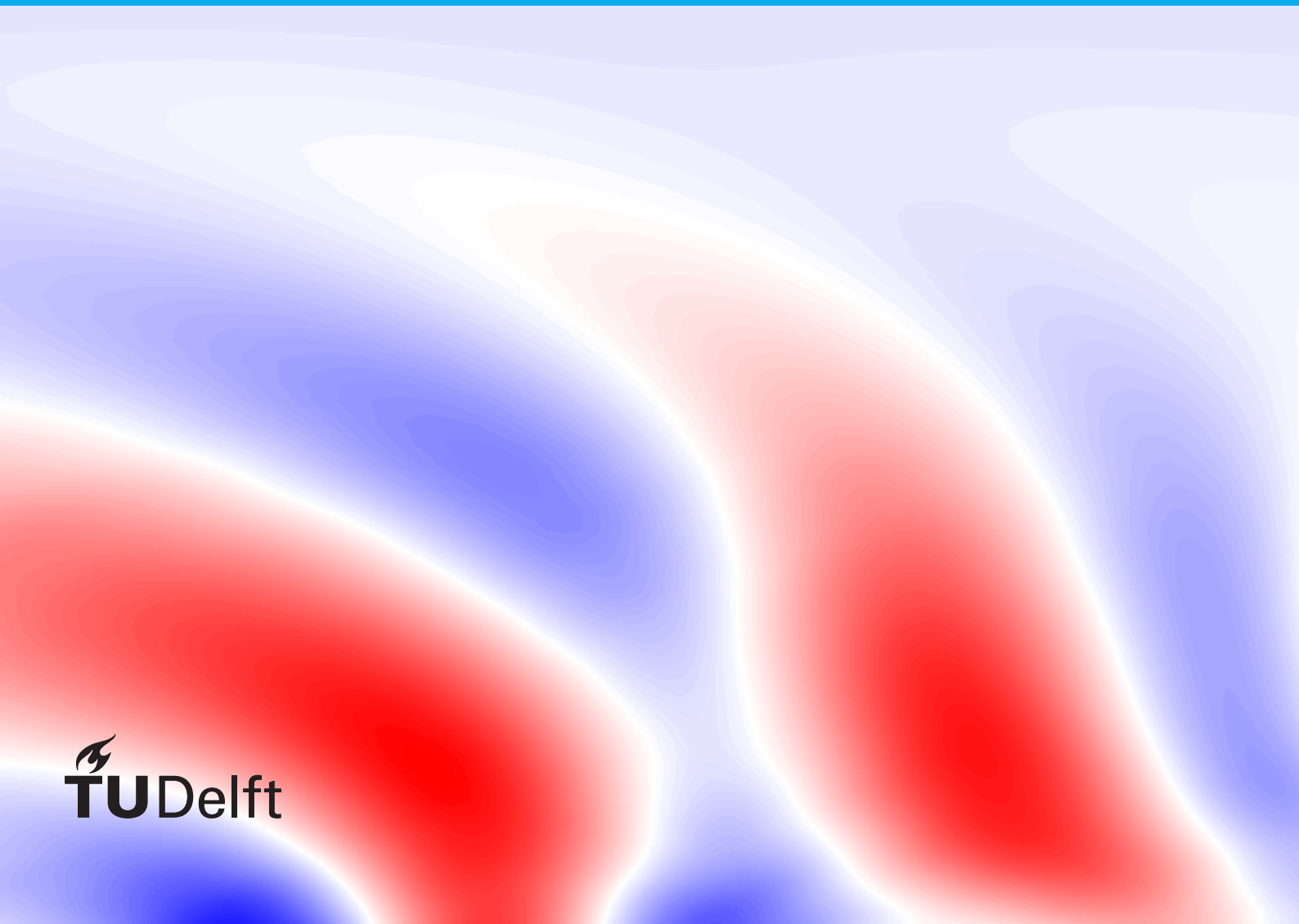

TU Delft

Numerical study of wind farm gravity waves: Impact of wind farm configuration

Final Thesis

by

Bas Comuth

to obtain the degree of Master of Science
at the Delft University of Technology,
to be defended publicly on February 7, 2025 at 15:00.

Student number:	4784626	
Project duration:	March 4, 2024 – February 7, 2025	
Thesis committee:	Prof. dr. ir. S.J. Watson,	TU Delft, supervisor
	Prof. dr. ir. D.A. von Terzi,	TU Delft, chairperson
	Prof. dr. ir. S. Hickel	TU Delft, external examiner
Supervision:	Prof. dr. ir. S.J. Watson,	
	Ir. M.A. Khan,	
	Ir. U.C. Krishnan Paranjothi	

TU Delft

Preface

This thesis is written in fulfilment of the Master's degree in Aerodynamics at the Delft University of Technology. It is the culmination of ten months of researching and simulating wind farms. I hope this thesis will inspire future students to pursue research in atmospheric gravity waves, as it is an exciting new field, and consequently contribute to the field of wind energy. Furthermore, I hope this thesis will be useful to the scientific community, and ultimately contribute to a more sustainable world.

The reader is assumed to have knowledge of (computational) fluid dynamics, specifically applied to wind turbines. For those who are looking to deepen their knowledge of mesoscale phenomena, such as atmospheric gravity waves, in relation to wind farms, Chapter 2 might be of particular interest. Readers interested in simulating atmospheric gravity waves are referred to the methodology in Chapter 4, where the novel Multi-Scale Coupled model and TOSCA framework for Large Eddy Simulations are discussed. Finally, anyone curious about the takeaways and exploratory guidelines derived from this study is advised to consult the results and conclusions in Chapter 5 and Chapter 6 respectively.

It goes without saying that this research was not possible on my own, which is why I owe a debt of gratitude to the people in my academic and personal life who helped me complete this work. First of all, I would like to thank Simon Watson for his supervision and guidance. Furthermore, I am grateful to Mehtab Ahmed Khan, and Udhaya Chandiran Krishnan Paranjothi for the many fruitful discussions, as well as for letting me use their experience in simulating wind farms in atmospheric gravity waves. Next, I am indebted to Sebastiano Stipa and Joshua Brinkerhoff for allowing me to use their innovative Multi-Scale Coupled model and TOSCA framework, and for being available for any questions. Finally, I appreciate the generous computational resources the team of the Delft High-Performance Computing Center has provided me with (Delft High Performance Computing Centre (DHPC), 2024).

To conclude my acknowledgements, I want to deeply thank my friends and family, especially Fleur, Luuk, Marc, Suzan, Sandra, Frank, Pim, Mees, Cairo, Huub, Moos, and Peer, for their support and company, and for helping me maintain my work-life balance.

Bas Comuth
Venlo, January 10, 2025

Abstract

The recent growth of the size of wind farms highlights the need for a deeper understanding of the mesoscale phenomena in a stably stratified atmosphere, such as atmospheric gravity waves, as the effect on the power generation can be significant. This thesis is a numerical study of the effect of wind farm layout on atmospheric gravity wave excitation and the resulting feedback on wind farm performance. Wind farms in this study have varying power density, streamwise or spanwise turbine spacing, aspect ratio, hub height, rotor diameter, shape, or orientation with respect to the freestream, and are situated in a conventionally neutral boundary layer in offshore conditions. Moreover, the wind farms can be horizontally or vertically staggered. To investigate the atmospheric gravity wave excitation, the effect of wind farm layout on the Froude number and inversion Froude number governing the internal and interfacial waves respectively is studied using several high-fidelity Large Eddy Simulations. Then, AGW wavelength and wind farm efficiency are parametrically studied using a fast reduced-order model. Specifically, the non-local efficiency is considered, which is a measure of the global blockage effect induced by the atmospheric gravity waves. It is found that the length scale used in the Froude number must be adjusted to the wind farm, and is dependent on the turbine spacing and farm shape. The inversion Froude number is based on the phase speed of the interfacial waves. It is suggested that the phase speed must be based on shallow-water theory and deep-water theory for small and large turbine spacings respectively. In other words, for small turbine spacings the wind farm acts as an entity, while for large turbine spacings, the farm acts as a collection of individual turbines. Finally, the streamwise and spanwise turbine spacing (and consequently the power density), and the aspect ratio primarily govern the non-local efficiency.

Keywords: Atmospheric Gravity Waves, Wind Farm Layout, Froude Number, Large Eddy Simulation, Multi-Scale Coupled Model

List of Figures

List of Tables

Nomenclature

Roman Symbols

A	Farm surface area	$[\mathrm{m}^2]$
AR	Aspect ratio	[-]
c'_{ft}	Disk-based wind farm planform thrust coefficient	[-]
C_P	Power coefficient	[-]
c_p	Specific heat capacity at constant pressure	$[\mathrm{J\,K^{-1}\,kg^{-1}}]$
C_T	Thrust coefficient	[-]
D	Rotor diameter	[m]
D_{hub}	Hub diameter	[m]
d_{hub}	Hub overhang	[m]
f_c	Coriolis parameter	$[\mathrm{s^{-1}}]$
Fr	Free atmospheric Froude number	[-]
Fr_i	Inversion Froude number	[-]
$Fr_{i,dw}$	Deep-water inversion Froude number	[-]
g	Gravitational acceleration	$[\mathrm{m\,s^{-2}}]$
g'	Reduced gravity	$[\mathrm{m\,s^{-2}}]$
H	Capping inversion height	[m]
H_1	Wind farm layer height	[m]
H_2	Upper layer height	[m]
h_{hub}	Hub height	[m]
k	Wavenumber	$[\mathrm{m^{-1}}]$
L	Characteristic length scale	[m]
$L_{f_\varnothing}$	Farm diameter	[m]
L_{f_x}	Farm length	[m]
L_{f_y}	Farm width	[m]
N	Brunt-Väisälä frequency	$[\mathrm{s^{-1}}]$
N_t	Number of turbines	[-]
N_{t_x}	Number of turbine rows	[-]
N_{t_y}	Number of turbine columns	[-]
P_1	(Average) first-row turbine power	[W]
$p_{(ref)}$	(Reference) Pressure	[Pa]
P_{rated}	Rated power	[W]

P_{total}	Total farm power	[W]
P_{th}	Theoretical turbine power	[W]
R	Gas constant of air	$[\mathrm{J\,K^{-1}\,kg^{-1}}]$
S_e	Equivalent turbine spacing	[m]
s_x	Streamwise non-dimensional turbine spacing	[-]
s_y	Lateral/Spanwise non-dimensional turbine spacing	[-]
U	Streamwise velocity	$[\mathrm{m\,s^{-1}}]$
U'	Streamwise perturbation velocity	$[\mathrm{m\,s^{-1}}]$
U_1	Streamwise wind farm layer wind speed	$[\mathrm{m\,s^{-1}}]$
U_2	Streamwise upper layer wind speed	$[\mathrm{m\,s^{-1}}]$
$u_\star$	Friction velocity	$[\mathrm{m\,s^{-1}}]$
U_B	Bulk velocity in the inversion layer	$[\mathrm{m\,s^{-1}}]$
U_g	Streamwise geostrophic wind speed	$[\mathrm{m\,s^{-1}}]$
U_{bk}	Streamwise background velocity	$[\mathrm{m\,s^{-1}}]$
U_{ref}	Reference velocity at hub height	$[\mathrm{m\,s^{-1}}]$
V	Lateral/Spanwise velocity	$[\mathrm{m\,s^{-1}}]$
V'	Lateral/Spanwise perturbation velocity	$[\mathrm{m\,s^{-1}}]$
V_1	Lateral/Spanwise wind farm layer wind speed	$[\mathrm{m\,s^{-1}}]$
V_2	Lateral/Spanwise upper layer wind speed	$[\mathrm{m\,s^{-1}}]$
V_g	Lateral/Spanwise geostrophic wind speed	$[\mathrm{m\,s^{-1}}]$
W	Vertical velocity	$[\mathrm{m\,s^{-1}}]$
x	Streamwise coordinate	[m]
y	Lateral/Spanwise coordinate	[m]
z	Height/Wall-normal coordinate	[m]
z_0	Surface roughness length	[m]

Greek Symbols

α_{lin}	Direction of the characteristic lines associated with the inversion Froude number	[°]
β	Direction of the internal wavetrains	[°]
ΔH	Capping inversion thickness	[m]
$\Delta\theta$	Capping inversion strength	[K]
η_1	Wind farm layer displacement	[m]
η_2	Upper layer displacement	[m]
η_f	Farm efficiency	[-]
η_w	Wake efficiency	[-]
$\eta_{(t)}$	(Total) Capping inversion displacement	[m]
η_{nl}	Non-local efficiency	[-]

Γ	Free atmospheric lapse rate	$[\mathrm{K\,m^{-1}}]$
γ_{lin}	Direction of the characteristic lines associated with the deep-water inversion Froude number	[°]
κ	Von Kármán constant	[-]
λ	Wavelength	$[\mathrm{m}]$
ν	Kinematic viscosity	$[\mathrm{m^2\,s^{-1}}]$
ν_t	Eddy viscosity	$[\mathrm{m^2\,s^{-1}}]$
Φ	Orientation	[°]
Π	Power density	$[\mathrm{W/m^2}]$
ψ	Horizontal staggering angle	[°]
ρ	Air density	$[\mathrm{kg\,m^{-3}}]$
τ_x	Streamwise shear stress	[Pa]
τ_y	Lateral/Spanwise shear stress	[Pa]
$\theta_{(0)}$	(Reference) potential temperature	[K]
$\tilde{\psi}$	Non-dimensional horizontal staggering angle	[-]

Abbreviations

3LM(R)	Three-Layer Model (Reconstruction)
ABL	Atmospheric Boundary Layer
ADL	Advection Damping Layer
ADM	Actuator Disk Model
AGW	Atmospheric Gravity Wave
ALM	Actuator Line Model
CFD	Computational Fluid Dynamics
CFL	Courant-Friedrichs-Lewy
CIH	Capping Inversion Height
CIS	Capping Inversion Strength
CIT	Capping Inversion Thickness
CNBL	Conventionally Neutral Boundary Layer
DNS	Direct Numerical Simulation
FALR	Free-Atmospheric Lapse Rate
IGW	Internal Gravity Wave
LES	Large Eddy Simulation
MSC	Multi-Scale Coupled
NBL	Fully Neutral Boundary Layer
OFAT	One-Factor-At-a-Time
RANS	Reynolds-Averaged Navier-Stokes
RDL	Rayleigh Damping Layer
SBL	Stable Boundary Layer
TGW	Trapped Gravity Wave
TOSCA	Toolbox fOr Stratitied Convective Atmospheres

Contents

1 Introduction

Although the generation of electricity from the wind was already possible for almost a century since the first wind turbine by Josef Friedländer (Bruyerre, 2022), the installation of the first onshore wind farm in 1980 in the United States (University of Massachusetts Amherst, 2023) and the first offshore wind farm (Vindeby) in 1991 off the coast of Denmark (Ørsted, 2019) marked the beginning of commercial energy generation through wind farms. In the 1980s, the incentive for wind energy came from the oil crisis (Zaaijer and Viré, 2023). On the contrary, in recent history, the incentive for wind energy has changed, recognizing the need for renewable energy to limit climate change. An example of this is the Paris Agreement signed in 2016, an international treaty aimed at limiting the rise of global surface temperature to two degrees or less.

Evidently, (offshore) wind energy plays a major role in the plans made by the parties in the treaty. Compared to the 5 MW capacity of the Vindeby wind farm, the total installed capacity of offshore wind energy of 64 GW in 2023 (GWEC, 2023) is already an enormous growth. This growth is achieved not only through the construction of additional wind farms but also by the increase in the size of the wind farms and the wind turbines themselves. Both wind farm size (Interreg NorthSEE, 2020), and wind turbine size (hub height and rotor diameter, Hartman, 2023) show clear trends in size. Moreover, Interreg NorthSEE, 2020 shows that offshore wind farms move further offshore to deeper waters.

However, the first evaluation of the progress towards the Paris Agreement, which was concluded in 2023, shows that insufficient progress is made, such that at the current rate the goals will not be met (UNFCCC secretariat, 2023). Therefore, it is essential that, next to bigger turbines and farms, the efficiency of a wind farm is as high as possible. The increase in the size of wind farms gives rise to new challenges concerning farm efficiency, as the flow in and around these farms is entering new domains in which mesoscale effects start to have an influence. More research is needed to explore the space of parameters that influence the power output of large wind farms, and it is precisely this area the current study falls into. Not only does the research allow for more accurate power prediction and give insight into the influence of certain parameters, but it will also open the possibility of tailoring the design of large wind farms to the mesoscale phenomena in the atmosphere.

The present chapter serves to define the research as introduced above. To do so, the research scope is presented in Section 1.1, highlighting what parameters will be studied in what conditions. Subsequently, the relevance of the research is demonstrated in Section 1.2. Finally, the remainder of the report will be outlined in Section 1.3.

1.1. Research Scope

The mesoscale phenomena that this study focuses on are wind farm-induced atmospheric gravity waves, an introduction to which will be given in Chapter 2. The study aims to improve the understanding of the interaction between (wind farm-induced) atmospheric gravity waves and wind farms, specifically offshore wind farms in conventionally neutral boundary layers (CNBL). To this end, low- and high-fidelity numerical methods are utilized, in order to have a large parameter space on the one hand, and a high level of detail for some cases on the other hand. The study is not site-specific but rather tries to investigate all parameters that together make up the layout of a wind farm. The practical scope is that the study investigates some preliminary exploratory guidelines for wind farm design. The atmospheric state is constant and is deemed to be representative of offshore conditions.

1.2. Relevance

It is quickly realised that accurately predicting the power of a wind farm with maximized efficiency is a desirable outcome of the research. However, the impact of atmospheric gravity waves on the performance of wind farms as a result of their configuration (e.g. layout or shape) still needs to be quantified, thus justifying the relevance of the present study. After all, a large power output improvement is an economic incentive. The study by Allaerts et al., 2018 investigates the annual impact of atmospheric gravity waves on the Belgian-Dutch offshore wind farm cluster. It is found that the annual energy loss for the cluster due to atmospheric gravity waves is between 4 to 6%, a significant amount. Therefore, there is an opportunity to reduce this number by investigating the impact as a result of the wind farm layout. Moreover, the potential of investigating the wind farm layout is already recognized by many research, such as Allaerts and Meyers, 2018, S. J. Ollier et al., 2018, Lanzilao and Meyers, 2021, S. Ollier, 2022, S. J. Ollier and Watson, 2023, Lanzilao and Meyers, 2024, and Stipa, Ahmed Khan, et al., 2024.

1.3. Outline

The remainder of this thesis is structured as follows. Chapter 2 will introduce the main concepts around which the current study revolves. The theoretical background of atmospheric gravity waves in the atmosphere, atmospheric boundary layers, and ways of numerically modelling and simulating large wind farms will be provided. Next, Chapter 3 will review the existing body of literature to chronologically demonstrate the existing research gap. From this research gap, research questions will follow, which the conclusions in Chapter 6 try to answer. The conclusions are preceded by the methodology in Chapter 4, where the atmospheric state, wind farm layouts, wind turbines, and modelling and simulation methods are discussed in detail, and the results in Chapter 5, accompanied with a discussion of said results.

2

Theoretical Background

In the present chapter, the concepts related to atmospheric gravity waves, different types of atmospheric boundary layers, and numerical modelling and simulation of wind farms, specifically related to AGWs, are introduced in Section 2.1, Section 2.2, and Section 2.3. Thus, this chapter serves as a theoretical background for the variables and concepts that are heavily used throughout the remainder of this report. Here, the main sources of information will be Nappo, 2013 and Stull, 1988, although there are many textbooks on the subject, such as Gossard and Hooke, 1975, Gill, 1982, Baines, 1998, and Sutherland, 2010.

2.1. Atmospheric Gravity Waves in the Atmosphere

First and foremost, it is important to understand what an atmospheric gravity wave (AGW) is. Atmospheric gravity waves are mesoscale oscillations in the atmosphere. Typical length scales for mesoscale phenomena are $2\,\mathrm{km}$ to $200\,\mathrm{km}$, as defined in Stull, 1988. Firstly, a disturbance needs to give an air parcel a displacement from its original position in the direction opposite to that of gravity. This is the case when the flow encounters for example mountains, hills, thunderstorms, or wind farms (Nappo, 2013). After the displacement, in a stratified atmosphere, a buoyancy force will act as the restoring force due to the density or potential temperature gradient. The potential temperature is the temperature of the air parcel if it were brought to a reference pressure adiabatically, as seen in Equation 2.1 (Nappo, 2013). Usually, the reference pressure is $100\,\mathrm{kPa}$. Furthermore, R is the gas constant of air and c_p is the specific heat capacity of air at constant pressure.

$$\theta = \left(\frac{p_{ref}}{p}\right)^{\frac{R}{c_p}} \tag{2.1}$$

Even though the waves are called gravity waves, gravity is not the restoring force. Rather, it is a requirement for stratification. As such, gravity waves would not exist without gravity, but it is the buoyancy force that is essential to the wave-like motion. If the potential temperature increases with height, the buoyancy force will counter the initial displacement, creating a wave-like motion, corresponding to a stable atmosphere. If the buoyancy force is in the other direction, the movement is diverging, corresponding to an unstable atmosphere.

Atmospheric gravity waves relevant to the present study are categorized into two categories: internal and interfacial waves. Internal waves are supported by a continuously stratified fluid, which in this case is the atmosphere having a certain free atmospheric lapse rate ($\Gamma = d\theta/dz$, where z is the direction normal to the ground). The internal gravity waves in the free atmosphere can propagate upwards and downstream. Secondly, interfacial waves occur when there is a discrete jump in the stratification, for example at the interface between two different fluids. However, as discussed in Section 2.2, there are locations in the atmosphere where the potential temperature gradient sharply changes. Interfacial waves will travel along this interface. A useful parameter for internal waves is the Brunt-Väisälä frequency, sometimes called the buoyancy frequency. It is a measure of the stability of the free atmosphere and represents the maximum supported frequency of the internal wave if it were propagating fully vertically. It is not necessarily the frequency of the wave itself, as that is dependent on the propagation direction. Its definition is presented in Equation 2.2. Note that for an unstable atmosphere, i.e. $d\theta/dz < 0$, the Brunt-Väisälä frequency is imaginary.

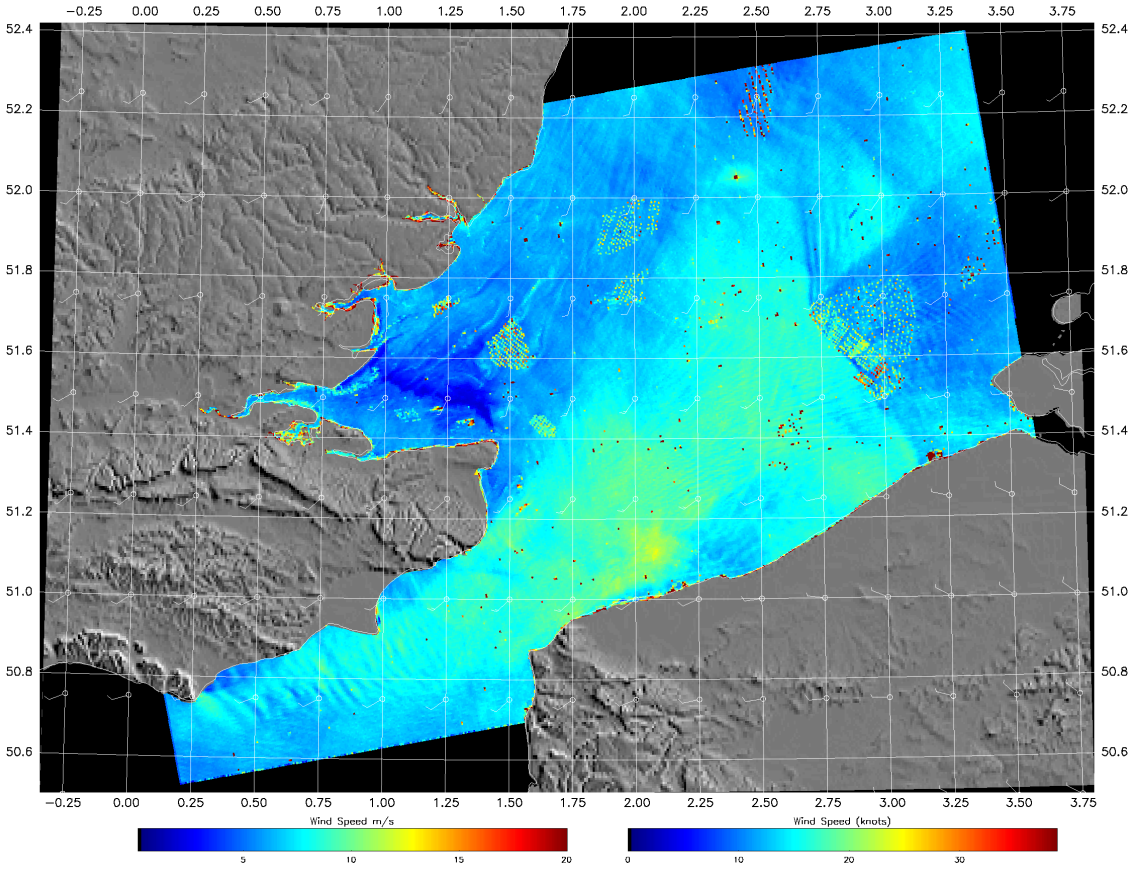

Figure 2.1: Instantaneous velocity field over the North Sea and Strait of Dover determined via satellite imagery. Atmospheric gravity waves induced by wind farms as well as topography are clearly visible in the bottom left and top right of the image. Reproduced from Davis, N. N., Badger, J., Hahmann, A. N., Hansen, B. O., Mortensen, N. G., Kelly, M., Larsén, X. G., Olsen, B. T., Floors, R., Lizcano, G., Casso, P., Lacave, O., Bosch, A., Bauwens, I., Knight, O. J., van Loon, A. P., Fox, R., Parvanyan, T., Hansen, S. B. K., … Drummond, R. (2023). The Global Wind Atlas: A High-Resolution Dataset of Climatologies and Associated Web-Based Application. https://doi.org/10.1175/BAMS-D-21-0075.1 This figure is licensed under a Creative Commons Attribution 4.0 International License.

$$N = \sqrt{\frac{g}{\theta_0}\frac{d\theta}{dz}} \tag{2.2}$$

Interfacial waves can either be subcritical, critical, or supercritical. In these cases, their propagation speed is either higher, equal, or lower respectively than the background velocity of the flow. Consequently, the disturbances induced by interfacial waves can only travel upstream in the subcritical case.

Atmospheric gravity waves on themselves are not visible, but the perturbations they induce can be, for example in the velocity field, as shown in Figure 2.1. Here, the instantaneous velocity field over the Strait of Dover and the North Sea is visualized by measuring the roughness of the sea using satellite imagery (Davis et al., 2023). Atmospheric gravity waves induced both by wind farms and topography are clearly visible in the top right and bottom left of the picture respectively.

2.2. Atmospheric Boundary Layers and the Free Atmosphere

As previously discussed, the potential temperature gradients in the atmosphere support the formation of the atmospheric gravity waves. It is therefore useful to discuss where the potential temperature gradients exist in the atmosphere. Close to the surface, there is the atmospheric boundary layer (ABL), which is the region where the flow is influenced by the Earth's surface in a time scale of an hour or less (Stull, 1988). The type of boundary layer is determined by the potential temperature gradient and can be either stable ($d\theta/dz < 0$), neutral ($d\theta/dz = 0$), or unstable or convective ($d\theta/dz > 0$). However, the boundary classifications do not take into account the stratification of the free atmosphere, which is why the terms truly neutral and conventionally neutral are introduced by Zilitinkevich and Esau, 2002. Here, the free atmosphere is neutral or stably strat-

ified respectively. The neutral boundary layer is of most interest since it often occurs in offshore conditions. Although a truly neutral case is an idealised case that does not exist in practical conditions (Hess, 2004), the conventionally neutral boundary layer (CNBL) does represent real offshore conditions (Allaerts, 2016). In the case of a CNBL, the height of the atmospheric boundary layer is clearly defined due to the presence of a thin layer with a strong potential temperature gradient, called the capping inversion (Allaerts, 2016). Due to this strong gradient, perturbations through the capping inversion are limited, thus explaining the clear definition of the boundary layer height. The CNBL is schematically visualised in Figure 2.2. The velocity profile shows the logarithmic profile at the surface and the characteristic Ekman spiral in the boundary layer due to the influence of friction. Furthermore, above the capping inversion, the flow is geostrophic, as a result of the balance between the Coriolis force and the pressure gradient (Allaerts, 2016). The potential temperature profile defines the different layers. First of all, the boundary layer is neutral, and thus the potential temperature does not change. Then, the sharp change represents the capping inversion. The jump in potential temperature is its strength (CIS). Furthermore, the capping inversion has a certain height and thickness (CIH and CIT). Finally, the atmosphere is stably stratified, having a certain free atmospheric lapse rate, which usually differs from the potential temperature gradient in the capping inversion. It can thus be observed that there is also a jump in the potential temperature *gradient*, establishing the conditions under which interfacial waves can occur.

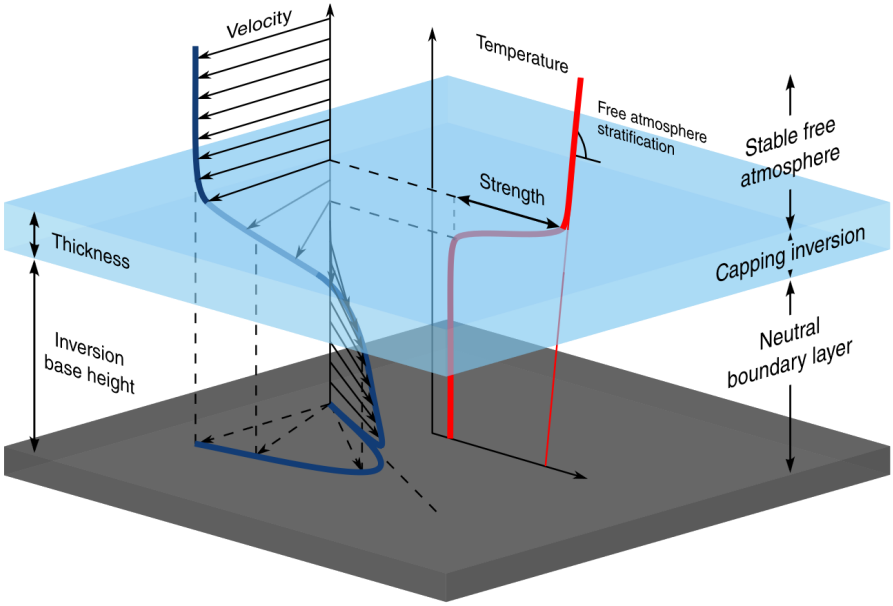

Figure 2.2: Three-dimensional velocity and potential temperature profiles of the conventionally neutral boundary layer. Based on the potential temperature profile, the neutral boundary layer, capping inversion, and free atmosphere can be identified. In the velocity profile, the Ekman spiral and logarithmic profile near the surface are clearly visible. Reprinted from Allaerts, D., & Meyers, J. (2015). Large eddy simulation of a large wind-turbine array in a conventionally neutral atmospheric boundary layer. *Physics of Fluids*, *27*(6) with the permission of AIP Publishing.

2.3. Numerical Modelling and Simulation of Wind Farms

The numerical modelling and simulation of wind farms can be done in many ways, at many different levels of fidelity. Simulating the interaction between wind farms and atmospheric gravity waves gives rise to many challenges, as discussed in Stipa, Ajay, et al., 2024a and Shaw et al., 2022. For instance, there is a huge range of length scales involved, and waves will reflect at the boundaries. The many different approaches for modelling and simulation range from fast reduced-order models to computational fluid dynamics (CFD) simulations. The latter can have vastly different computational requirements, depending on the level of turbulence being resolved. To deal with turbulence, there are three main categories, being Reynolds-Averaged Navier-Stokes simulations (RANS), Large Eddy Simulations (LES), and Direct Numerical Simulations (DNS). For more information on the workings of the different frameworks, the reader is referred to a CFD textbook, for instance, Wilcox, 2006. Although all methods have been applied to wind farms successfully (see for example S. Ollier, 2022, Allaerts, 2016, and Johnstone and Coleman, 2012 respectively), the majority of studies uses LES, as will become apparent in Chapter 3. Mainly, LES is deemed to be a good trade-off between computational resources and fidelity, allowing for the LES results to be used for reduced-order model validation. Furthermore, LES gives the transient solution of a physical problem, which is useful for studying atmospheric gravity waves.

3

Literature Review

The present chapter reviews the existing body of literature related to the research area discussed in Chapter 1. The review will take a chronological approach, in order to arrive at the current state of research and the resulting research gap. To do so, the wake effects of wind farms are discussed in Section 3.1. Then, the interaction between the atmospheric boundary layer and the wind farm is discussed in Section 3.2. The excitation of atmospheric gravity waves by this interaction or other factors is discussed in Section 3.3. Next, the influence of atmospheric gravity waves excited by topography on wind farms is investigated in Section 3.4. Finally, the feedback effect on the wind farm of self-induced atmospheric gravity waves is discussed in Section 3.5.

3.1. Wake Effects of Wind Farms

As discussed before, the world's total wind energy generation has grown significantly recently. This growth is not only achieved by installing more wind farms, wind farms themselves are containing more and bigger wind turbines. It is therefore vital to study the interaction between individual (groups of) wind turbines, to maximize the farm's power output. The field of wind farm wake effects is concerned with investigating these interactions, specifically the interaction between a turbine and the wake of an upstream turbine. It is generally agreed that the inclusion of wakes in the analysis of the wind farm power output will yield a lower output than the summation of the power outputs of the individual turbines. The present section serves to demonstrate the (ongoing) field of research dedicated to studying wind farm aerodynamics, highlighting the different methodologies.

There are many different ways to study the effect of the interaction between turbines, with different levels of fidelity. Barthelmie et al., 2009 evaluates different wind farm and wake models of different levels of fidelity, and compares them with data from the Horns Rev wind farm. The models range from linearized models to CFD (computational fluid dynamics) models. Note that the analysis is concerned with large offshore wind farms. Conditions in which wake losses are largest are considered, and it is concluded that lower-fidelity wind farm models tend to under-predict wake losses, while full CFD models tend to over-predict wake losses. All CFD models in the above-mentioned study solve the RANS (Reynolds-Averaged Navier-Stokes) equation (in contrast to for example Large Eddy Simulations). It is suggested that further research is needed in order to increase the understanding of wind farm wakes.

In an effort to get a more accurate understanding of wind farm wakes, many studies use LES (Large Eddy Simulation) to study wake losses. This is made possible by the improvement of computational resources. The main idea of LES is that large turbulent eddies are resolved, while only small eddies are modelled, in contrast to solving the RANS equations, where all turbulent eddies are modelled. One can thus postulate that LES is better suited towards studying wake losses, or wind farm aerodynamics in general. This idea is studied by Mehta et al., 2014, in which the contributions of various LES studies to wind farm aerodynamics are summarized and the use of LES is evaluated. The paper confirms that with the proper LES model and a refined grid, a substantially better accuracy can be achieved. Moreover, it is concluded that LES data can be used to improve engineering models (such as some of those discussed in Barthelmie et al., 2009), retaining computational efficiency while improving accuracy.

While the two paragraphs above describe the advancements made in studying wind farm wakes using numerical models, there is also an active field of research concerned with analytical wake loss models. Archer et al., 2018 provides a review and evaluation of six of these analytical wake loss models. The performance of the six models is evaluated using data from three wind farms, both on- and offshore. It is concluded that the

six models perform well, albeit with a generally positive bias in the estimation of the power production. This illustrates that analytical wake loss models can be useful for (preliminary) analysis of wake losses.

The work by Lanzilao and Meyers, 2022a illustrates that wake losses are, at the time of writing, still an active field of research. The paper proposes a new wake-merging method, in contrast to a classic linear superposition of the results of the analytical wake models. A higher accuracy is reported using the proposed improved method.

Concluding the present section, it can be noted that plenty of research has been done on the wake losses in (large) wind farms, and the merging of turbine wakes. Note that both effects express themselves downstream. This is a key thought, which will contribute to explaining the necessity of research in atmospheric gravity waves later in this chapter, since effects induced by atmospheric gravity waves can express themselves upstream.

3.2. Atmospheric Boundary Layer-Wind Farm Interaction

Besides the interaction between individual turbines within the wind farm, the farm will also interact with its surroundings. The present section will discuss the literature concerned with these interactions, specifically the interaction with the atmospheric boundary layer. The properties of the boundary layer vary depending on the location and the time of day. It is topped with a layer of warm air, which creates a temperature or capping inversion (Stull, 1988). The stability of the boundary layer is directly related to the surface cooling rate. To study the interaction between the atmospheric boundary layer and the wind farm one could vary the capping inversion strength, the capping inversion height, or the surface heating or cooling rate.

Examples of studies that vary the surface cooling rate are the work of Strickland et al., 2022 and the work of Sanchez Gomez et al., 2023. Both vary the surface cooling rate to study the effect on wind farm blockage. However, there are two key differences between the two studies. While Strickland et al., 2022 does not include a capping inversion to isolate the effect, and uses a laterally infinite wind farm, Sanchez Gomez et al., 2023 opts for realism, including a capping inversion and using a finite-size wind farm. The former reports an increased blockage effect with increasing atmospheric stability (i.e. an increased cooling rate) and reduced turbine spacing. This results in a decreased wind farm performance due to reduced entrainment of flow above the farm, and increased turbine interactions. Sanchez Gomez et al., 2023 reports an equal behaviour of the wind farm performance, reducing power generation with increasing atmospheric stability. Interesting to note is that the velocity deficit upstream of a stand-alone turbine does change with atmospheric stability, as is the case for an entire wind farm. Sanchez Gomez et al., 2023 indicates that the blockage effect for an entire wind farm is larger due to upward advection of streamwise momentum.

In the previous paragraph, two studies concerning the effect of atmospheric stability are presented. However, these studies are only considered with positive surface cooling, resulting in stably stratified flow. To see the effect of an unstable (or convective) boundary layer, the work of Abkar and Porté-Agel, 2015 provides an evaluation of the differences in the turbine wakes for interaction with stable and unstable boundary layers. Significant differences are found since wake growth is 2.4 times larger in unstable boundary layers, as well as stronger wake meandering. Moreover, an enhanced turbulence level within the unstable boundary layer causes an improved wake recovery.

As mentioned before, the interaction with the atmospheric boundary layer can be studied by varying the capping inversion strength or height, exactly the scope of work of Allaerts and Meyers, 2015 and Allaerts and Meyers, 2016. The former studies wind farms in a conventionally neutral boundary layer (CNBL), which is capped by a strong inversion layer. The authors postulate that this inversion layer can reduce the power production of the farm, as a result of the limited vertical entrainment of kinetic energy. It is concluded that a stronger capping inversion that is closer to the turbines will drastically decrease the power output of the farm, by up to 31% for a capping inversion that is lowered from $1500\,\mathrm{m}$ to $500\,\mathrm{m}$. Furthermore, the study found that a capping inversion limits the internal boundary layer growth of the wind farm. It is this boundary layer growth that is the cause of the decreased power output, not the limited vertical entrainment of kinetic energy as postulated earlier. The authors advise further study of the interactions with a CNBL, given the large impact on power production. Indeed, it can be seen in the literature presented in the remainder of this chapter that the CNBL is a frequent subject of study. Allaerts and Meyers, 2016 reports a similar behaviour in the power deficit of the wind farm as a result of a lower inversion height. Here, the capping inversion is lowered from $1000\,\mathrm{m}$ to $250\,\mathrm{m}$, the latter being a typical height for the capping inversion offshore. Consequently, a power decrease of 17% is observed. Furthermore, the authors show that the velocity deficit caused by the farm will displace the top of the boundary layer due to the conservation of mass.

Finally, for a thorough understanding of the interactions between the wind farm and the atmospheric boundary layer, Porté-Agel et al., 2020 may be consulted. The review summarizes (recent) research efforts in said interactions. Here, experimental (wind tunnel and field experiments), computational (CFD), and theoretical (analytical modelling) work is presented. The overview addresses cases in which a single turbine or an entire farm on homogeneous terrain is considered, as well as the effect of topography or a different kind of turbine (vertical-axis wind turbines). The authors indicate that the thermal stability of the free atmosphere can trigger standing gravity waves.

In short, it can be concluded that the interaction between the atmospheric boundary layer and a wind farm is worth studying since there can be a significant effect on the performance of the wind farm. Authors from research in this section note that there is a displacement of the top of the boundary layer and a possibility of standing gravity waves as a result of the thermal stability in the free atmosphere. It is indeed the field of atmospheric gravity waves that is the subject of the remainder of this chapter.

3.3. Atmospheric Gravity Wave Excitation

As an introduction to atmospheric gravity waves, this section serves to present the theoretical work behind their existence and excitation. These waves, sometimes called lee waves or mountain waves if excited by topography, are extensively studied. One of the earlier efforts in this field is the work by Gossard and Hooke, 1975. The textbook serves as an introduction to any kind of wave in the atmosphere that is of a less than global scale, dominated by atmospheric compressibility and gravitational stratification. This includes waves in the lower and upper atmosphere, as well as mountain lee waves. On the contrary, the book by Baines, 1998 specializes in density-stratified flow over and around topography, both from a theoretical and experimental perspective. The author discusses the two- and three-dimensional flow over topography, as well as two-layer flow, a concept that will be useful in modelling atmospheric gravity waves. The most recent textbook is that of Nappo, 2013, which provides the fundamentals of atmospheric gravity waves in all forms, as well as a gravity wave linear theory.

The explanation of an atmospheric gravity wave can be found in any of the three textbooks presented above. Such a wave occurs when buoyancy tries to get an air parcel that is perturbed back to equilibrium. Three conditions for existence can be deducted from this statement, gravity, stratification (for buoyancy to exist), and a perturbation (for example a mountain). Note that, according to Nappo, 2013, gravity waves do not exist without the presence of gravity, albeit the buoyancy force that is acting. Moreover, stratification can be a discrete interface between two types of fluid (for example the surface of the ocean), or a continuous stratification (such as the density distribution in the atmosphere). In the case of a CNBL, which includes a capping inversion, gravity waves can either exist above or in the inversion layer (or under if there is stratification present). The latter are interfacial gravity waves, and are studied by the work of Sachsperger et al., 2015, where the authors show that the waves have a strong dependency on the level of free atmosphere stratification. Specifically, the wave characteristics are evaluated.

As it is now clear that atmospheric gravity waves are present in many regions of the atmosphere, it is useful to study the implications for wind farms. Since the gravity waves impact the state of the atmosphere, the next section addresses the influence of these changed variables, like pressure and velocity, on a wind farm downstream of a perturbation, and vice versa.

3.4. Influence of Atmospheric Gravity Waves on Wind Farms

Since atmospheric gravity waves alter the flow field, it is instructive to study their effect on wind farms. The influence of topographically excited atmospheric gravity waves or trapped lee waves is studied by S. J. Ollier et al., 2018, S. Ollier, 2022, and S. J. Ollier and Watson, 2023, where a trapped lee wave is a type of atmospheric gravity wave that is trapped in a temperature inversion. In all three studies, the impact of waves excited by topography near the coast on an offshore wind farm is studied. Firstly, S. J. Ollier et al., 2018 reports that the trapped lee waves can cause a significant increase in the power output variation and that this variation is dependent on many factors, such as the properties of the wind farm, the atmospheric boundary layer (inversion strength and height, wind speed and direction), and the topography (dimensions and orientation). The variability in power output is a 76% difference between the most and least power-producing turbine, compared to 29% for a control case without topography. Interestingly, a higher total power production is reported for the case where trapped lee waves impact the farm, although it must be noted that for the control case, the surface roughness length is constant, and does not switch to the significantly lower roughness length over

the sea. S. Ollier, 2022 and S. J. Ollier and Watson, 2023 investigate the influence of trapped lee waves on wind farm power production as a result of different stability profiles (with either a neutral or stable surface layer) compared to a fully neutral stability profile. Compared to the fully neutral profile, a reduction in power production is reported for all cases. Moreover, it is found that peaks in the waves counteract wake losses in the wind farm, while troughs enhance wake losses. In large wind farms, the effect on the wake losses is found to be balanced out.

In Draxl et al., 2021, mountain waves (i.e. topographically excited atmospheric gravity waves) over the mainland of the United States are simulated and compared to various sources of experimental data. In contrast to the previous studies, that have been executed using CFD, the current study relies on a fast Fourier transform in WRF (Weather Research and Forecasting) simulations. Again, a significant variability in the flow field in a wind farm is reported. The authors advise taking into account mountain waves in the design of a wind farm, and in forecasting the power output, because of this variability in the quantity and quality of the wind resource.

It can be concluded that atmospheric gravity waves can have a significant effect on the power production of a wind farm. Therefore, it is valuable to conduct further research in this area, since an atmospheric gravity wave can be excited by various phenomena, not only topography. While it is desired to be able to properly forecast the output of a wind farm, further research is also beneficial for the optimization of wind farms, seeing that S. Ollier, 2022 reports an overall power output reduction.

3.5. Atmospheric Gravity Wave Self-Induction and Feedback on Wind Farms

In the field of atmospheric gravity waves, it was realized that the gravity waves could be excited by various causes, such as topography, the transition from land to sea, or weather phenomena (see e.g. Nappo, 2013). Recently, it was realized that wind farms themselves can induce atmospheric gravity waves. The work of Wu and Porté-Agel, 2017 and Allaerts and Meyers, 2017 show that a wind farm can provide the necessary vertical deflection of the flow at the wind farm entrance and, in combination with strong atmospheric stratification, excite atmospheric gravity waves. Since atmospheric gravity waves are known to impact the wind farm performance, many studies have been performed to investigate the feedback of self-induced gravity waves to the wind farm.

Wu and Porté-Agel, 2017 identifies five flow regimes in and around the wind farm that are of use in the literature discussion below. The regions are displayed in Figure 3.1. First, there is the induction zone upstream of the first row of turbines. In this zone, the flow is decelerated due to the blockage effect of the wind farm. In the presence of strong stratification (i.e. gravity wave excitation), the blockage effect is amplified, and the flow speed is further reduced. Additionally, the induction region grows in size, extending further upstream. Next, there is the entrance and development region, where the flow speed is again reduced due to momentum extraction by the turbines. The internal boundary layer generated by the farm grows in this region. Then, a fully developed region can be present. In this region, there are no or negligible streamwise variations in the flow, and the internal and atmospheric boundary layer heights are constant. Note that this region is not necessarily present, since the size of the farm will determine whether the flow will reach its fully developed state before exiting. Indeed the following region is the exit region. In this area just upstream of the last row of turbines, the flow is accelerated again. In the presence of strong stratification, there will be gravity wave excitation, which will contribute to the flow acceleration. Finally, behind the wind farm is the wake region, which is characterized by flow speed recovery.

Furthermore, Wu and Porté-Agel, 2017 introduces the inversion Froude number in the context of atmospheric gravity waves, defined as the ratio between the flow speed and the interfacial gravity wave (phase) speed. Consequently, an inversion Froude number smaller than one indicates that the gravity wave can propagate upstream as well as downstream (the subcritical case), while an inversion Froude number larger than one means the wave can only propagate downstream (the supercritical case). The inversion Froude number is an important parameter since it determines whether the interfacial atmospheric gravity waves can affect the flow field upstream. Next to identifying these key concepts in the field of atmospheric gravity waves, the study is concerned with the performance of a wind farm in an aligned or staggered layout, for weak ($Fr_i > 1$) and strong ($Fr_i < 1$) stratification. Under weak stratification, the power loss at the first row of turbines is 1.3% and 3% for the aligned and staggered layout respectively. However, under strong stratification, the effect is increased significantly, with power losses of 36% and 41% for the two layouts. Stratification has thus a significant impact on the induction zone and the turbines in the entrance region, and a farm in a staggered

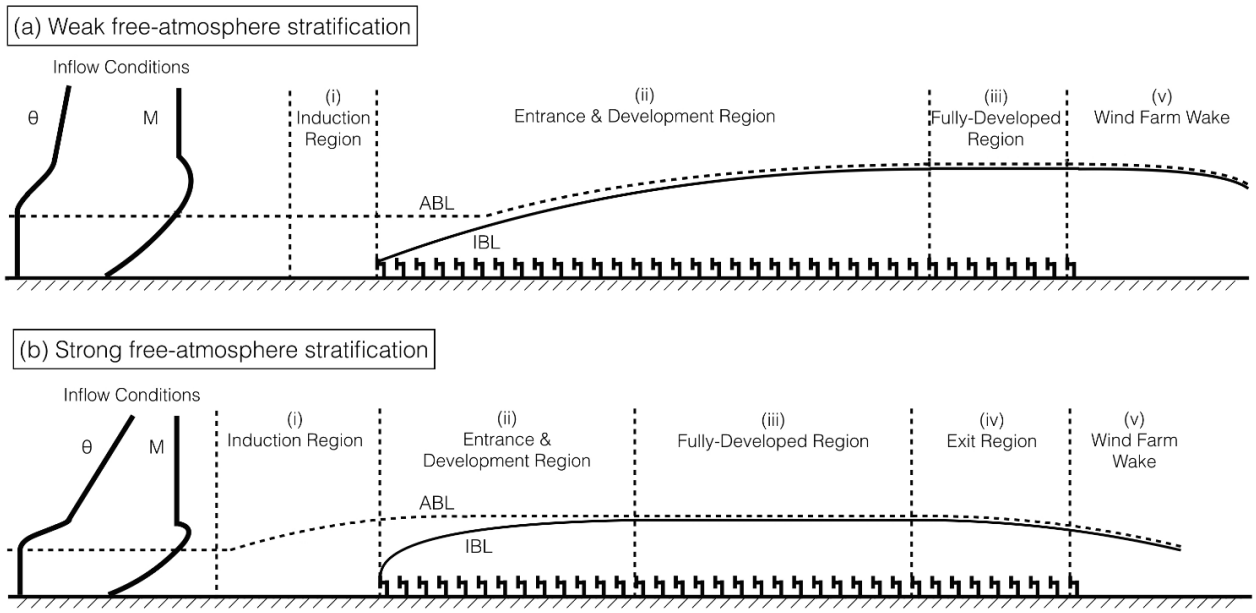

Figure 3.1: Flow regimes for a wind farm in a conventionally neutral boundary layer under weak and strong stratification. Reproduced from Wu, K. L., & Porté-Agel, F. (2017). Flow Adjustment Inside and Around Large Finite-Size Wind Farms. *Energies*, *10*(12), 2164. https://doi.org/10.3390/en10122164 This figure is licensed under a Creative Commons Attribution 4.0 International License.

layout seems to suffer more from this effect. On the contrary, the stronger stratification has a beneficial effect in the wake region, allowing the flow to fully recover after $5\,\mathrm{km}$, while the flow in weak stratification is not fully recovered even after $10\,\mathrm{km}$.

The study of Wu and Porté-Agel, 2017 uses a conventionally neutral boundary layer (CNBL) while varying the stratification of the free atmosphere above. Other studies have been performed on varying other characteristics of the CNBL, such as the capping inversion strength or height, or on comparing the results of a CNBL with a fully neutral boundary layer (NBL) or stable boundary layer (SBL). These studies are presented below. Note that all studies make use of Large Eddy Simulations. The extensive work of Allaerts, 2016 and Allaerts and Meyers, 2017 study wind farm performance as a result of the capping inversion characteristics. In Allaerts, 2016 the transition from a CNBL to an SBL is studied, as well as a fully developed CNBL flow. The stable boundary layer, or nocturnal boundary layer, is characterized by surface cooling, causing a stable layer near the surface. It was found that atmospheric gravity waves are excited in both cases. For the transition from CNBL to SBL, the boundary layer displacement and induced pressure gradients as a result of gravity wave excitation increase with the level of stability in the SBL. In general, the author describes the main effect of gravity waves as the lower wind speed in the induction zone, caused by the induced pressure distribution, and that the waves tend to redistribute the kinetic energy over the wind farm. The latter effect is maximal for lower boundary layer heights. As a general note, the study considered laterally infinite wind farms, and the author realizes that this may overestimate the excitation of atmospheric gravity waves.

Allaerts and Meyers, 2017 also finds gravity wave excitation in the inversion layer and the free atmosphere above, for a CNBL flow over the wind farm. Again it is concluded that a lower capping inversion height will strengthen the induced pressure gradients. Furthermore, the authors find that the internal boundary layer developed by the wind farm will interact with the inversion layer if its height is sufficiently small. Through an energy budget analysis, it is found that all kinetic energy comes from within the boundary layer, as entrainment through the inversion layer is insignificant. The study considered an infinite farm in the spanwise direction, and a fixed free atmosphere stratification (of $1\,\mathrm{K\,km^{-1}}$), equal to the work of Allaerts and Meyers, 2016. It is therefore of interest to study a varying free atmosphere stratification, indeed the subject of Lanzilao and Meyers, 2024. The specific study makes use of specific wind farm efficiencies, as defined by Allaerts and Meyers, 2018.

In Allaerts and Meyers, 2018 again a transition from CNBL to SBL is studied, for two different cooling rates. Atmospheric gravity waves were excited for all cases, and the amplitude of the waves increased with time and surface stability (i.e. a higher cooling rate). Moreover, the authors found that the average turbine power output is reduced by the gravity wave-induced pressure gradient, in comparison to the output of a turbine in

isolation. Next to these results, two efficiencies have been defined. Firstly, the wind farm wake efficiency is defined as the ratio between the total power output of the farm and the total power output if every turbine is a first-row turbine. Then, the non-local wind farm efficiency is defined as the ratio between the power output of a first-row turbine and the output of that same turbine in isolation. The latter is particularly useful in the analysis concerning atmospheric gravity waves.

The extensive study of Lanzilao and Meyers, 2024 makes use of these efficiencies. The study consists of 36 simulations, an additional 4 fully neutral simulations, and 4 simulations with stand-alone turbines. In these simulations, the capping inversion height, capping inversion strength, and free atmospheric lapse rate are varied, shown in Figure 3.2. The values that are picked for these variables are based on probability density functions for their occurrence, which are a result of 30 years of atmospheric data. Hence, Figure 3.2 is especially useful to get a feel for realistic atmospheric states. In contrast to the aforementioned studies, a finite wind farm is used. Shallow boundary layer flow (i.e. a low capping inversion height) increases the (counteracting) pressure gradient in the induction zone of the wind farm. Additionally, a strong capping inversion limits the vertical displacement of the flow, causing it to go to the sides of the farm. Gravity waves induced in the presence of stronger capping inversions have smaller wavelengths. A larger free atmospheric lapse rate also suppresses vertical motion, and this in turn causes the adverse pressure gradient at the entrance of the farm and favourable pressure at the exit of the farm to be of smaller magnitude. In regards to pressure gradients, the authors note that the pressure perturbations are an order of magnitude smaller for the fully neutral (NBL) cases, in comparison to the CNBL flows. The wind farm in the presence of an NBL has a non-local efficiency of 98%, while it is as low as 26% in the presence of a capping inversion and stratification aloft. The authors conclude that wind farm blockage is hence primarily related to atmospheric gravity waves. The total farm efficiency (the multiplication of wind farm wake and non-local wind farm efficiencies) is positively related to the free atmospheric lapse rate. Although the wind farm wake and non-local wind farm efficiencies are inversely related, the case with the lowest non-local efficiency (i.e. the strongest gravity wave feedback) still has the lowest total farm efficiency. Finally, it is interesting to note that the total farm efficiency is lower than the fully neutral reference case for lower capping inversion heights ($150\,\mathrm{m}$ and $300\,\mathrm{m}$ meters), while the opposite is true for higher heights ($500\,\mathrm{m}$ and $1000\,\mathrm{m}$).

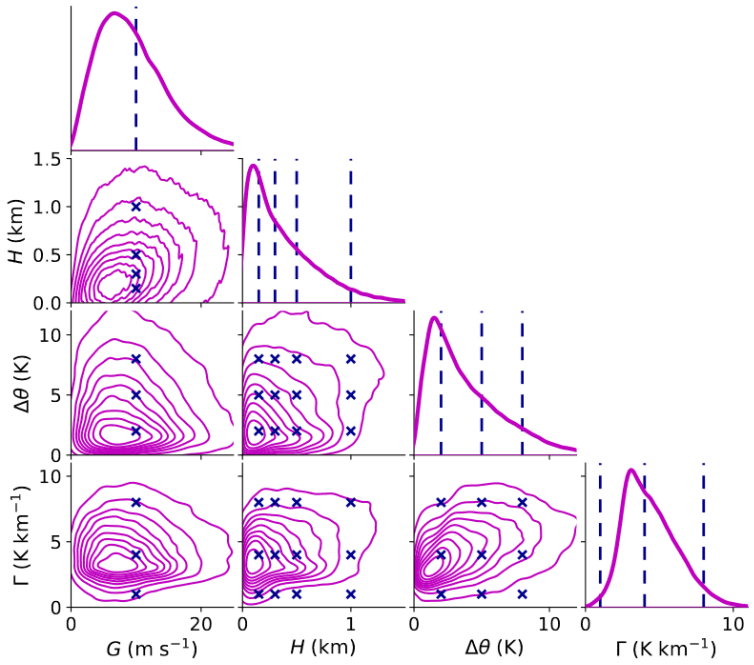

Figure 3.2: Probability of certain atmospheric states based on 30 years of atmospheric data. Note that the geostrophic velocity is represented by G. Reproduced from Lanzilao, L., & Meyers, J. (2024). A parametric large-eddy simulation study of wind-farm blockage and gravity waves in conventionally neutral boundary layers. *Journal of Fluid Mechanics*, *979*, A54. https://doi.org/10.1017/jfm.2023.1088 This figure is licensed under a Creative Commons Attribution-NonCommercial 4.0 International License.

The final study that uses LES in the present discussion is Lanzilao and Meyers, 2022b. In the study, a wind farm in a staggered and aligned configuration is considered, both in a CNBL and an NBL reference case. It was found that the total farm efficiency is 8.8% higher for a staggered farm when immersed in a CNBL flow, in comparison to the fully neutral counterpart. Note that the capping inversion height is around $600\,\mathrm{m}$, while its

strength is around $4\,\mathrm{K}$. The free atmospheric lapse rate is approximately $5\,\mathrm{K\,km^{-1}}$. One can thus conclude that the higher efficiency is in line with the results of Lanzilao and Meyers, 2024. Moreover, the non-local efficiency for a staggered farm is reported to be 4.6% lower than for the aligned configuration. The authors deduce that the farm in a staggered layout can extract a higher quantity of momentum from the flow, which promotes the boundary layer thickening and flow redirection around the farm. It must be noted that the authors stress that the results are highly dependent on the atmospheric state and can therefore not be generalized.

The above discussion highlights the body of research performed using LES in the field of atmospheric gravity waves. However, many studies are concerned with modelling the flow field around the wind farm. Many of these models rely on dividing the atmosphere into several layers. In the subsequent text, these studies will be highlighted, discussing the two-layer, three-layer, and multiscale coupled models.

The discussion begins with the work of Smith, 2010, in which the development of the two-layer model is discussed. In this linear model, the atmosphere is divided into the region containing the atmospheric boundary layer and the free atmosphere above. The model includes momentum exchange between the layers and with the surface, as well as gravity wave excitation. The results of the model show small wind perturbations, thus justifying the use of linear theory. The behaviour as a result of the Froude number is studied using the model. It is found that around an inversion Froude number of 1, the average wind speed reduction expresses singularity behaviour, which is more pronounced for certain atmospheric conditions.

Smith, 2022 uses the two-layer linear model, and adds Rayleigh damping, to conclude that gravity waves reduce the overall wind farm efficiency. The authors note that it is important to consider the interaction between farms since gravity waves can alter the flow field far upstream and far downstream of the farm.

The turbine drag that is taken into account in the lower layer of the two-layer model is only felt close to the surface within this layer, which is why Allaerts and Meyers, 2019 divides the lower layer into two. Furthermore, a Gaussian wake model is coupled to the model, resulting in an improved three-layer model. The model is validated using LES (two-dimensional) data and is found to obtain reasonable agreement. Moreover, the shape and magnitude of the flow perturbations are better captured than the original model of Smith, 2010. In agreement with the LES studies in the aforementioned text, the model found that gravity wave excitation is highest for low inversion height, free atmospheric stratification, and surface roughness. Moreover, the model also identifies the singularity behaviour for inversion Froude number close to 1. However, it was found that the feedback on wind farm efficiency is maximal for subcritical conditions close to the critical inversion Froude number of 1. Additionally, it is concluded that losses due to gravity waves are highest for large wind farms, with high turbines that have high thrust coefficients, in a farm that has an aspect ratio of about $3/2$. Both Allaerts and Meyers, 2019 and Smith, 2010 note that two non-dimensional parameters govern the effect of the induced pressure gradients. Next to the (inversion) Froude numbers, the studies identify the P_N number (which is analogous to the free-atmospheric Froude number used in the present study), which is based on the boundary layer flow velocity, the geostrophic flow speed, the Brunt-Väisälä frequency, and the boundary layer height. In the study, the wind speed and Brunt-Väisälä frequency are kept constant in the free atmosphere, and the extension of the model towards varying these parameters is exactly the subject of Devesse et al., 2022. The extended model that allows for changing speed and stability with altitude in the free atmosphere is validated using mountain wave reference cases. A wind farm cluster is analysed for one year of operation and thus for an array of atmospheric states. It was found that the wind speed reduction in the induction zone differs by more than 30% between uniform and non-uniform conditions for 17% of the atmospheric states. However, when averaging over all cases the impact is small. The authors thus conclude that taking into account non-uniformity is important when analysing a specific atmospheric state.

An example of the usage of a three-layer model is the work of Lanzilao and Meyers, 2021, which builds on the model of Allaerts and Meyers, 2019. In this study, the thrust coefficient distribution over the farm is optimized, for an array of atmospheric states. Although the thrust coefficient distribution is allowed to vary over space and time, a steady distribution yields the highest power gain. For the vast majority of atmospheric states, a power gain larger than 4% is observed. In cases where gravity wave feedback is largest (weak stratification and an inversion Froude number close to 1), the power gain is largest, reaching up to 14%.

The final model that will be discussed is the multiscale coupled (MSC) model presented in Stipa, Ajay, et al., 2024b. Multiscale refers to the fact that the model couples the microscale effects (turbine scale) and mesoscale effects (wind farm scale and larger). The three-layer model (mesoscale) of Allaerts and Meyers, 2019 is coupled with the Gaussian wake model (microscale). The current work presents an improved coupling of the microscale and mesoscale phenomena. The model is validated with LES data for subcritical and super-

critical flow regimes and can predict the farm's power output within a 2% deviation. The MSC model is used by the work of Stipa, Ahmed Khan, et al., 2024. In that study, the model is used to predict the displacement of the top of the boundary layer. Then, LES is performed with a domain that extends up to the boundary layer top, rather than several kilometers into the free atmosphere. With this technique, the authors can run simulations that use less than 15% of the computational resources of a classical domain while still being able to accurately predict wind farm performance.

3.6. Research Gap

Now that the body of literature has been laid out and discussed, the research gap in which the present research will fall can be identified. Atmospheric gravity waves are determined to have a significant impact on the wind farm performance. This impact with respect to the atmospheric state has been thoroughly studied. However, research has only touched the surface of the impact of gravity waves as a result of different wind farm layouts. General parameters such as the wind farm aspect ratio or size have been investigated shortly, as well as a staggered layout, but the influence of the entire parameter space of wind farm layout variables is yet to be determined. Moreover, all research so far has considered rectangular wind farms. Allaerts and Meyers, 2018 states that the response of a wind farm to atmospheric gravity waves is highly dependent on its layout, so a thorough investigation of different parameters (as discussed in the next chapter) is validated. Other studies that report the need for studying the wind farm layout include Allaerts and Meyers, 2018, S. J. Ollier et al., 2018, Lanzilao and Meyers, 2021, S. Ollier, 2022, S. J. Ollier and Watson, 2023, and Lanzilao and Meyers, 2024. Given the large parameter space, the multi-scale model presents itself as an excellent candidate for the study, especially given its accuracy.

3.7. Research Questions

The research questions that have been formulated to fill (part of) the research gap are presented below. The main question this study tries to answer is:

How does the wind farm layout affect atmospheric gravity wave excitation and its feedback on wind farm performance?

It can be noted that the research question is multifaceted, which is why the following subquestions have been formulated:

- *What is the proper length scale of non-uniform, very dense, or very sparse farms?*
- *What is the effect of the wind farm layout on the characteristics of the excited atmospheric gravity waves?*
- *How is wind farm performance affected by the flow field features induced by atmospheric gravity waves?*
- *What is the optimal wind farm layout to have the least atmospheric gravity wave-induced power losses?*

4

Methodology

The current chapter presents the methodology used towards the fulfilment of the research gap identified in the previous chapter. First, the overall approach is explained in Section 4.1. The chosen atmospheric state, wind turbines, and wind farm layouts are presented in Section 4.2, Section 4.3, and Section 4.4 respectively. Subsequently, Section 4.5 discusses the engineering model, while Section 4.6 elaborates upon the high-fidelity Large Eddy Simulation framework. Finally, note that the full simulation suite and an explanation of the simulation identifiers are presented in Appendix A. Since the literature review has shown that non-dimensional numbers are omnipresent, it is essential to discuss the definition and meaning of the different non-dimensional numbers in this study, which is done in Section 4.7.

4.1. General Approach

The present thesis aims to show the effect of different parameters that quantify a wind farm layout on atmospheric gravity wave excitation and the consequent feedback on wind farm performance. Since this thesis considers a large parameter space, as Section 4.4 will show, it is important to implement a one-factor-at-a-time (OFAT) methodology, such that a parameter can be isolated. The literature has shown that the length of a wind farm is an important parameter in determining the characteristics of atmospheric gravity wave excitation, for example, M. Khan et al., 2024 or Allaerts and Meyers, 2019. The length of a rectangular farm is therefore often the length scale used in the Froude number, which will be discussed in Section 4.7, representing the dominant length-scale of the wind farm. It is, however, unclear, what the characteristic length is of a non-uniform farm, say, a circular or triangular farm. Furthermore, very sparse or very dense farms may have different characteristic lengths, although their geometric length is equal. Similarly, the length scale used in the inversion Froude number must be tested for non-uniform and sparse farms. In other words, it is of interest to know when a wind farm is an entity, and when a collection of individual turbines. Consequently, the first step of this research is to investigate how to determine the characteristic length of non-uniform or sparse wind farms. Knowing the characteristic length of a wind farm and keeping it constant allows for a proper OFAT methodology since the desired parameter is then the only parameter varied.

The main research question can be split into two parts, the first part of which concerns understanding AGW excitation as a result of a certain wind farm layout. The interfacial wavelength is the main parameter to represent AGW excitation, that can be extracted from the MSC model. Additionally, the LES results will allow for the extraction of more wave characteristics, such as the direction of the wave in the $x-z$-plane. Note that due to the extensive parameter space, LES results will only be available for select cases. Since the selection depends on the results of the MSC model, it will be discussed in Chapter 5. The second part of the research question discusses the wind farm performance. Here, wind farm performance is mainly quantified using the non-local efficiency defined by Allaerts and Meyers, 2018, as it quantifies the power losses associated with the AGW-induced pressure gradients. Other quantities that might be of interest are the wake efficiency and total farm efficiency, and they will be investigated when they are of value to the discussion.

The methodology outlined in the previous paragraphs will give a clear image of what the effect is of the wind farm layout on AGW excitation and resulting feedback on wind farm performance. In practice, the goal is not to keep the characteristic length of a wind farm constant. Rather, there will be a budget that needs to be adhered to or a certain area that is allocated for a wind farm. Therefore, the MSC model is utilized to find exploratory guidelines for wind farm design from a developer's perspective, advising on how to mitigate

the negative effects accompanying AGW excitation. Thus, the idea of constant characteristic length is abandoned, and rather the constraint of (approximately) constant number of turbines is applied.

The research is concluded with the validation of the MSC model results using LES. Furthermore, a comparison between the LES framework and the MSC model will give insights into what the depth-averaged solution of the MSC model actually represents.

4.2. Atmospheric State

Since the focus of the present study is to investigate the sensitivity of atmospheric gravity wave excitation to wind farm layout, rather than the atmospheric state, this atmospheric state is kept constant, in contrast to many previous studies. The current section aims to display the selected atmospheric conditions and their representation using different numerical models. As discussed in Section 1.1, the conventionally neutral boundary layer (CNBL) is often studied, and representative of conditions offshore.

4.2.1. Conventionally Neutral Boundary Layer Representation

The potential temperature profile of the conventionally neutral boundary layer (CNBL) can be characterized using the capping inversion strength (CIS) $\Delta\theta$, the capping inversion height (CIH) H, and the capping inversion thickness (CIT) ΔH. The progression of the potential temperature in the free atmosphere is called the free-atmospheric lapse rate (FALR) Γ and is a measure of the free atmosphere's stability. Often-occurring values of these potential temperature characteristics can be determined using analysis of atmospheric data, see for example Lanzilao and Meyers, 2024. As a result, the CIS is $4\,\mathrm{K}$, the CIH is $500\,\mathrm{m}$, and the FALR is $4\,\mathrm{K\,km^{-1}}$. The CIT can be defined in multiple ways. Since it is an input to the Rampanelli and Zardi, 2004 model, which in turn is used to initialize the potential temperature distribution in the precursor simulation, it is set to $100\,\mathrm{m}$, based on its presence in Lanzilao and Meyers, 2024 and Stipa, Ajay, et al., 2024a which also use this model. Note that the CIH represents the centre of the capping inversion. The standard or reference potential temperature is set to $300\,\mathrm{K}$. The Brunt-Väisälä frequency can be determined using Equation 4.1 from Nappo, 2013 and is $0.0114\,\mathrm{s^{-1}}$.

$$N = \sqrt{\frac{g}{\theta_0}\Gamma} \tag{4.1}$$

To fully determine the flow in the boundary layer and the capping inversion, the veered velocity and shear stress magnitude profiles must be determined, which can be obtained using numerical simulation, analytical models, or observations, as discussed in Stipa, Ajay, et al., 2024b. The MSC model makes use of the Nieuwstadt, 1983 analytical model. To achieve realistic turbulent inflow conditions for LES successor simulations, one must perform precursor simulations. The details of this precursor simulation are further discussed in Subsection 4.6.2, but the results are shown in the top left and bottom left plots of Figure 4.1. Note that the precursor's domain height exceeds the ABL's height. The MSC model includes an option to use (averages of) the precursor data as inflow conditions. Although only one atmospheric state is considered, and therefore only one precursor simulation is needed, the Nieuwstadt model is used for the MSC simulations, since in real-life scenarios precursor simulations are likely unfeasible. A comparison between the two types of inflow for the MSC model is presented in Section 5.5.

The veered velocity distributions are simulated based on a reference velocity at a reference height. Here, the reference height is the hub height, at which the reference velocity will be $9.21\,\mathrm{m\,s^{-1}}$. From sources like Davis et al., 2023 or NREL, 2024 it can be deduced that the reference velocity is representable for many offshore locations. It must be noted that the precise reference velocity is not of interest, since the present study does not aim to simulate a specific wind farm or cluster. The reason for the decimals in the reference velocity comes from the fact that precursor data with a different reference height from a different study is reused. More details on this are shown in Subsection 4.6.2. Other inputs to the Nieuwstadt model are the CIH, the CIS, the friction velocity $u_\star$, the roughness length z_0, and the Coriolis parameter f_c, the latter three of which have not yet been determined. Firstly, the Coriolis parameter is a result of the reused precursor data and is $5.9204 \times 10^{-5}\,\mathrm{s^{-1}}$, corresponding to a latitude of $24°$. Next, the roughness length is set to $10^{-4}\,\mathrm{m}$, representing calm sea conditions according to Lanzilao and Meyers, 2024 and Taylor and Yelland, 2001. Finally, using the Monin-Obukhov similarity theory, the mean velocity profile can be shown to follow Equation 4.2, as demonstrated in Panofsky, 1963. Note that the expression is in its simplest form since the correction factor for stability is zero in a CNBL. The reference height and accompanying reference velocity have previously been determined, and hence this pair can be used to calculate the friction velocity. The Von Kármán κ constant is set to 0.4 by Stipa, Ajay, et al., 2024b.

$$U(z) = \frac{u_\star}{\kappa} \ln\left(\frac{z}{z_0}\right) \tag{4.2}$$

It must be noted that the geostrophic wind cannot freely be determined in combination with a reference velocity at hub height since this would be an overconstrained problem. The choice for setting the reference velocity at hub height ensures a fair comparison between the power production of turbines, but this comes at the cost of different geostrophic wind speeds for the analytical Nieuwstadt, 1983 model and precursor data. As will be discussed in Section 4.7, the geostrophic wind speed is an important parameter, and it is important to keep in mind that the values differ ($11.48\,\mathrm{m\,s^{-1}}$ and $9.31\,\mathrm{m\,s^{-1}}$ for the model and precursor data respectively). Finally, the density ρ is set at its standard value of $1.225\,\mathrm{kg\,m^{-3}}$. At the standard temperature of $300\,\mathrm{K}$ and the

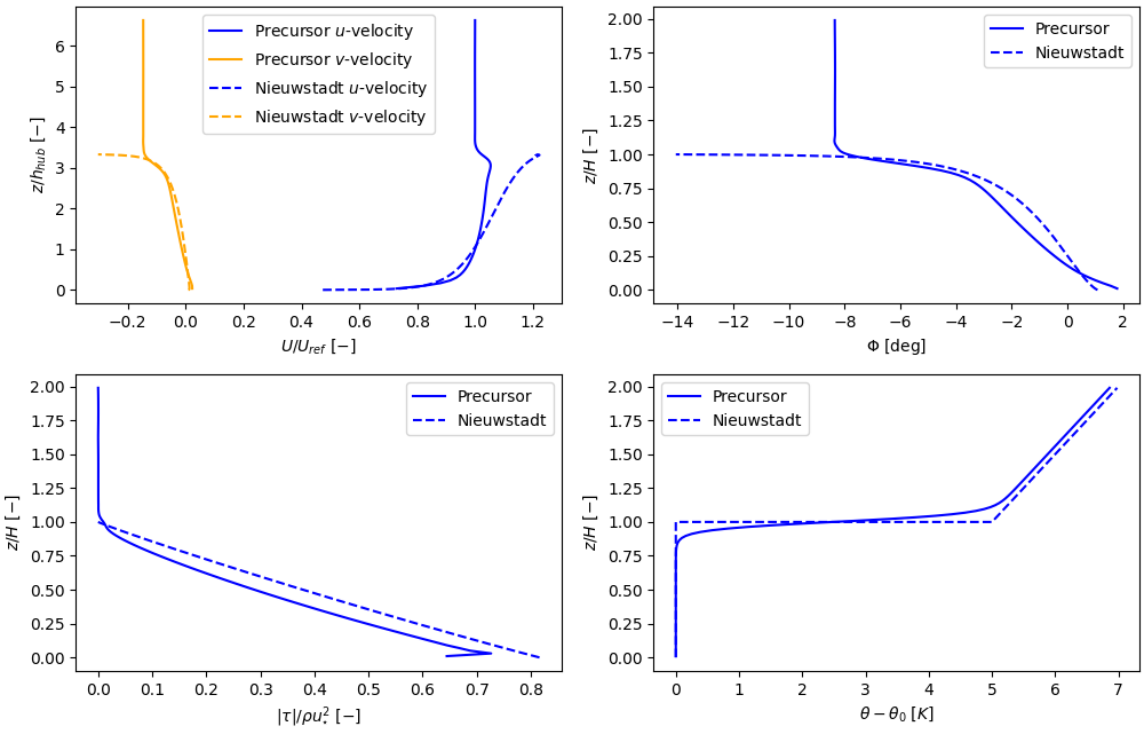

Figure 4.1: Characteristics of the conventionally neutral boundary layer, according to the Nieuwstadt, 1983 model and the precursor done by Stipa, Ahmed Khan, et al., 2024. The Nieuwstadt model yields data until the capping inversion height, while the precursor data reaches a height of $2\,\mathrm{km}$. Top left: veered velocity profiles showing the stream- and spanwise velocity as a fraction of the reference velocity at hub height. Top right: veering angle with height representing the direction of the velocity vector in the $x-y$-plane. Bottom left: shear stress magnitude with height non-dimensionalized with the dynamic pressure using the friction velocity. Bottom right: potential temperature deviation from its standard value with height. Note that the profile is an input rather than a result for the Nieuwstadt model.

aforementioned density the kinematic viscosity is $1.5 \times 10^{-5}\,\mathrm{m^2\,s^{-1}}$. The turbulence intensity level is a result of the precursor simulation and is $5\,\%$, and for reasons of consistency, this is also the turbulence intensity level used in the MSC model. Marek et al., 2016 shows that this is a representative value for many different offshore conditions.

4.3. Turbine Representation

The turbine selected for the wind farms is the IEA Wind 15-Megawatt Offshore Reference Wind Turbine, as presented in Gaertner et al., 2020. The reason for this choice is twofold. Firstly, the turbine is a reference turbine, with detailed geometric and performance data available to anyone, allowing for comparison between studies. Secondly, the high 15-MW power rating ensures that the turbine selection is relevant even in the future. Other key features of the turbine are presented in Figure 4.1. In the present study, the power and thrust coefficients are kept constant at their design values of 0.489 and 0.799 respectively. This will reduce the complexity of the problem to focus on the wind farm layout, in line with the OFAT methodology, and will allow for comparison with, for example, Allaerts and Meyers, 2019. The thrust and power coefficient curves are shown in Figure 4.2. The dashed lines show the aforementioned design values. Although a constant thrust and power coefficient is an idealization, it can be observed from Figure 4.2 that the design values are valid for a satisfactorily large interval around the reference velocity (of $9.21\,\mathrm{m\,s^{-1}}$), further justifying the choice for constant coefficients. For simplicity, the precone and uptilt angles of the turbines are set to zero. Moreover,

no rotational speed, pitch, or yaw controllers are implemented. The turbine is represented using the uniform actuator disk model without rotation in the LES.

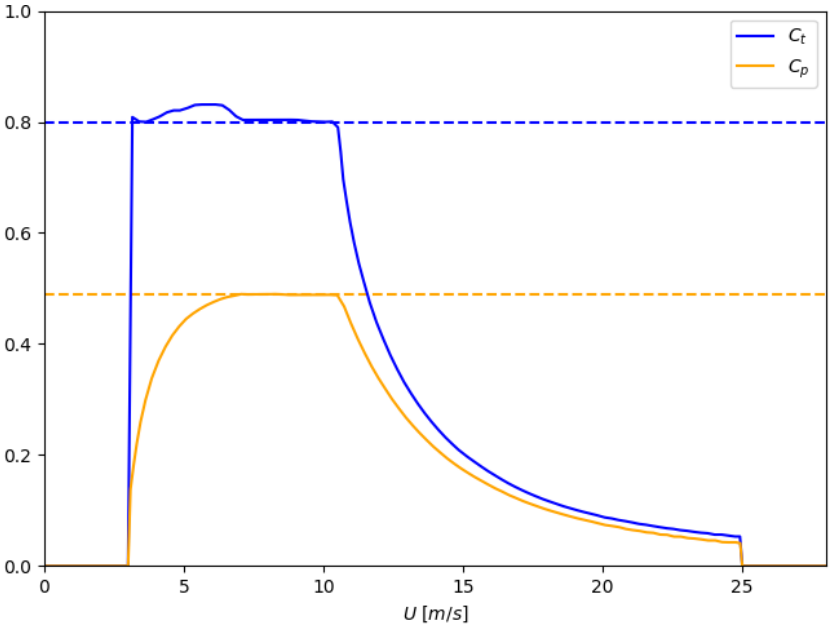

Figure 4.2: Thrust and power coefficient of the IEA 15-Megawatt reference turbine versus wind speed, with dashed lines showing the design thrust and power coefficients. Data taken from Gaertner et al., 2020.

Table 4.1: Key features of the IEA 15-Megawatt reference turbine. Data taken from Gaertner et al., 2020.

Parameter	Value
Rotor diameter D	$240\,\mathrm{m}$
Hub height h_{hub}	$150\,\mathrm{m}$
Hub diameter D_{hub}	$7.94\,\mathrm{m}$
Hub overhang d_{hub}	$11.35\,\mathrm{m}$
Design thrust coefficient C_T	0.799
Design power coefficient C_P	0.489
Cut-in wind speed U_{cut-in}	$3\,\mathrm{m\,s^{-1}}$
Cut-out wind speed $U_{cut-out}$	$25\,\mathrm{m\,s^{-1}}$

4.4. Wind Farm Parametrization

The research question of this thesis states that atmospheric gravity wave excitation as a result of wind farm layout is studied. However, wind farm layout can be quantified in many ways, and therefore the present section aims to lay out the different parameters that are varied, and what their levels are. The large parameter space is intended to give a complete image of any possible wind farm layout, and consequently, this study is parametric in nature. The varied parameters are divided in three categories, being farm layout, turbine characteristics, and farm shape and orientation, all of which are elaborated upon below. All simulations that have been performed are displayed in Appendix A. Each simulation has a unique identifier to quickly distinguish the wind farm layout. As discussed in Section 4.1 the research question is studied from a theoretical perspective, where the characteristic length is kept constant, and from a more practical developer's perspective, where the number of turbines is kept constant. Constant characteristic length is denoted by 'L', and constant number of turbines by 'T'. The identifier is further completed by an abbreviation of the studied parameter, a number, and the numerical method. As an example, 'PDL4MSC' is the fourth simulation that studies the power density at constant characteristic length using the MSC model. Finally, the standard layout of a wind farm is five rows, five columns, and a $5D$ spacing, unless otherwise mentioned.

4.4.1. Farm Layout

Farm layout refers to how the turbines are positioned over a certain wind farm. The first thing that comes to mind is putting the turbines further from or closer to each other. Therefore, the streamwise spacing and spanwise spacing are varied individually, and the power density is varied by increasing both spacings equally.

To obtain a practical range of turbine spacings, the work of Borrmann et al., 2018 is followed, where streamwise spacings from 5 to $12D$ are reported, and spanwise spacings from 3 to $8D$ are reported for various European offshore wind farms. Therefore, the simulations for a constant number of turbines vary the spacings in this way. The power density is varied from 3 to $45\,\mathrm{MW\,km^{-2}}$ by varying the turbine spacing from 3 to $12D$. The turbine spacing is $5D$ in the direction that is kept constant. Note that the power density is calculated using Equation 4.3, where the rated power times the number of turbines is divided by the farm area, which is defined as the convex hull of the set of coordinates of the turbine towers. The area can be expressed in terms of the turbine spacings in the case of a rectangular farm.

$$\Pi = \frac{N_t P_{rated}}{A} = \frac{N_t P_{rated}}{(N_{t_x} - 1) s_x D (N_{t_y} - 1) s_y D} \tag{4.3}$$

For the farms with constant characteristic length, the farm length is set to $48D$. Furthermore, the range of spacings is extended to 2 to $16D$, for maximum data spread. The power density thus ranges from 2 to $73\,\mathrm{MW\,km^{-2}}$. Note that the turbine spacing in the direction with constant spacing is set to $4D$, to ensure an integer number of columns or rows. The abbreviations for simulations studying the streamwise turbine spacing, spanwise turbine spacing, and power density are 'TSX', 'TSY', and 'PD' respectively.

A horizontally staggered wind farm, in contrast to a uniformly aligned wind farm, has rows of turbines that are misaligned to some extent. Here, the staggering angle as defined by Stevens et al., 2013 in Equation 4.4 is a useful parameter to quantify the amount of staggering, where the ratio between the offset in the spanwise direction and the spacing in the streamwise direction defines the angle. Using the spacing in the spanwise direction, as seen in Equation 4.5, the maximum angle can be obtained. The parameter that will be varied is the non-dimensional staggering angle, as defined in Equation 4.6, taking the values 0, 0.25, 0.5, 0.75, and 1.

$$\psi = \arctan \frac{s_{y,\mathrm{offset}}}{s_x} \qquad (4.4) \qquad \psi_{\max} = \arctan \frac{s_y/2}{s_x} \qquad (4.5) \qquad \tilde{\psi} = \frac{\psi}{\psi_{max}} \qquad (4.6)$$

Note that no different layout is needed for the different types of analysis since the farms have a constant number of turbines and a constant characteristic length. The abbreviation used for horizontal staggering is 'HS'.

Finally, it is studied how the concentration of turbines along the boundaries of the wind farm influences the atmospheric gravity wave excitation. To do so, the reference layouts by Kainz et al., 2024 will be utilized, which are based on Borssele zones III and IV of the Belgian-Dutch wind farm cluster. The wind direction will be perpendicular to the largest side of the wind farm, as indicated by the wind rose in Kainz et al., 2024. Although the farm is designed for the 10-megawatt reference turbine, the 15-megawatt reference turbine will be used to be consistent with the rest of the study. The wind farm consists of 37 turbines. The regular and irregular reference farms are presented in Figure 4.3. In the regular farm, the mean spacing is $7.1D$. The irregular farm is better quantified by its minimum turbine spacing, which is $2.2D$. Both farms cover a surface of $182\,\mathrm{km^2}$. Note that the area of the farm is pre-defined, and therefore not calculated using the convex hull. The abbreviation for the consequent simulations is 'FLNU'.

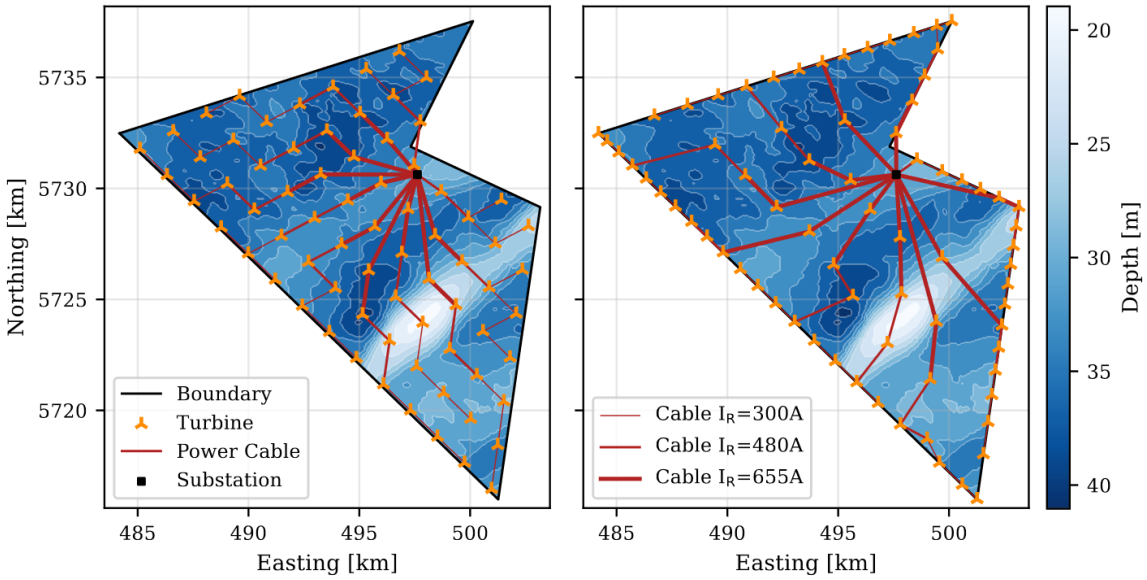

Figure 4.3: Reference layouts to study farm non-uniformity with on the right a uniformly spaced farm, and on the left an optimized farm in the same area. Reproduced from Kainz, S., Quick, J., Souza de Alencar, M., Sanchez Perez Moreno, S., Dykes, K., Bay, C., Zaaijer, M. B., & Bortolotti, P. (2024, March). *IEA Wind TCP Task 55: The IEA Wind 740-10-MW Reference Offshore Wind Plants* (tech. rep. No. NREL/TP-5000-87923). National Renewable Energy Laboratory (NREL), Golden, CO (United States). https://doi.org/10.2172/2333634 with permission.

4.4.2. Turbine Characteristics

In the present section, wind farm layouts that change the characteristics of individual turbines, such as hub height or rotor diameter, are discussed. Since the location of the turbines is not changed, all farms are five by five, with a $5D$ spacing.

As a lower limit to the hub height, practical tip clearances for offshore wind turbines are followed. Gaertner et al., 2020 reports the value varies between 20 to $30\,\mathrm{m}$, and Netherlands Wind Energy Association, 2023 vows for standardizing a value of $25\,\mathrm{m}$, so this study will use that clearance. The upper limit on the hub height is enforced by the limits on the MSC model. A large hub height close to the capping inversion height will yield perturbations that are too large for the linear model to be valid. For now, a maximum of $205\,\mathrm{m}$ is selected, but in Chapter 5 this choice is validated. Either way, larger hub heights are assumed to be unfeasible anyway. The hub height is increased in $15\,\mathrm{m}$ increments. The hub height can also be increased by vertical staggering, where only the odd or even rows are elevated. Since Zhang and Stevens, 2018 reports differences between these two cases, both are investigated, and the rows with constant hub height have a standard hub height of $150\,\mathrm{m}$. The abbreviations for investigating the hub height of all rows, the hub height of even rows, and the hub height of odd rows are 'HH', 'VS', and 'VSR' respectively. Note that the reference height was set to the hub height. Although the hub height changes, the reference height is kept constant to preserve the velocity inflow profile, rather than the velocity at hub height.

An increase in the turbine rotor diameter will also be limited by the $25\,\mathrm{m}$ clearance to the sea. Therefore, the maximum rotor diameter is $250\,\mathrm{m}$. As a sensible minimum rotor diameter for a turbine of this size and rated power, $220\,\mathrm{m}$ is chosen. All values in between using $10\,\mathrm{m}$ increments are also simulated. Note that the turbine spacing of $5D$ is always determined using the original rotor diameter of $240\,\mathrm{m}$, such that the absolute distance is constant. The abbreviation for runs studying the rotor diameter is 'RD'.

4.4.3. Farm Shape and Orientation

The final category of farm layout consists of farms differing in shape, and their orientation with respect to the incoming freestream. Here, equal turbines that are equally spaced are positioned in different ways, as explained below.

The aspect ratio is the ratio of the width to the length of the wind farm. For a farm of constant (characteristic) length, the number of columns is varied from 2 to 17, while keeping the number of rows constant at 5. The spacing is constant at $5D$. This approach yields aspect ratios ranging from 0.25 to 4. The farm with a constant number of turbines will have configurations of 2 by 11, 3 by 9, 4 by 7, 5 by 5, and their transposed versions, causing the aspect ratio to range from 0.1 to 10. The spacing is again its default value. The abbreviation for the simulations is 'AR'.

Finally, five basic shapes will be studied (square ('SFSNU'), rectangle ('RFSNU'), circle ('CFSNU'), triangle ('TFSNU'), and ellipse ('EFSNU')), for different orientations. Note that although square and rectangular farms have already been studied in the above sections, the focus is here on the farm shape with respect to the direction of the wind. Thus, rotating the farm will give a new effective farm shape. The square farm is a 6 by 6 wind farm with a spacing of $5D$. The rectangular farm will be 9 by 4 with a $5D$ spacing. The square farm is rotated to $0°$, $22.5°$, $45°$, $-22.5°$. Any rotation further than $45°$ will be a repetition. Although the positive and negative $22.5°$ rotations are each other's mirrored version, they will both be analyzed since the flow does not have symmetry along the y-axis due to the Coriolis effect. The same approach is applied to the rectangle, but due to the width and length not being equal, now rotations up to $90°$ are necessary. Furthermore, the alignment of the diagonal of the rectangle with the flow is studied. Next, an equilateral triangle of 36 turbines is considered, each row having one more turbine than the previous one. Here, $0°$, $90°$, $-90°$, and $180°$ (or, equivalently, $0°$, $30°$, $60°$, and $90°$) rotations are considered as unique layouts, where the triangle points either upstream, downstream, or to one of the two lateral sides. Lastly, the circular wind farm will be based on the optimal packing of 37 turbines with $5D$ spacing (so the optimal packing of 37 circles of $5D$ diameter, following Lubachevsky and Graham, 1997), with a diameter of approximately $6.9\,\mathrm{km}$. Equivalently, the elliptic wind farm will be based on the optimal packing of 39 turbines with $5D$ spacing within an ellipse of which the major axis ($10.5\,\mathrm{km}$) is about twice as large as the minor axis ($4.8\,\mathrm{km}$), following the work of Birgin et al., 2013. The elliptic wind farm will be studied in the $0°$, $45°$, and $90°$ orientations. The circular and elliptic layouts are presented in Figure 4.4 and Figure 4.5 respectively, where a turbine will be placed at the centre point of each circle.

4.5. Multi-Scale Coupled Model

The Multi-Scale Coupled (MSC) model is a reduced-order model made by Stipa, Ajay, et al., 2024b. In the present section, it is introduced in Subsection 4.5.1. Then, the determination of a suitable domain, grid refinement level, and desired tolerances are laid out in Subsection 4.5.2. Finally, the limits of the MSC model and

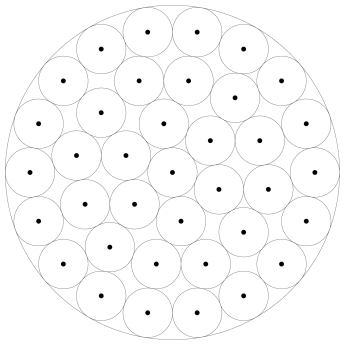

Figure 4.4: Circular wind farm layout. Adapted from Lubachevsky, B. D., & Graham, R. L. (1997). Curved Hexagonal Packings of Equal Disks in a Circle. *Discrete & Computational Geometry*, *18*(2), 179–194. https://doi.org/10.1007/PL00009314 with permission from SNCSC.

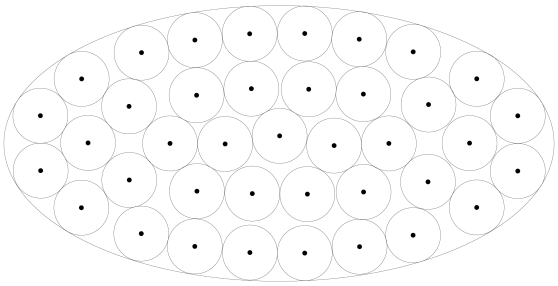

Figure 4.5: Elliptic wind farm layout. Adapted from Birgin, E. G., Bustamante, L. H., Callisaya, H. F., & Martínez, J. M. (2013). Packing circles within ellipses. *International Transactions in Operational Research*, *20*(3), 365–389. https://doi.org/10.1111/itor.12006 with permission from John Wiley and Sons.

flags that can be turned on or off are discussed in Subsection 4.5.3 The model is based on the three-layer model by Allaerts and Meyers, 2019.

4.5.1. Working Principles

Multi-scale refers to the combination of micro- and mesoscale effects. As previously mentioned, microscale effects relate to the turbine level, while mesoscale effects concern the atmospheric level. The meaning of these three layers can be deduced from Figure 4.6, which is taken from the work of Allaerts and Meyers, 2019. The wind farm layer contains the microscale effects caused by the thrust force of the turbines. Together with the upper layer, it forms the part of the atmosphere that is underneath the inversion layer, such that $H_1 + H_2 = H$. Above the inversion layer is the free atmosphere layer. The capping inversion displacement is $\eta_{(t)}$, which is obtained by the superposition of the displacements of the two lower layers.

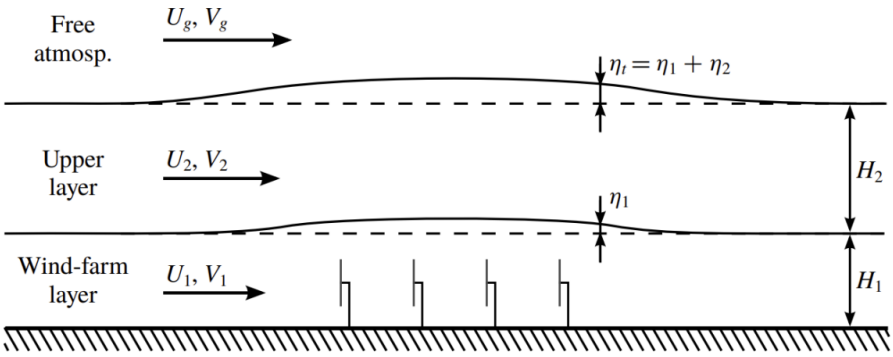

Figure 4.6: Representation of the three layers in the 3LM and MSC model. Reproduced from Allaerts, D., & Meyers, J. (2019). Sensitivity and feedback of wind-farm-induced gravity waves. *Journal of Fluid Mechanics*, *862*, 990–1028. https://doi.org/10.1017/jfm.2018.969 with permission from Cambridge University Press.

The solution procedure is conveniently shown in Figure 4.7, which is presented in Stipa, Ajay, et al., 2024b. Firstly, the background state is initialized using the parameters described in Section 4.2. Then, using a homogeneous velocity field, the turbine thrust is set up. In the three-layer model (3LM) step, the pressure perturbation as a result of the turbine thrust is calculated. Next, in the three-layer model reconstruction (3LMR) step, the turbine effects are removed from the perturbation field. Since it is desired to use the perturbation field again to update the thrust later on, it is essential to remove the turbine contributions now to avoid double-counting the effects. Note that since the background velocity field does not contain turbine effects, it is especially useful in determining the atmospheric gravity wave characteristics. The 3LMR-step is the new coupling mechanism developed in Stipa, Ajay, et al., 2024b, which is the principal difference from the original three-layer model. The perturbation fields without the turbine contributions are still depth-averaged, so the background velocity needs to be reconstructed such that a height dependency is obtained. From this, the velocity at hub height can be obtained which is needed to run the wake and induction models. Now, all ingredients are in place to update

the thrust coefficient and thus the thrust force, after which all steps can be iterated until convergence on the pressure is achieved. Finally, the converged fields can be postprocessed to obtain valuable parameters, such as the turbine power.

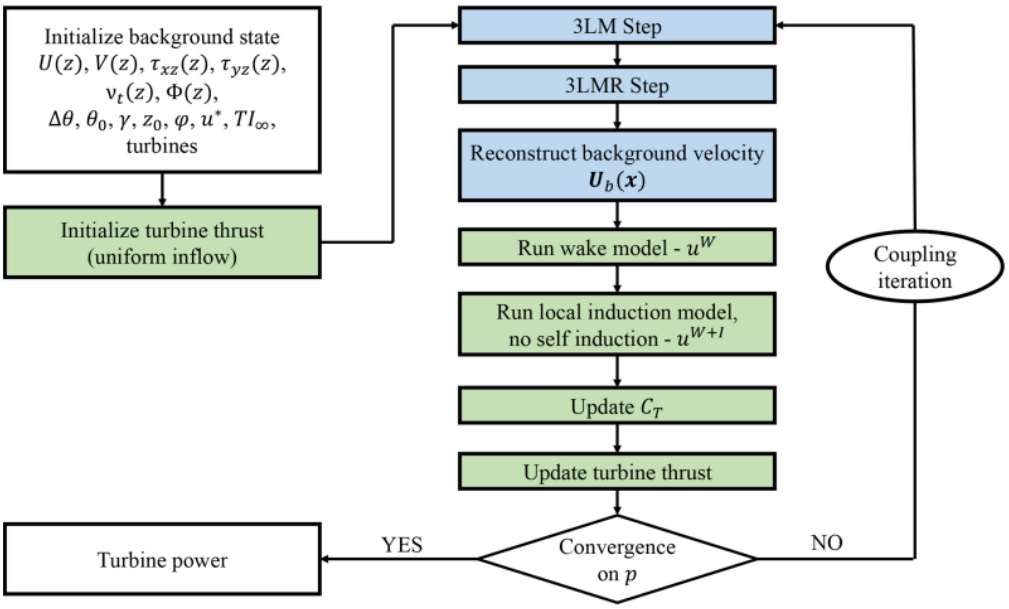

Figure 4.7: Solution procedure of the MSC model containing in green the steps concerning microscale effects, and in blue the steps concerning mesoscale effects. Reproduced from Stipa, S., Ajay, A., Allaerts, D., & Brinkerhoff, J. (2024b). The multi-scale coupled model: A new framework capturing wind farm–atmosphere interaction and global blockage effects. *Wind Energy Science*, *9*(5), 1123–1152. https://doi.org/10.5194/wes-9-1123-2024 This figure is licensed under a Creative Commons Attribution 4.0 International License.

4.5.2. Numerical Setup

In the MSC model, the domain size, domain discretization, and number of iterations need to be determined to complete the numerical setup. The domain size needs to be such that wave reflection and perturbation re-entry are prevented. In contrast to Large Eddy Simulation, the MSC model has no damping layers implemented. Therefore, wave reflection can occur at the boundaries. Furthermore, as Stipa, Ajay, et al., 2024b discusses, the solver of the MSC model makes use of Fourier transforms, and therefore the use of periodic boundary conditions is enforced. Therefore, undamped perturbations are recycled at the inlet and can influence the solution, just like wave reflection. To prevent the issue, the domain should be large enough, such that the perturbations have naturally damped out. Wave reflection and perturbation re-entry is visible in Figure 4.8, and by visual inspection of the reflection and re-entry the domain is selected to be $400\,\mathrm{km}$ and $200\,\mathrm{km}$ in the streamwise and spanwise directions respectively. The two remaining boundaries are the top and bottom of the domain. The effect of the ground on the flow is simulated by mirroring the wind farm, as discussed in Stipa, Ajay, et al., 2024b. Finally, Stipa, Ajay, et al., 2024b argues that the third layer, which represents the free atmosphere in the three-layer model, effectively acts as a boundary condition.

To find a suitable cell size, a grid convergence study has been performed. Figure 4.10 displays the L_2-norm of the error that is quantified as the difference between a coarse mesh and the fine mesh with a $100\,\mathrm{m}$ cell size. To calculate the difference cubic interpolation of the coarse mesh is applied. The solution consists of the background velocity obtained by the MSC model for a five-by-five wind farm. Only the part of the domain where either the wind farm or atmospheric gravity waves are located is used. It can be seen that the rate of reduction of the L_2-norm decreases when going from $3200\,\mathrm{m}$ to $400\,\mathrm{m}$ cell size, indicating that convergence is approached. However, the rate increases again when going to finer resolutions. It is believed that this is due to the fact that from a resolution of $200\,\mathrm{m}$ and lower, the individual effects of turbines are captured, as displayed in Figure 4.9, and that the rate of reduction would decrease again for finer resolutions. It is not possible to simulate finer resolutions due to memory restrictions. In conclusion, although a grid-independent solution is not achieved, it is assumed that a grid resolution of $100\,\mathrm{m}$ yields sufficient numerical accuracy, especially given the large length scales of the atmospheric gravity waves. Moreover, key parameters like the wavelength and turbine power seem to oscillate around the expected value, indicating that a further mesh refinement will not give more accuracy.

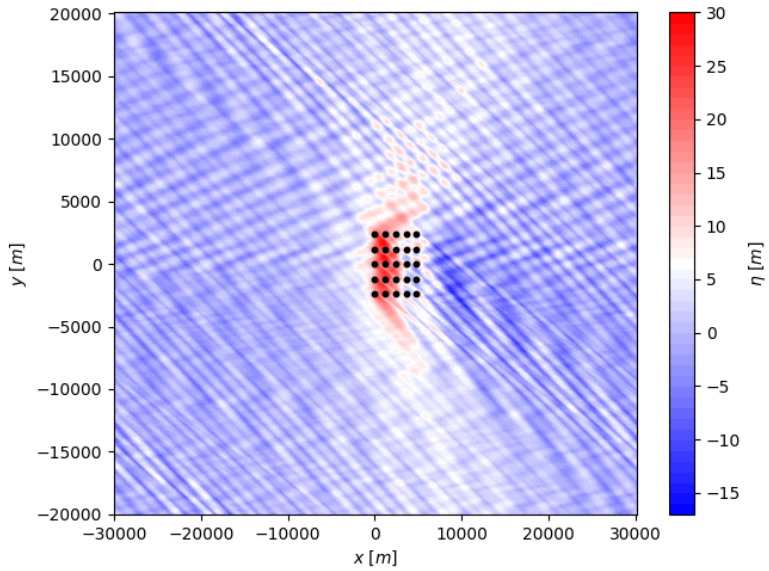

Figure 4.8: Wave reflections and perturbation re-entry visible in the boundary layer displacement field in a small 60 by $40\,\mathrm{km}$ domain for a five-by-five wind farm.

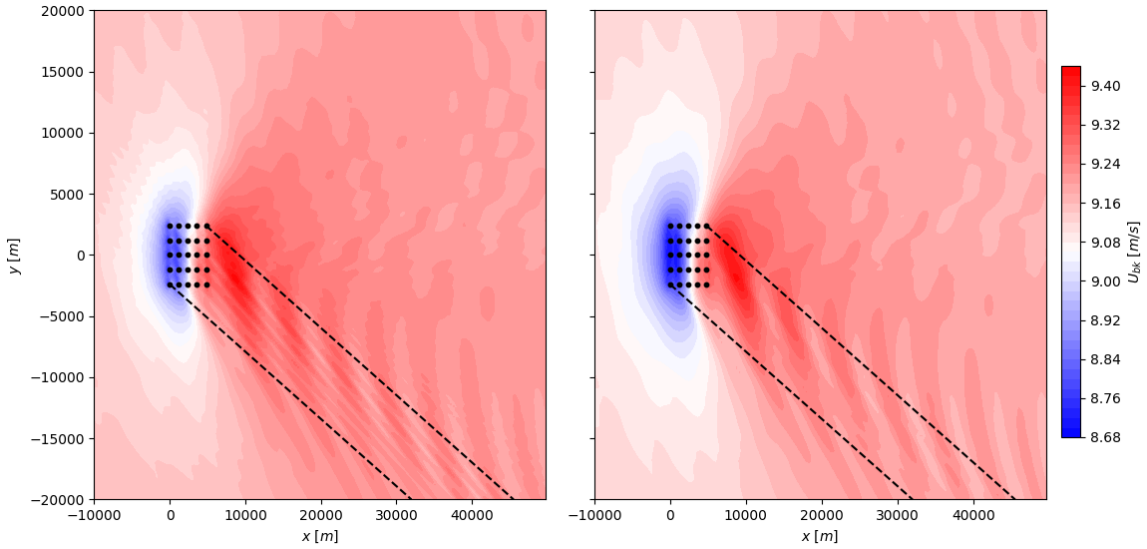

Figure 4.9: Background velocity field for a five-by-five wind farm with a cell size of $200\,\mathrm{m}$ (left), where the effects of the individual turbines are captured in the area between the dashed lines, and a cell size of $400\,\mathrm{m}$, where the effects of the individual turbines are not captured.

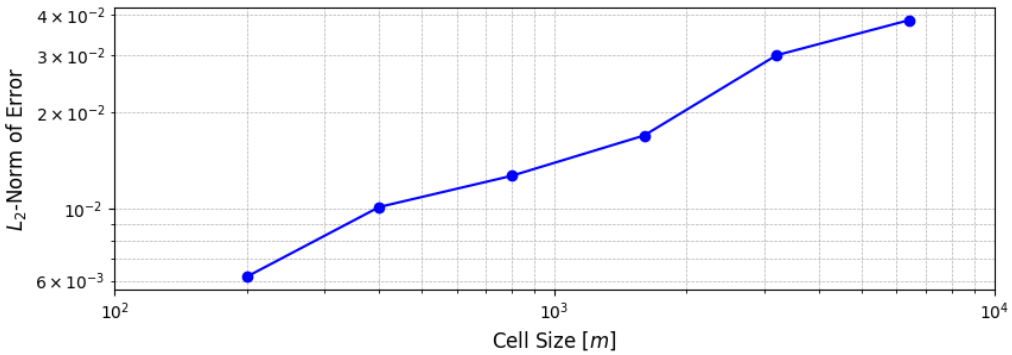

Figure 4.10: L_2-norm of the error that is quantified as the difference between a coarse mesh and the fine mesh with a $100\,\mathrm{m}$ cell size. To calculate the difference cubic interpolation of the coarse mesh is applied. The solution consists of the background velocity obtained by the MSC model for a five-by-five wind farm. Only the part of the domain where either the wind farm or atmospheric gravity waves are located is used.

As can be seen in Figure 4.7, the solution procedure ends when the pressure perturbation residual is converged, and hence it is useful to define the number of iterations after which the residual has decreased to a satisfactory level. Stipa, Ajay, et al., 2024b reports that five iterations are sufficient to get the pressure residual under $10 \times 10^{-4}\,\mathrm{Pa}$. Since the present study makes use of a different turbine, the pressure residual is plotted versus the number of iterations in Figure 4.11. It can be observed that the pressure residual is higher than previously reported. However, it is deemed that the residual at five iterations is satisfactory, since Stipa, Ajay, et al., 2024b has found that one iteration is enough for capturing the major interaction effects between the wind farm and atmospheric gravity waves, and that three iterations will be sufficient for thrust and power distribution. It is assumed that this can be extrapolated to the present study, especially given the fact that the thrust coefficient is constant.

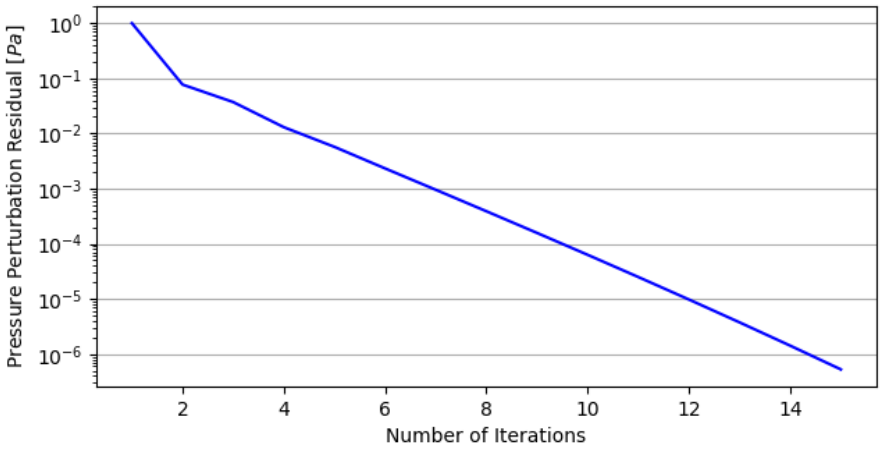

Figure 4.11: Pressure perturbation residual versus the number of iterations of the MSC model.

4.5.3. Limitations and Choices

While the MSC model does an excellent job of giving accurate results using low computational time, naturally this will come with some limitations. First and foremost, the effect of the internal and interfacial gravity waves cannot be readily distinguished. The velocity field in the free atmosphere would be necessary to investigate the internal gravity waves separately. Rather, it will be investigated which wave type is dominantly displayed in the MSC results. As mentioned before, the results of the MSC model are depth-averaged. This prevents from calculating any wave characteristics besides the wavelength, which would require the vertical velocity field. Moreover, it is advised to limit the hub height such that the perturbation levels stay within the assumptions of the linear model. In practice, the guideline would be Equation 4.7 (Stipa, Ahmed Khan, et al., 2024). In general, it is essential that the solution does not contain perturbations that are too large, as it will yield unfeasible results, like excessively large turbine powers. The efficiencies can be a good measure of feasible results, as they cannot be larger than one. Furthermore, the turbine power cannot exceed the theoretical maximum. It is observed that maximum perturbations of $15\,\%$ can be allowed to obtain physical results.

$$\frac{2h_{hub}}{H} \leq 0.75 \tag{4.7}$$

Besides certain limitations, there are also some choices to make regarding the different models that are included in the MSC model. Firstly, it can be opted to calculate the microscale velocity field. Although the microscale effects are always taken into account, the high-resolution microscale field is not calculated, since it is computationally expensive. The high-resolution field around the turbines is not needed since it is the mesoscale background velocity field caused by the atmospheric gravity waves that is of interest. Furthermore, there is a deep-array model implemented in the MSC model. According to Stipa, Ajay, et al., 2024b, the deep array model only improves the results for random wind turbine configurations and in the far wake, both of which are not relevant to the present study. Therefore, the deep-array model is not included.

4.6. Large Eddy Simulation Framework: TOSCA

The Large Eddy Simulation (LES) framework that will be used for high-fidelity results is the Toolbox fOr Stratified Convective Atmospheres (TOSCA) code by Stipa, Ajay, et al., 2024a. It is especially suited to study

the wind farm's interaction with the atmospheric gravity waves. Its working principles are discussed in Subsection 4.6.1. Next, the precursor simulation needed to generate realistic inflow conditions is discussed in Subsection 4.6.2. The numerical setup of the successor simulations is discussed in the subsequent sections, where Subsection 4.6.3 presents the domain, mesh, and boundary conditions, while Subsection 4.6.4 discusses the parameters that control the successor, such as the time-stepping, numerical schemes, or choice of controllers.

4.6.1. Working Principles

TOSCA is a finite-volume code using generalized curvilinear coordinates. TOSCA has been selected for the present study since it is specifically designed for the simulation that needs to be performed. Furthermore, TOSCA allows for enforcing the reference velocity at hub height. Finally, TOSCA's post-processing options allow for easy comparison with the MSC model. The governing equations are the conservation of mass and momentum of incompressible flow with Coriolis forces, subject to the Boussinesq approximation, with the transport equation for potential temperature closing the set, as shown in Stipa, Ajay, et al., 2024a. The LES model used for modelling the sub-grid stresses is the dynamic Smagorinsky model by Lilly, 1992 and Germano et al., 1991. The Lagrangian averaging of the Smagorinsky constant as discussed in Meneveau et al., 1996 is implemented. For further details on the workings of the TOSCA code the reader is referred to Stipa, Ajay, et al., 2024a.

4.6.2. Precursor Simulation

The precursor is a simulation without wind turbines used to generate realistic turbulent inflow for the successor simulation. As the precursor data from Stipa, Ahmed Khan, et al., 2024 matches the desired atmospheric state, the data can be reused, allowing for a reduction in computational costs. The flow in the precursor advances for $100\,000\,\mathrm{s}$ until it has reached steady-state turbulence statistics. The flow then further advances until $150\,000\,\mathrm{s}$ and is sampled at a desired time interval at a plane parallel to the inlet of the domain. These slices can be used to have a time-dependent inflow of the successor simulation. The above procedure is the conventional approach for precursor simulation for wind farms by Churchfield, Lee, Michalakes, and Moriarty, 2012 and Churchfield, Lee, Moriarty, et al., 2012. Note that Stipa, Ajay, et al., 2024a has developed a novel hybrid off-line-concurrent precursor method. It is argued that the novel method is better suited for simulating atmospheric gravity waves. However, the method needs to be paired with streamwise periodic boundary conditions and fringe regions. The associated computational costs of the fringe regions are undesired, and since it is believed that wave reflection can be sufficiently confined, the conventional approach combined with inflow-outflow boundary conditions is applied. During the precursor simulation, the flow velocity and direction are prescribed at hub height and the potential temperature distribution is enforced by a temperature controller. The domain of the precursor is 6 by 6 by $1\,\mathrm{km}$ in the streamwise, spanwise, and height directions respectively.

4.6.3. Successor Domain

Simulation of wind farm-atmospheric gravity wave interaction requires careful design of the successor domain, to mitigate problems mainly related to wave reflection. Domain design consists of selecting the proper dimensions of the physical domain, the selection of adequate boundary conditions, the selection and sizing of the relevant damping layers, and the mesh design, all of which will be discussed in the same order below.

The physical domain is the part of the successor domain where the variable fields are representative of reality. Here, the solution is not damped in any way. To size the domain, the work of M. A. Khan et al., 2024 and M. Khan et al., 2024 can be used. The domain height should be at least one maximum vertical wavelength plus the capping inversion height. The former can be calculated using Equation 4.8, which derives from linear theory (Lanzilao and Meyers, 2024). Together with the capping inversion height and some margin, the physical domain height is $5750\,\mathrm{m}$.

$$\lambda_z = \frac{2\pi U_g}{N} = 5115\ m \tag{4.8}$$

Next, the domain length is sized using M. Khan et al., 2024 and Lanzilao and Meyers, 2024. The resulting domain length is $23\,000\,\mathrm{m}$, where the start of the wind farm is exactly in the middle of the physical domain. Finally, the desired domain width would be the width of the wind farm, plus ten diameters of extra width on each side, following Lanzilao and Meyers, 2024. For the simulations in the present study, the resulting domain width would be $13\,285\,\mathrm{m}$ in the extreme case, or $12\,480\,\mathrm{m}$ in the most common case. However, it is a requirement that the successor domain width is an integer multiple of the precursor domain width since this is the only way that the inflow can be guaranteed to have steady-state turbulence statistics. A domain width of $18\,000\,\mathrm{m}$ would be unfeasible in terms of computational costs, and hence the domain width is selected to be

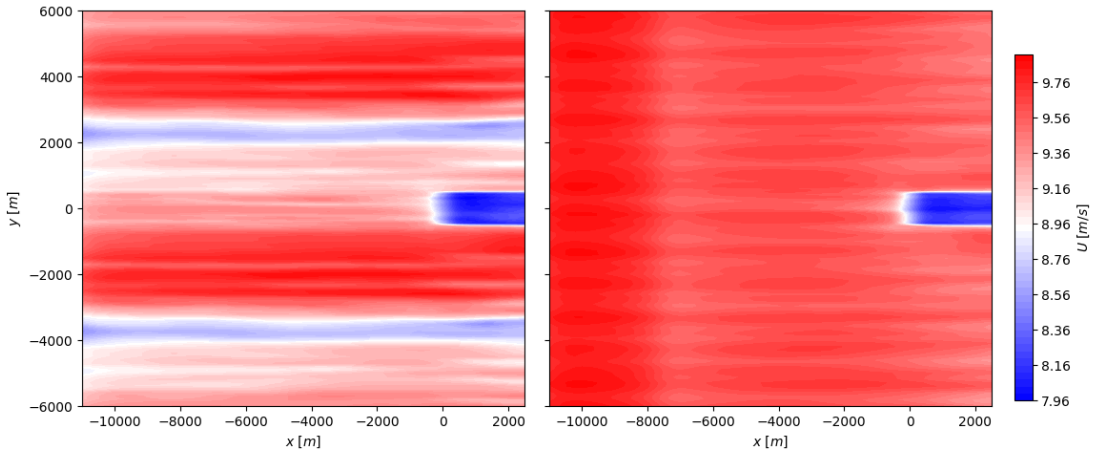

Figure 4.12: Average streamwise velocity fields at hub height for LES simulations of small wind farm canopies using coarse meshes. On the left, streaks due to the interface between two lateral boundaries of the precursor data are clearly visible. On the right, shifting the inflow using the methodology in Munters et al., 2016 solves the problem, and no streaks are visible anymore in the average data.

$12\,000\,\mathrm{m}$. In Section 5.5 this assumption is investigated and validated.

Table 4.2 presents an overview of the boundary conditions on the different patches of the successor domain. The inlet and outlet boundaries are `kLeft` and `kRight` respectively. At the inlet, the `inletFunction` is used, which turns the inflow slices from the precursor simulation into usable inflow for the successor. This is primarily due to the fact that there is a mismatch in the domain size of the precursor and successor. First of all, the solution is extrapolated in the z-direction using the top ten cells of the precursor inflow slices. It is allowed to do so since the free atmospheric lapse rate is constant and therefore the solution in the top ten cells is representative for the free atmosphere (given that the top ten cells are sufficiently high to be in the free atmosphere). As mentioned before, the domain of the successor needs to be an integer multiple of the precursor. In the present study, that means that the precursor data is repeated once in the lateral direction (although one of the two precursor domains is split by the lateral periodic boundary). This poses a problem at the interfaces of the two precursor domains since streaks will form here due to a mismatch of the solution on the two lateral boundaries. The streaks are clearly visible in the left average streamwise velocity field in Figure 4.12, where the results of an LES simulation with a coarse mesh and a small wind farm canopy are shown. To solve the problem, the approach of shifted boundary conditions from Munters et al., 2016 is applied, which is readily integrated into TOSCA. Here, the inflow is shifted in the spanwise direction by some distance each timestep. Therefore, a shift 'velocity' can be defined, which is set to $1.5\,\mathrm{m\,s^{-1}}$ in the present study, following Stipa, 2024, such that each cell has traversed the domain width at least once. Note that no physical velocity is introduced into the solution. Rather, a precursor cell that previously fed the inflow to the lateral station y_1 will after a certain Δt feed the inflow to the lateral station y_2, which is located at some Δy from y_1. The impact on the average velocity can be seen on the right in Figure 4.12, and it can be concluded that the streaks have disappeared. To enforce the outlet of the domain, `zeroGradient` boundary conditions are used. For the lateral, top, and bottom boundaries, the validation runs from Stipa, Ajay, et al., 2024a are followed. The lateral boundaries for all variables use periodic boundary conditions. It is not possible to apply an inlet-outlet boundary condition pair to the lateral boundaries since flow would flow both in and out of the lateral boundaries, which is difficult to implement numerically. Finally, the boundary conditions for the top and bottom of the domain are different for each variable. The temperature boundary conditions are `zeroGradient` and `fixedGradient` for the bottom and top respectively, to match the temperature profile in the ABL, and the lapse rate in the free atmosphere. Next, the velocity at the ground is enforced by prescribing the wall shear stress. As discussed in Stipa, Ajay, et al., 2024a, this is done through the similarity theories of Monin and Obukhov, 1954 and Paulson, 1970. At the top, a `slip` boundary condition is applied. The eddy viscosity is enforced to be zero at the top and bottom of the domain.

The next step in the domain design is the selection and sizing of the appropriate damping layers. Here, the recommendations in the work of M. A. Khan et al., 2024 and M. Khan et al., 2024 are followed. Firstly, it can be noted that no fringe regions are needed since inflow-outflow boundary conditions are used in the streamwise direction. It is however important that the waves are damped. As the aforementioned works note, Rayleigh damping layers (Klemp and Lilly, 1978) are needed at the domain's inlet, top, and outlet. However, for simulations with only a few flowthroughs, which is the case in the present study, the outlet RDL can be omitted. The top RDL should be able to accommodate one maximum vertical wavelength. Therefore, with some mar-

Table 4.2: Overview of the boundary conditions for velocity (`U`), potential temperature (`T`) and eddy viscosity (`nut`) on the different patches of the successor domain. `iLeft` and `iRight` correspond to the lateral boundaries, `jLeft` and `jRight` to the bottom and top boundaries respectively, and `kLeft` and `kRight` to the inlet and outlet boundaries respectively. The details on the implementation of the boundary conditions can be found in Stipa, 2024.

	iLeft	**iRight**	**jLeft**	**jRight**	**kLeft**	**kRight**
U	periodic	periodic	velocityWallFunction	slip	inletFunction	zeroGradient
T	periodic	periodic	zeroGradient	fixedGradient	inletFunction	zeroGradient
nut	periodic	periodic	fixedValue	fixedValue	inletFunction	zeroGradient

gin, the top RDL is $5250\,\mathrm{m}$ high, spanning the entire top of the successor domain. The inlet RDL extends $3500\,\mathrm{m}$ into the domain, and spans the inflow plane of the free atmosphere. The inlet RDL is smaller than the top RDL since the damping at the inlet is paired with the advection damping layer. The damping function goes back to one over the capping inversion, such that the flow in the ABL is not damped. This is because the inlet RDL damps the flow towards the geostrophic wind vector, which needs to be determined from the precursor simulation. This is essential, as a deviation from the initial condition will give inertial oscillations in the free atmosphere (Stipa, Ajay, et al., 2024a). Naturally, the flow in the ABL is different from the free atmosphere, and should not be damped towards the aforementioned vector. As demonstrated in M. Khan et al., 2024, the damping coefficient in the RDLs should be one to ten times the Brunt-Väisälä frequency. For low Froude numbers, it is desired to be closer to ten, and hence the damping coefficient ν_{RDL} is selected to be $0.1\,\mathrm{s}^{-1}$. Between the inlet RDL and the physical domain, there is an advection damping layer (ADL). The buffer zone of the ADL is the region where the damping function is zero, as can be seen in Lanzilao and Meyers, 2023. M. Khan et al., 2024 advises that this buffer zone has the same length as the trapped wavelength. Since the trapped wavelength is not known a priori, it needs to be estimated for example with a linear model. The trapped wavelength is expected to be $4000\,\mathrm{m}$ maximum (M. Khan et al., 2024). The regions in which the advection damping layer function goes back to one are in front and behind the buffer zone and extend $1000\,\mathrm{m}$ further than the buffer zone. The transitioning region in front of the ADL overlaps with the inlet RDL. No damping regions have been implemented on the lateral boundaries. Depending on the inversion Froude number, the interfacial waves on the sides of the wind farm will either exit through the lateral or streamwise boundaries. This can be predicted by using the angle that the characteristic lines make with the x-axis, using the relationship from linear theory as described in Allaerts and Meyers, 2019, and as shown in Equation 4.9.

$$\alpha = \arctan\left(1/\sqrt{Fr_i^2 - 1}\right) \tag{4.9}$$

It can be deduced that for low supercritical Froude numbers (such as the one corresponding to the atmospheric state used in the present study), the angle is large, indicating that the characteristic lines exit through the lateral boundaries. As a consequence, the interfacial waves are reintroduced on the other side of the domain. However, since the Coriolis parameter is small, it is assumed that the flow is sufficiently symmetric in the $x-y$-plane such that the interaction between the incoming and reintroduced wave acts as a mirror. Consequently, the reintroduction will not cause contamination of the solution. A full overview of the successor domain and its damping layers is presented in Figure 4.13. The presented layout is valid for every spanwise station of the domain, with the exception of the wind farm being finite.

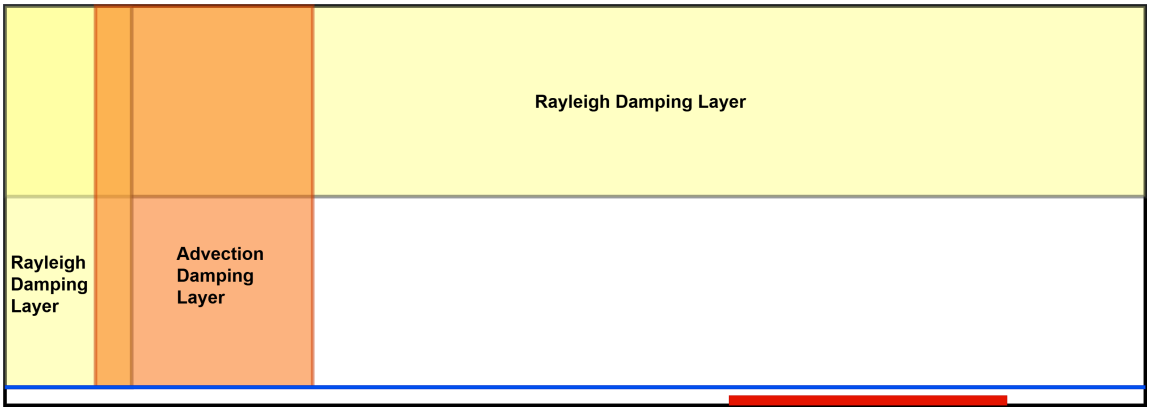

Figure 4.13: Overview of the successor domain, with the inlet and top Rayleigh damping layers in yellow, the advection damping layer in orange, the capping inversion in dark blue, and the wind farm in red. Drawing is to scale.

Finally, the mesh resolution needs to be determined. TOSCA allows for mesh grading in all directions, allowing for the mesh resolution to be optimized using the requirements for each region of the domain. Unfortunately, it is unfeasible to do a grid convergence study, given the large computational costs of an LES with a fine mesh. However, many LES have been performed before, so the literature can be followed to give an indication of the necessary resolutions. Specifically, the approach in Stipa, Ajay, et al., 2024a is followed. Here, the mesh is graded in all three directions. In the vertical direction, the mesh in the ABL will have a resolution of $10\,\mathrm{m}$. It will be graded over the thickness of the capping inversion to reach $5\,\mathrm{m}$ in the middle, and back to $10\,\mathrm{m}$ afterwards. Next, the mesh is graded to $200\,\mathrm{m}$ over the physical domain, which will be the resolution in the top RDL. This coarse resolution is sufficient to capture the large-scale wavelengths in the free atmosphere. In the spanwise direction, the mesh resolution is $12.5\,\mathrm{m}$ through the wind farm and is graded on both sides to $20\,\mathrm{m}$. Finally, the mesh is graded from $200\,\mathrm{m}$ to $30\,\mathrm{m}$ over the buffer zone of the ADL. The inlet RDL consequently has a $200\,\mathrm{m}$ resolution, following the same approach as the top RDL, and the rest of the domain, including the wind farm, a $30\,\mathrm{m}$ resolution. Note that Stipa, Ajay, et al., 2024a applies a high resolution at the inlet and outlet of the domain since fringe regions are used. Fringe regions are not used in this study and hence the high resolution is not needed. The mesh resolutions and cell numbers are summarized in Table 4.3. The resulting mesh is displayed in Figure 4.14, clearly showing the regions with the highest mesh resolution. Note that the mesh is equal for all LES simulations since the wind farms are roughly equal in size. The total cell count is $131\,686\,896$.

Table 4.3: Mesh resolution in the streamwise, spanwise, and vertical directions respectively, showing the interval size, the grid resolution, the number of cells, and the common ratio between cell sizes.

$x_s\ [m]$	$x_e\ [m]$	$\Delta x\ [m]$	$N\ [-]$	$r\ [-]$
-20000	-16600	200	17	1
-16600	-12500	$200-30$	45	0.958
-12500	11500	30	800	1
$y_s\ [m]$	$y_e\ [m]$	$\Delta y\ [m]$	$N\ [-]$	$r\ [-]$
-6000	-5000	20	50	1
-5000	-4000	$20-12.5$	63	0.992
-4000	4000	12.5	640	1
4000	5000	$12.5-20$	63	1.008
5000	6000	20	50	1
$z_s\ [m]$	$z_e\ [m]$	$\Delta z\ [m]$	$N\ [-]$	$r\ [-]$
0	400	10	40	1
400	500	$10-5$	14	0.947
500	600	$5-10$	14	1.056
600	5800	$10-200$	81	1.038
5800	11000	200	26	1

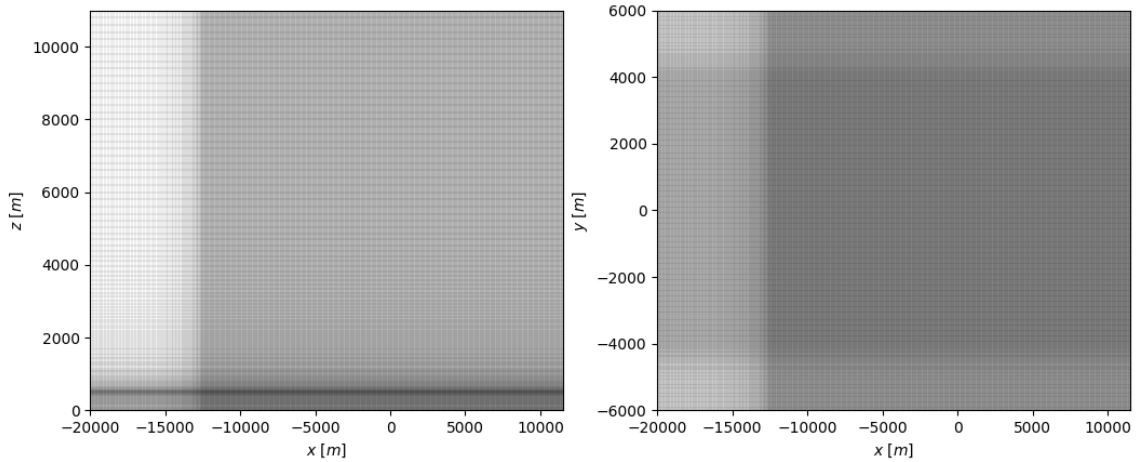

Figure 4.14: Successor domain discretization in the $x-z$-plane (left) and $x-y$-plane (right). The higher resolution in the capping inversion and wind farm is clearly visible.

4.6.4. Successor Simulation Control

The present section will discuss the parameters that control the successor simulation, such as the time stepping, numerical schemes, and sampling locations. First of all, the total simulation time is based on the amount of flowthroughs. The reference velocity is $9.21\,\mathrm{m\,s^{-1}}$ and the total domain length is $31\,500\,\mathrm{m}$, and the consequent simulation time will be $10\,000\,\mathrm{s}$, such that three flowthroughs are achieved. The time step will be CFL-controlled, based on a Courant number of 0.9. The numerical schemes used for the velocity and temperature are the backward Euler method. This method is preferred for longer CFL-controlled simulations, as discussed in Stipa, 2024. Furthermore, the divergence scheme is the weighted central upwind scheme, since a graded mesh requires a weighted scheme. The main outputs of the simulations are the turbines' power outputs, and the slices made in the domain where the two-dimensional data is saved (and averaged). Averaging takes place from the second flowthrough onwards (i.e. from $3500\,\mathrm{s}$ onwards). The domain is sliced at different spanwise, streamwise, and vertical locations. These locations are positioned such that they are representative of the successor domain, for locations with or without turbines, in the ABL, capping inversion, or free atmosphere. Note that the specific coordinates can be found in Appendix B. Finally, a velocity controller is applied in the successor simulation to enforce the magnitude and direction of the velocity vector at hub height. Stipa, Ajay, et al., 2024a argues that a temperature controller should be applied to force the temperature profile since the temperature profile cannot develop over time due to the diurnal cycle. This approach is not adopted, since diurnal cycles are associated with onshore conditions (Stull, 1988). Thus, no temperature controller is applied.

4.7. Non-Dimensional Numbers

Non-dimensional numbers allow for a generalisation of the results, such that they can be used for farm layouts that are not present in the study. Ultimately, indicating trends versus non-dimensional numbers will give the most useful output of the research. The most important non-dimensional number that governs the behaviour of atmospheric gravity waves is the Froude number. In the literature, the definitions of the Froude number vary, which is why different Froude numbers that are significant to this study are listed below.

The first definition is presented in Equation 4.10 (M. Khan et al., 2024). Here, the geostrophic wind speed is divided by the Brunt-Väisälä frequency and the characteristic length of the farm. This non-dimensional number is the ratio between the advection of the freestream flow, and the upward propagation of the internal waves, or in other words, the ratio between the inertia of the flow and the buoyancy force (M. Khan et al., 2024). Therefore, the Froude number is a direct measure of the direction of the internal waves and is hence especially useful to investigate what the characteristic length scale should be for a certain wind farm.

$$Fr = \frac{U_g N}{L} \tag{4.10}$$

Then, there is the inversion Froude number. This non-dimensional number determines the behaviour of the interfacial gravity waves on the inversion layer. The inversion Froude number can be determined using the bulk velocity in the inversion layer, the reduced gravity, and the inversion layer height, as can be seen in Equation 4.11, originally defined in Smith, 2010. However, the original definition uses the bulk velocity as its velocity scale. Stipa, Ahmed Khan, et al., 2024 argues that the proper velocity scale to use is the geostrophic velocity, and this approach will be adapted in the present study. The corresponding inversion Froude number is 1.03 and it is constant for all simulations. It is useful to define the sub- and supercritical flow regimes, corresponding to $Fr_i < 1$ and $Fr_i > 1$ respectively. If the flow regime is subcritical, the interfacial gravity waves can travel upstream and downstream, as their propagation speed is higher than the speed of the flow. If it is supercritical, the waves only travel downstream, and the perturbations in the flow field upstream are only due to the internal gravity waves (Stipa, Ajay, et al., 2024b).

$$Fr_i = \frac{U_g}{\sqrt{g' H}} \qquad \text{where} \qquad g' = g\Delta\theta/\theta_0 \tag{4.11}$$

As mentioned in Section 4.2, the geostrophic velocity is not equal for the MSC and LES simulations. As a result, the inversion Froude number is 1.27 and 1.03 respectively. Qualitative comparison can be directly made since both inversion Froude numbers are supercritical. For quantivative comparison, the wave characteristics must first be scaled.

Finally, the Prandtl number of the flow will be at its standard value of 0.71.

5

Results

The present chapter serves to display and discuss the results that are acquired towards answering the research questions. Firstly, Section 5.1 aims to find the correct characteristic length scales to use in the definition of the Froude number and inversion Froude number for sparse and non-uniform farms. Next, Section 5.2 elaborates upon the atmospheric gravity wave excitation as a result of wind farm layout, and consequently discusses the wave characteristics. Then, Section 5.3 shows the wind farm performance as a result of the AGW feedback in the form of non-local, wake, and farm efficiencies. Subsequently, results relating to farms with a constant number of turbines are displayed in Section 5.4. Finally, Section 5.5 aims to validate the results and choices made in the methodology, and compare some results to the literature.

5.1. Characteristic Length

As discussed in Section 4.7, both the Froude number and inversion Froude number include a length scale. In most of the literature, the length scale is the length of the farm, and the capping inversion height respectively. Subsection 5.1.1 and Subsection 5.1.2 will test those choices for sparse and non-uniform farms.

5.1.1. Length Scale of Froude Number for Sparse and Non-Uniform Farms

As mentioned before, it is often assumed that the proper length scale to be used in the Froude number is the length of the wind farm. However, the present section investigates whether this assumption is still valid for sparse farms, i.e. where the turbine spacing is very large. It is important to keep in mind that the farms in the subsequent discussion are equal in length. Figure 5.1 through Figure 5.4 show the vertical velocity field of the free atmosphere for square wind farms with increasing power density. Note that the lower vertical limits of the plots differ since the influence of the wind farm reaches higher for different layouts. Moreover, the results in the Rayleigh damping layer are taken into account, since it is the direction of the wave that is of interest here. Based on the local maxima and minima, the directions of the wavetrains generated by the beginning and end of the wind farm are estimated. The Froude number in its definition used in this study, is the ratio of the advection speed over the propagation speed of the internal gravity wave (IGW). Therefore, it is also a measure of the angle that the IGW makes with the horizontal, as the propagation direction is upwards, and the advection direction of the mean flow is downstream, as shown in Equation 5.1. Note that it is not an equality, since the Brunt-Väisälä frequency is the maximum frequency an oscillating air parcel can take, and thus it might not be the actual frequency (Nappo, 2013). Furthermore, the local velocity might differ from the magnitude of the geostrophic wind.

$$\tan\beta \sim Fr^{-1} \tag{5.1}$$

The direction of the internal gravity waves is equal for the first three wind farms with turbine spacings of $2D$, $4D$, and $8D$, which indicates that the farm length is the proper length scale to use for the Froude number. However, the wavetrains are tilted back further for the farm with a turbine spacing of $16D$. For this case, the ratio between the farm lengths and wave directions can be used to determine the proper length scale. Here, two assumptions need to be made. Firstly, it must be assumed that indeed the farm length is the correct length scale for the farms in Figure 5.1, Figure 5.2, and Figure 5.3. Secondly, it is assumed that the proportionality constant of Equation 5.1 is not dependent on the direction of the IGW, on the wave characteristics, or on the turbine spacing. Furthermore, it must be noted that the interaction between the two wavetrains in the free atmosphere can have an effect on the characteristics of the waves. Consequently, the direction β must only be used in a qualitative sense, as it might be weakly defined for cases where the two wavetrains are heavily

interacting. Moreover, only the most upstream wavetrain is used for calculations, since the second wavetrain is influenced by the interaction between the two wavetrains. Of course, the first wavetrain is also affected by the interaction, but it is assumed that this interaction is less pronounced and that the direction of the wavetrain can thus be used for the subsequent analysis. Then, the length scale can be calculated using Equation 5.2. Here, index 2 indicates the farm in Figure 5.4 (i.e. the vertical velocity field of simulation PD4LES), and index 1 indicates any of the other three (i.e. the vertical velocity field of simulation PD1LES, PD2LES, or PD3LES).

$$L_2 = L_1 \frac{\tan \beta_2}{\tan \beta_1} \tag{5.2}$$

The resulting length scale is between $2900\,\mathrm{m}$ and $3400\,\mathrm{m}$, given the farm length of $7680\,\mathrm{m}$. Since the turbine spacing is $16D$, equaling $3840\,\mathrm{m}$, it is deemed plausible that the correct length scale for very sparse farms is the turbine spacing. The streamwise and spanwise turbine spacing are equal, and therefore it cannot be determined whether the length scale is the effective turbine spacing or the streamwise turbine spacing.

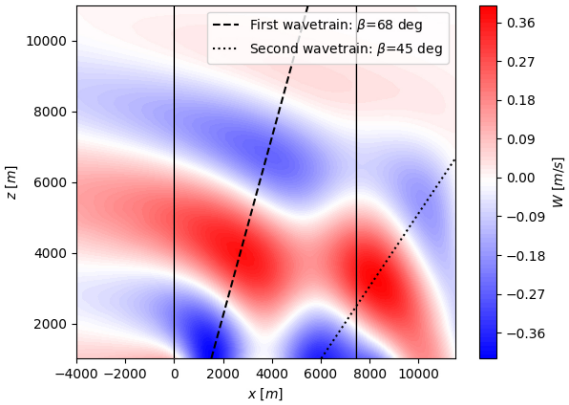

Figure 5.1: Vertical velocity field of the free atmosphere of simulation PD1LES, which has a square farm with a power density of $73\,\mathrm{MW\,km^{-2}}$. The directions of the first and second wavetrain are indicated. The solid black lines mark the start and end of the wind farm.

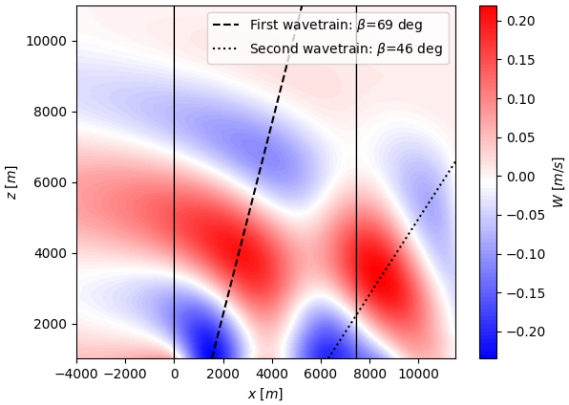

Figure 5.2: Vertical velocity field of the free atmosphere of simulation PD2LES, which has a square farm with a power density of $21\,\mathrm{MW\,km^{-2}}$. The directions of the first and second wavetrain are indicated. The solid black lines mark the start and end of the wind farm.

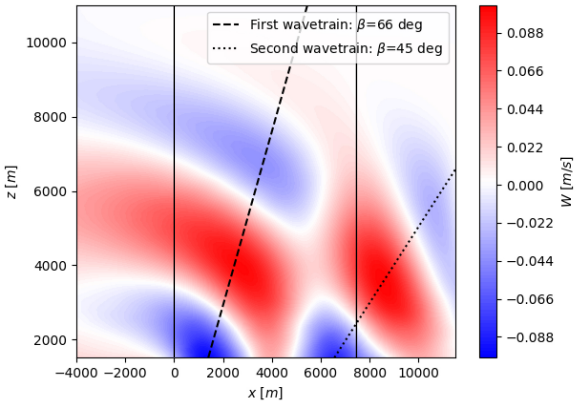

Figure 5.3: Vertical velocity field of the free atmosphere of simulation PD3LES, which has a square farm with a power density of $6\,\mathrm{MW\,km^{-2}}$. The directions of the first and second wavetrain are indicated. The solid black lines mark the start and end of the wind farm.

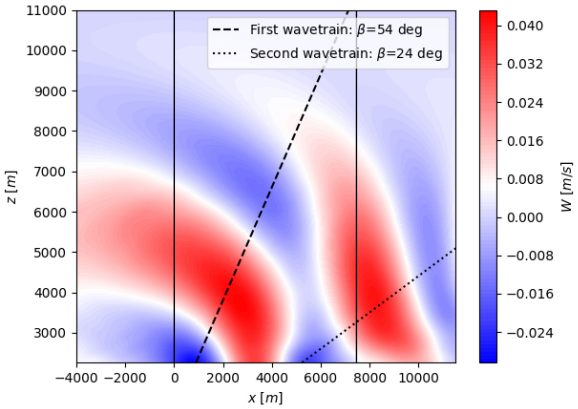

Figure 5.4: Vertical velocity field of the free atmosphere of simulation PD4LES, which has a square farm with a power density of $2\,\mathrm{MW\,km^{-2}}$. The directions of the first and second wavetrain are indicated. The solid black lines mark the start and end of the wind farm.

An argument that further strengthens the idea of the wind farm behaving as an entity for small turbine spacings is that the two wavetrains are clearly defined for these cases. When a wind farm is behaving as an entity, it means that the turbines all together form a thrust field. Then, there is a wavetrain generated where the thrust field changes, i.e. at the beginning and the end of the farm. When the turbines are spaced further from each

other, the thrust field cannot be viewed as continuous. Although the strongest disturbances to the thrust field (which again are the beginning and end of the wind farm) still cause two wavetrains that can be separated, the behaviour is much more complex, as is visible in Figure 5.4, hinting at the interaction between the wavetrains.

A similar approach can be applied to find the characteristic length scale for the Froude number for non-uniform farms. In Figure 5.5, Figure 5.6, and Figure 5.7, the vertical velocity field of the free atmosphere is shown for a square six by six farm that has a $5D$ turbine spacing. The square farm is rotated $0\,\mathrm{deg}$, $22.5\,\mathrm{deg}$, and $45\,\mathrm{deg}$ with respect to the freestream respectively. Again, the direction of the two wavetrains generated by the beginning and end of the wind farm are shown. Note that all three farms are assumed to be an entity. After all, the turbine spacing is less than $8D$. One could argue that the turbine spacing is not $5D$ anymore when the farm is rotated. However, in the case of a $45\,\mathrm{deg}$ rotation, the spacing between turbines in the streamwise direction is approximately $7D$, still lower than the farm in Figure 5.3. Consequently, the three simulations can be used to determine the characteristic length scale of a non-uniform farm. To do so, Equation 5.1 and Equation 5.2 will be reused. It is assumed that the farm length is the correct length scale for the farm in Figure 5.5. Furthermore, it is again assumed that the proportionality constant of Equation 5.1 is not dependent on the direction of the IGW, on the wave characteristics, or on the turbine spacing. The length scale of the farm in Figure 5.7 can then be calculated to be $4400\,\mathrm{m}$. It is suggested that the proper length scale of the non-uniform farm is the average length over the span of the farm, which is $4250\,\mathrm{m}$ for the $45\,\mathrm{deg}$ rotation. This can be calculated using Equation 5.3, where y_{min} is the minimum spanwise coordinate of the farm, y_{max} the maximum spanwise coordinate, and L_f the length of the farm in the streamwise direction. In other words, it is the total farm area divided by the maximum farm width.

$$L = \frac{\int_{y_{min}}^{y_{max}} L_f(y)dy}{y_{max} - y_{min}} \tag{5.3}$$

It must be noted that for the farm in Figure 5.6, which is rotated by $22.5\,\mathrm{deg}$, the internal waves have the same direction as in Figure 5.5. In this case, it is assumed that the direction is not changed significantly due to the fact that the flow is turned by the Coriolis effect. This causes the flow to be aligned with the original farm length. Note that this effect is not present for the non-rotated wind farm, as can be appreciated from the Figure 5.8, where it is shown from left to right that the Coriolis effect gets stronger when the farm is rotated more because the velocity vector at hub height is turned due to a larger spanwise velocity. As a consequence, the aforementioned estimated length scale for a rotated farm is overestimated, causing it to be even closer to the average farm length from Equation 5.3.

5.1.2. Length Scale of Inversion Froude Number for Sparse and Non-Uniform Farms

The inversion Froude number is the ratio between the velocity of the flow versus the propagation speed of the interfacial waves. To quantify the latter, the capping inversion height is used as a characteristic length scale. The present section aims to test this hypothesis for sparse and non-uniform farms. The vertical velocity field has previously been used to display the internal waves. Due to the complex interaction between the internal and interfacial waves, which is dependent on their relative strength, the displacement of the capping inversion is a better variable to study interfacial waves. After all, it is a perturbation of the capping inversion height that is the source of the interfacial wave. As a result, the atmospheric boundary layer displacement η is shown in Figure 5.9 through Figure 5.12 for the farms that have a varying power density, and in Figure 5.13 through Figure 5.15 for the farms that have a varying orientation. The boundary layer displacement is determined by tracing a streamline far upstream at the capping inversion height. This capping inversion height is subsequently subtracted. The interfacial wavelength can be determined a priori using linear theory using Equation 5.4, as shown in Lanzilao and Meyers, 2024. Here, k_x is the wavenumber and U_B is the bulk velocity in the ABL. The latter can be determined to be $9.48\,\mathrm{m\,s^{-1}}$ using the MSC model. The resulting wavelength is approximately $4800\,\mathrm{m}$. As shown in Section 4.7, the inversion Froude number uses the interfacial-wave phase speed in its definition. This speed is $\sqrt{g'H}$ following shallow-water wave theory, according to Sutherland, 2010. The formulation is valid when the forcing length scale is larger than $4\pi H$, where H is the capping inversion height. It can be noted that the wavelength of the interfacial wave determined by Equation 5.4 and the inversion Froude number that is characteristic of the interfacial wave behaviour are both independent of any parameters related to the wind farm layout. Therefore, when the wavelength of the interfacial waves deviates from the expected value, the assumption of the forcing length must not be valid anymore.

$$\lambda_x = \frac{2\pi}{k_x} \qquad \text{where} \qquad k_x = \frac{g\Delta\theta}{2U_B^2\theta_0} + \frac{N^2\theta_0}{2g\Delta\theta} \tag{5.4}$$

From Figure 5.9, Figure 5.10, Figure 5.13, and Figure 5.14, it can be observed that the wavelength of the interfacial wave seems independent of the locations of the turbines, which are indicated with the dashed lines.

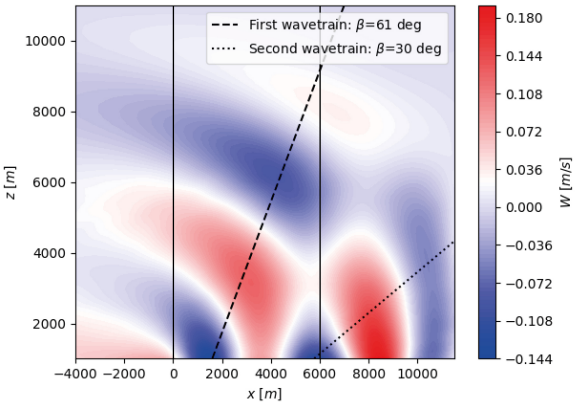

Figure 5.5: Vertical velocity field of the free atmosphere of simulation SFSNU1LES, which is rotated $0\,\mathrm{deg}$ with respect to the freestream and has a power density of $15\,\mathrm{MW\,km^{-2}}$. The directions of the first and second wavetrain are indicated. The solid black lines mark the start and end of the wind farm.

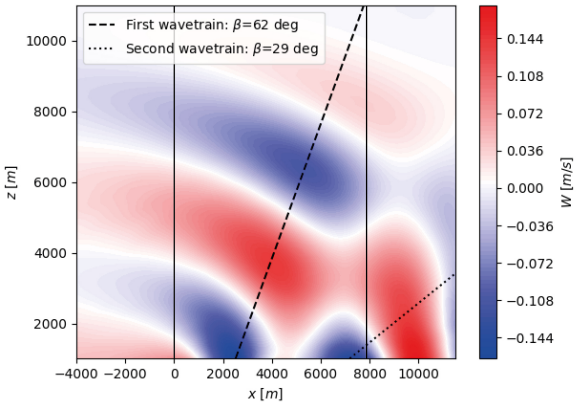

Figure 5.6: Vertical velocity field of the free atmosphere of simulation SFSNU2LES, which is rotated $22.5\,\mathrm{deg}$ with respect to the freestream and has a power density of $15\,\mathrm{MW\,km^{-2}}$. The directions of the first and second wavetrain are indicated. The solid black lines mark the start and end of the wind farm.

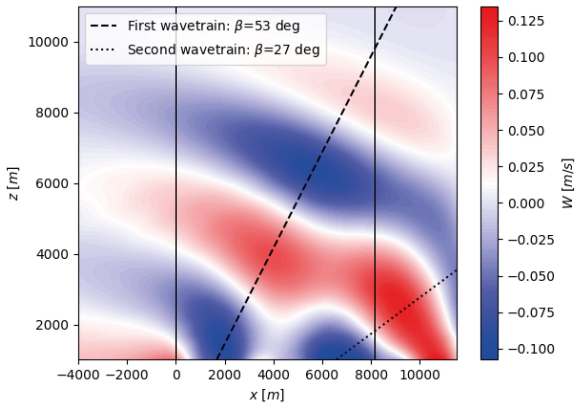

Figure 5.7: Vertical velocity field of the free atmosphere of simulation SFSNU3LES, which is rotated $45\,\mathrm{deg}$ with respect to the freestream and has a power density of $15\,\mathrm{MW\,km^{-2}}$. The directions of the first and second wavetrain are indicated. The solid black lines mark the start and end of the wind farm.

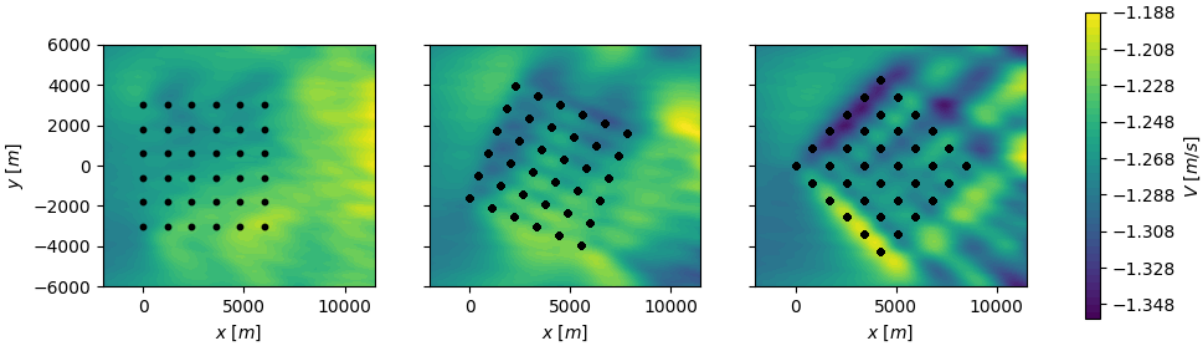

Figure 5.8: Spanwise velocity fields for the free atmosphere ($z = 600\,\mathrm{m}$) for simulations SFSNU1LES, SFSNU2LES, and SFSNU3LES from left to right respectively. The turbine locations are marked with dots. When progressing to the right in the figure, it can be observed that the Coriolis effect gets stronger. Due to the larger spanwise velocity, the velocity vector at hub height is turned.

Indeed, the wavelengths range from $3700\,\mathrm{m}$ to $4200\,\mathrm{m}$, in the range of the predicted wavelength from linear theory. Within the length of the farm, there are two peaks in the boundary layer displacement. In the cases of Figure 5.11 and Figure 5.15, which have a turbine spacing of $8D$ and $7D$ respectively, the two peaks are

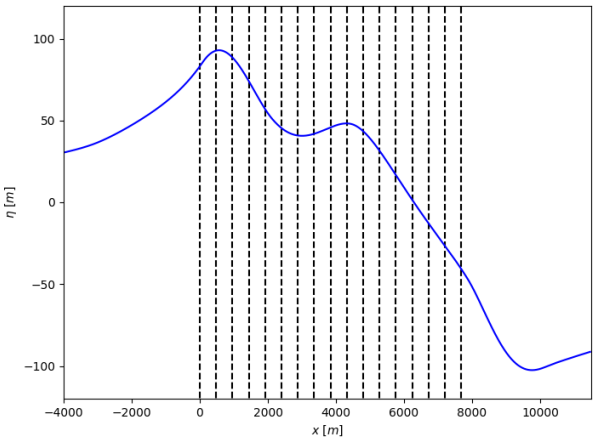

Figure 5.9: Atmospheric boundary layer displacement of simulation PD1LES, which has a square farm with a power density of $73\,\mathrm{MW\,km^{-2}}$. The locations of the turbine rows are marked.

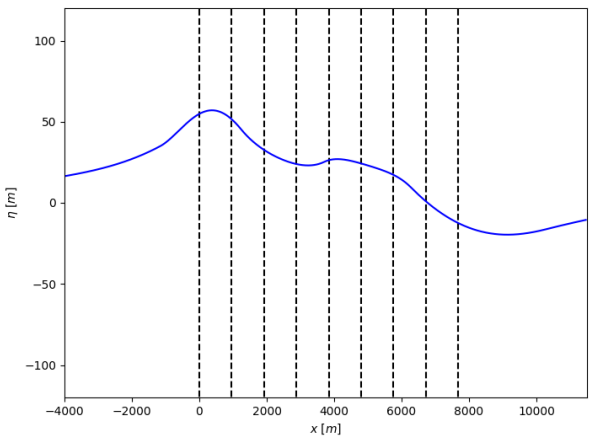

Figure 5.10: Atmospheric boundary layer displacement of simulation PD2LES, which has a square farm with a power density of $21\,\mathrm{MW\,km^{-2}}$. The locations of the turbine rows are marked.

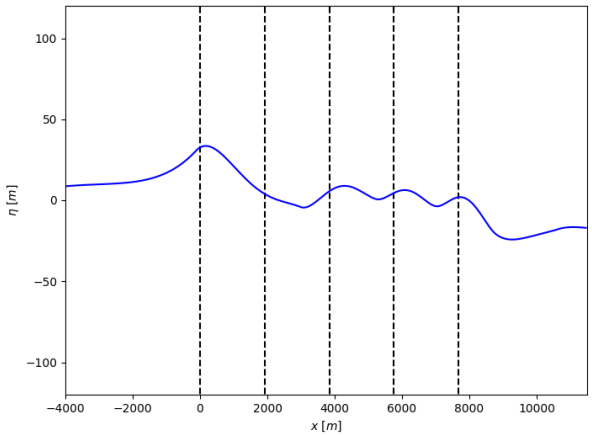

Figure 5.11: Atmospheric boundary layer displacement of simulation PD3LES, which has a square farm with a power density of $6\,\mathrm{MW\,km^{-2}}$. The locations of the turbine rows are marked.

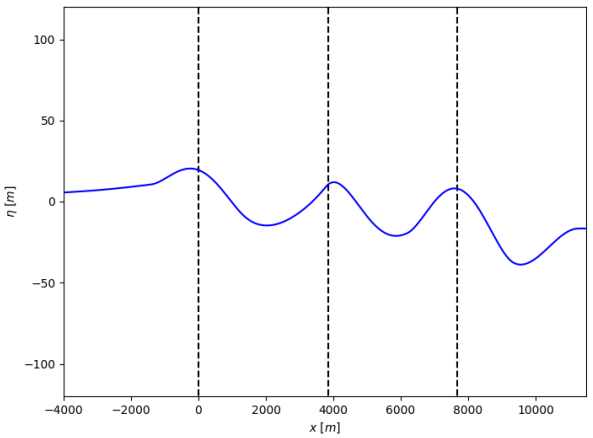

Figure 5.12: Atmospheric boundary layer displacement of simulation PD4LES, which has a square farm with a power density of $2\,\mathrm{MW\,km^{-2}}$. The locations of the turbine rows are marked.

still visible. However, the perturbations of the individual turbines start to be visible. The larger wavelength is $4100\,\mathrm{m}$ and $4300\,\mathrm{m}$, and thus still in the order of the predicted value. However, the smaller wavelength is $1700\,\mathrm{m}$ and $2100\,\mathrm{m}$ respectively, both in the order of the turbine spacing. Finally, for the farm of Figure 5.12, the wavelength is $3872\,\mathrm{m}$, again in the order of the turbine spacing. Although it is also in the order of the predicted wavelength from linear theory, it can be observed that the last row of turbines perturbs the ABL height, an effect that is absent in the other cases.

The characteristic length scale for farms with large spacings can be determined by taking the ratio of the interfacial wavelengths (which are determined using the atmospheric boundary layer displacement), and assuming that the capping inversion height is the correct length scale for farms that behave as an entity. This assumption is deemed justified since the wavelengths are in the order of the expected wavelengths determined using the theory that is based on the capping inversion height being the correct length scale. To take the ratio, the average of the farm-independent interfacial wavelength is used, which is approximately $3900\,\mathrm{m}$. Note that the wavelength from Figure 5.14 is not used, since it is not clear what the effective turbine spacing is in this case due to the wind farm not having clearly defined rows. Consequently, it cannot be determined whether the measured wavelength is in the order of the predicted value or in the order of the turbine spacing. If the ratio between the measured farm-dependent wavelength and the measured farm-independent wavelength is multiplied by the capping inversion height, i.e. the original length scale, new length scales of $280\,\mathrm{m}$, $220\,\mathrm{m}$, and $500\,\mathrm{m}$, for turbine spacings of $7D$, $8D$, and $16D$ respectively are obtained. Lanzilao and Meyers, 2024 suggests that the length scale to be used for the perturbations related to the turbine spacing is Equation 5.5. This length scale originates from deep-water wave theory. Here, S_e is the equivalent turbine spacing. Using the aforementioned turbine spacings, length scales of $250\,\mathrm{m}$, $280\,\mathrm{m}$, and $410\,\mathrm{m}$ for turbine spacings of $7D$,

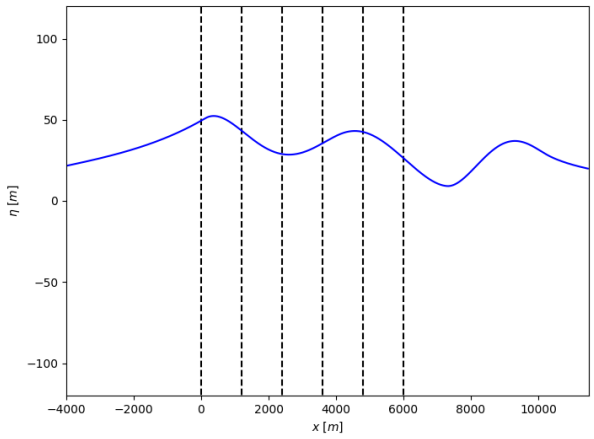

Figure 5.13: Atmospheric boundary layer displacement of simulation SFSNU1LES, which is rotated $0\,\mathrm{deg}$ with respect to the freestream and has a power density of $15\,\mathrm{MW\,km^{-2}}$. The locations of the turbine rows are marked.

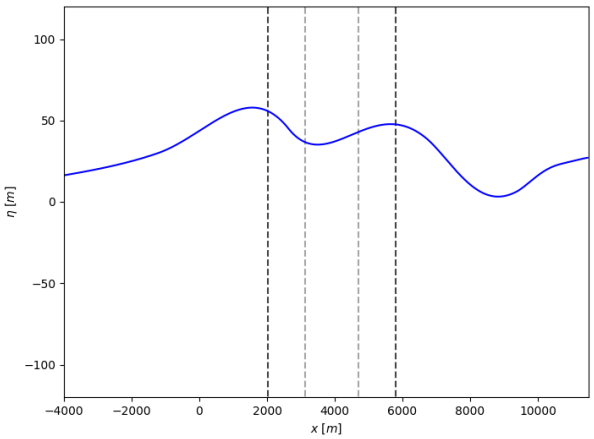

Figure 5.14: Atmospheric boundary layer displacement of simulation SFSNU2LES, which is rotated $22.5\,\mathrm{deg}$ with respect to the freestream and has a power density of $15\,\mathrm{MW\,km^{-2}}$. The locations of the turbines that are less than $500\,\mathrm{m}$ from the centerline are marked, with the opacity of the lines indicating the distance from the centerline.

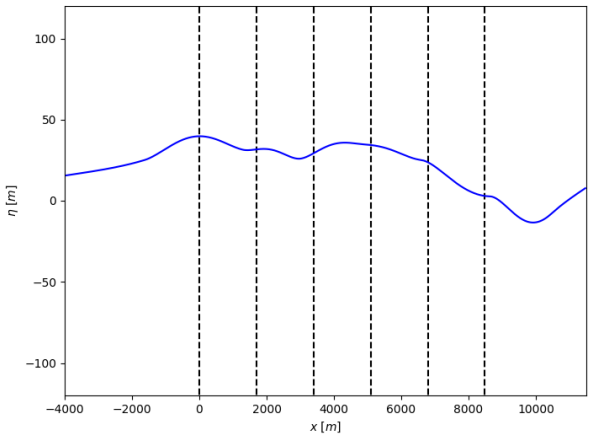

Figure 5.15: Atmospheric boundary layer displacement of simulation SFSNU3LES, which is rotated $45\,\mathrm{deg}$ with respect to the freestream and has a power density of $15\,\mathrm{MW\,km^{-2}}$. The locations of the turbines in the centerline are marked.

$8D$, and $16D$ respectively are obtained. These match reasonably well with the aforementioned calculated values, and thus the proper length scale is suggested to be Equation 5.5. Indeed, this length scale is valid under the assumption that the length scale of the forcing (which is different from the characteristic length scale in this section), is smaller than H/π, indicating that the farm behaves as a set of individual turbines that each have their own forcing.

$$L = \frac{S_e}{2\pi}\tanh\left(\frac{2\pi H}{S_e}\right) \qquad \text{where} \qquad S_e = D\sqrt{s_x s_y} \tag{5.5}$$

As a consequence of the new length scale, the behaviour of the interfacial waves is governed by the deep-water inversion Froude number from Equation 5.6, as defined in Lanzilao and Meyers, 2024. Note that, as mentioned in Section 4.7, the velocity scale of the boundary layer is selected to be the geostrophic velocity U_g.

$$Fr_{i,dw} = \frac{U_g}{\sqrt{\frac{g' S_e}{2\pi}\tanh\left(\frac{2\pi H}{S_e}\right)}} \tag{5.6}$$

To further strengthen the argument that the wavelength that is visible is indeed due to the perturbations of the individual turbines associated with the deep-water inversion Froude number, two simulations using wind

farm canopies have been performed. A wind farm canopy is a simplified representation of the wind farm with individual turbines, where the influence of the wind farm as a whole is modelled by applying a continuous body force over a volume (Stipa, 2024). The volume is the bounding box of the turbine rotors, i.e. bounded by the wind farm dimensions in the $x-y$-plane, and bounded by the lowest and highest point of the rotor disk in the z-direction. The body force is quantified using the disk-based wind farm planform thrust coefficient c'_{ft} shown in Equation 5.7, which is an input to TOSCA as described in Stipa, 2024. Here, C'_T is the disk-based thrust coefficient (which is 1.523 based on the thrust coefficient), and s_x and s_y are the streamwise and spanwise turbine spacings respectively.

$$c'_{ft} = \frac{\pi C'_T}{4 s_x s_y} \tag{5.7}$$

Using turbine spacings of $2D$ and $16D$, the disk-based wind farm planform thrust coefficient is 0.299 and 0.005 respectively, which are supposed to represent the farms of simulations PD1LES and PD4LES. As expected, the behaviour in Figure 5.16 is equal to the atmospheric boundary layer displacement observed in Figure 5.9, showing the farm-independent interfacial wavelength. However, the perturbations due to the individual turbines observed in Figure 5.12 have disappeared in Figure 5.17, since the disturbance due to the wind farm is now continuous. Therefore, it is indeed the perturbations due to the individual turbines that were the cause of the smaller wavelength.

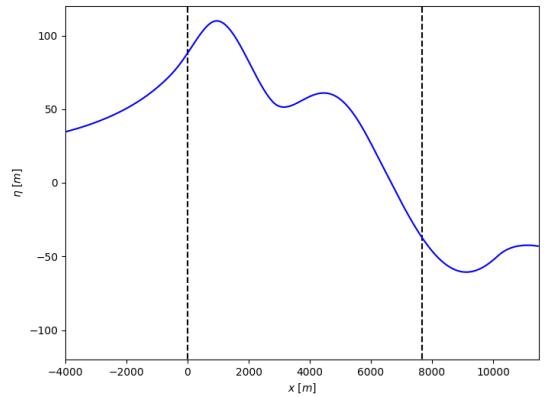

Figure 5.16: Atmospheric boundary layer displacement of a wind farm canopy simulation that matches a power density of $73\,\mathrm{MW\,km^{-2}}$ using $c'_{ft} = 0.299$. The start and end of the canopy are marked.

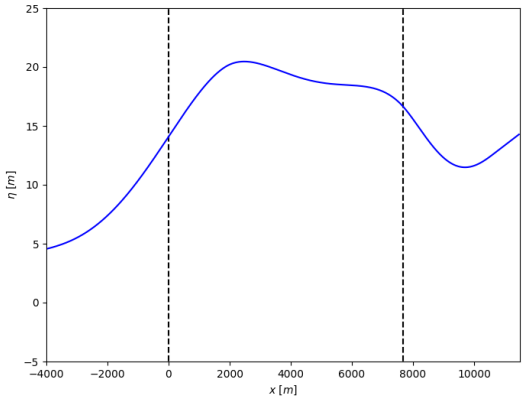

Figure 5.17: Atmospheric boundary layer displacement of a wind farm canopy simulation that matches a power density of $73\,\mathrm{MW\,km^{-2}}$ using $c'_{ft} = 0.005$. The start and end of the canopy are marked. Note that the vertical scale is enlarged.

5.2. Atmospheric Gravity Wave Excitation

The suite of simulations done with the MSC model will give an understanding of atmospheric gravity wave excitation as a result of wind farm layout. However, as discussed in Subsection 4.5.3, the results of the MSC model are depth-averaged, and consequently, it is not clearly defined whether the background velocity field is representative of the internal or interfacial waves or a superposition of both. Therefore, Subsection 5.2.1 investigates the observed behaviour to interpret the results correctly. Subsequently, the results per parameter are discussed in Subsection 5.2.2.

5.2.1. Interpretation of MSC Wave Type

To determine whether the interfacial or internal waves are dominantly appearing in the MSC results, the work by Allaerts and Meyers, 2019 is utilized. Since the inversion Froude number is supercritical, there will be V-shaped characteristic lines. These lines make an angle α_{lin} with the horizontal, where the angle is shown to be only dependent on the inversion Froude number and can be determined from linear theory using Equation 5.8 (Allaerts and Meyers, 2019). Note that originally β is used, but since that would interfere with the previously defined vertical direction of the internal waves, the present study adopts α as the symbol.

$$\alpha_{\text{lin}} = \arctan\left(\left(Fr_i^2 - 1\right)^{-1/2}\right) \tag{5.8}$$

Furthermore, as Lanzilao and Meyers, 2024 demonstrates, there is a second set of characteristic lines that is related to perturbation induced by the individual turbines. These lines make an angle γ_{lin} with the horizontal. The above definition can be used to calculate the angle, but as shown in Equation 5.9 the inversion Froude number is now replaced with the deep-water inversion Froude number as defined in Equation 5.6.

$$\gamma_{\text{lin}} = \arctan\left(\left(Fr_{i,dw}^2 - 1\right)^{-1/2}\right) \tag{5.9}$$

Figure 5.18 through Figure 5.21 show the characteristic lines determined using the inversion Froude number and deep-water inversion Froude number, plotted over the streamwise background velocity field. The simulations have a turbine spacing of $2D$, $4D$, $8D$, $16D$ respectively, and the farms are equal in length. As previously demonstrated, for small spacings, the wind farm acts as an entity, and the inversion Froude number is the governing parameter. On the contrary, when the turbine spacing is large, the governing parameter is the deep-water inversion Froude number, as the farm behaves as a set of individual turbines. This is clearly visible, as for the farm with a $2D$ turbine spacing the characteristic lines with an angle α_{lin} are dominant, while for a large turbine spacing the characteristic lines with angle γ_{lin} are dominant. In between, both sets of characteristic lines are visible. This further reinforces the idea that for large turbine spacings the deep-water inversion Froude number should be used. Furthermore, since the angles from linear theory match the background velocity field excellently, it is likely the interfacial waves that are dominantly visible.

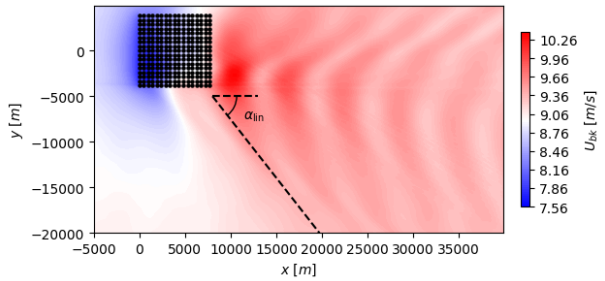

Figure 5.18: Streamwise background velocity field of simulation PDL1MSC, which has a square farm with a power density of $73\,\mathrm{MW\,km^{-2}}$. The locations of the turbines are marked, as well as the characteristic lines of the interfacial waves.

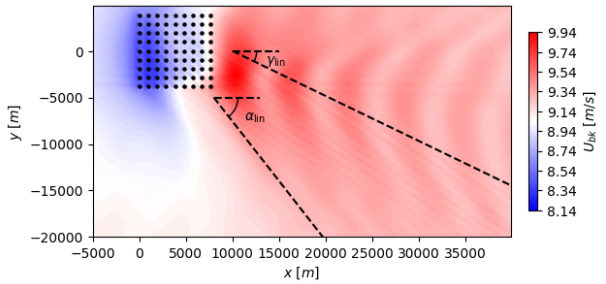

Figure 5.19: Streamwise background velocity field of simulation PDL3MSC, which has a square farm with a power density of $21\,\mathrm{MW\,km^{-2}}$. The locations of the turbines are marked, as well as the characteristic lines of the interfacial waves.

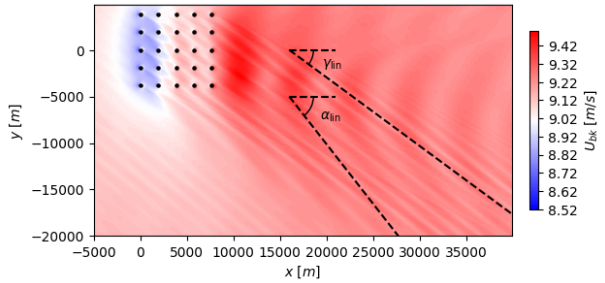

Figure 5.20: Streamwise background velocity field of simulation PDL6MSC, which has a square farm with a power density of $6\,\mathrm{MW\,km^{-2}}$. The locations of the turbines are marked, as well as the characteristic lines of the interfacial waves.

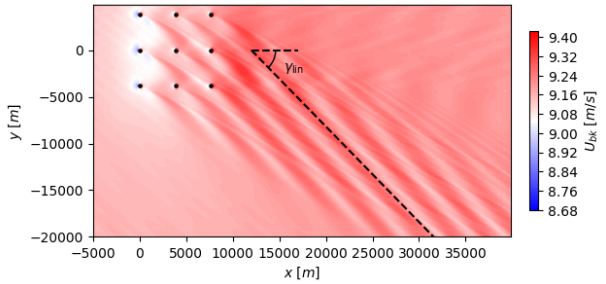

Figure 5.21: Streamwise background velocity field of simulation PDL8MSC, which has a square farm with a power density of $2\,\mathrm{MW\,km^{-2}}$. The locations of the turbines are marked, as well as the characteristic lines of the interfacial waves.

A second argument for the fact that the interfacial waves are dominantly displayed is shown in Figure 5.22. Here, the absolute wavelength that is determined from the wavetrain behind the farm in the streamwise background velocity field is shown versus the Froude number. The Froude number, which governs the behaviour of the internal waves, is varied by changing the length of the farm. Here, the characteristic length scale is the length of the farm, since the turbine spacing is $5D$. If it is indeed the internal waves that would be dominantly visible, it is expected that the wavelength would change with Fr. However, as can be appreciated from Figure 5.22, the wavelength is fairly constant. A constant wavelength is expected for the interfacial wavelength since Fr_i is constant (and Fr_i is the governing parameter at this turbine spacing).

Finally, it can be observed that the expected wavelength of the interfacial wave matches the measured wavelengths of Figure 5.22. Using Equation 5.4 with the geostrophic velocity of $11.48\,\mathrm{m\,s^{-1}}$, the expected wave-

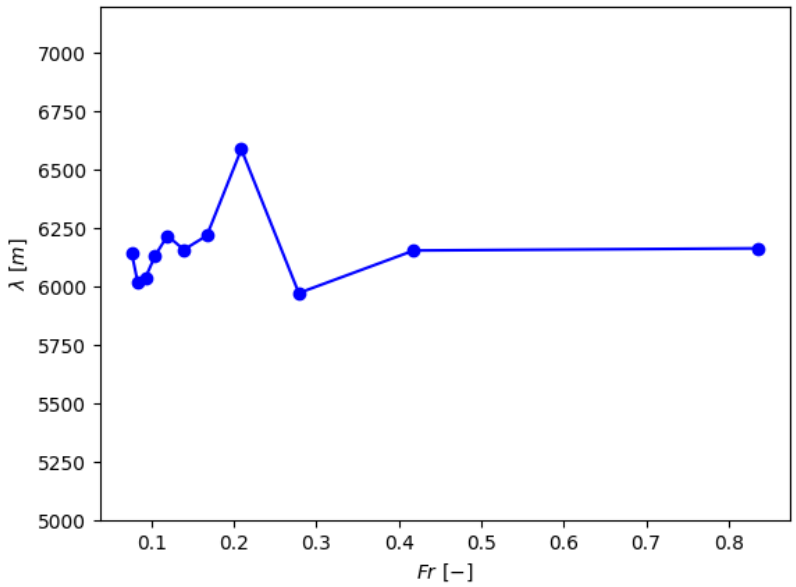

Figure 5.22: Absolute wavelength determined from the streamwise background velocity field versus the Froude number. The Froude number is varied by adding additional rows of turbines to a farm with five turbine columns and a $5D$ turbine spacing.

length from linear theory is $6200\,\mathrm{m}$. Note that the variation in wavelength is attributed to numerical error, as will be further elaborated upon in Subsection 5.2.2.

5.2.2. Interfacial Wavelengths

The above has made it clear that it is the interfacial wavelength that is visible in the streamwise background velocity field. Consequently, it can be analysed whether the interfacial wavelength is affected by any of the wind farm layout parameters discussed in Section 4.4. In the present section, the wavelength is always the wavelength governed by the inversion Froude number, not the wavelength governed by the deep-water inversion Froude number. Every turbine will yield a V-shaped perturbation in the background velocity field. Due to the interaction of these shapes, the wavelength cannot be correctly retrieved. On the contrary, there is only one V-shaped perturbation due to the farm as an entity. The wavelength can be retrieved for this case, since a local maximum will be located at the base of each V. For cases where the deep-water inversion Froude number is governing the background velocity field, the wavelength due to the inversion Froude number can be retrieved by Gaussian smoothing of the background velocity field. Since the perturbation due to the individual turbine is sharper than the perturbation due to the wind farm, the distances between the local maxima will still yield the correct wavelength. Consequently, the wavelength is scaled with the capping inversion height, which is the length scale associated with the inversion Froude number.

Figure 5.23 and Figure 5.24 show the wavelength of the interfacial wave versus the power density, streamwise turbine spacing, and spanwise turbine spacing. By observing the scale on the y-axis, it can be concluded that the variation in wavelength is marginal. The marginal variation is attributed to two things. First of all, it is aimed to remove the perturbations of the individual turbines by Gaussian smoothing. However, if a local maximum of one of these perturbations is close to (and in the order of) a local maximum of the interfacial wavelength that is plotted in the graphs, the maxima might merge due to the smoothing, yielding a different position. Furthermore, since the cell size is $100\,\mathrm{m}$, the wavelength cannot be determined with a finer resolution than this cell size. Both effect are expected to yield discrepancies in the order of (a few) hundred meters. Consequently, if the wavelength shows no clear trend, the non-monotonic behaviour is attributed to numerical error. This is the case for Figure 5.23, Figure 5.24, and therefore the power density and spanwise turbine spacing are deemed to not influence the wavelength of the interfacial wave. The interfacial wavelength seems to be decreasing for increasing streamwise turbine spacing, which is explained as follows. For a larger turbine spacing, the wavelength associated with the deep-water inversion Froude number approaches the wavelength associated with the inversion Froude number (the latter being shown in the graph). Furthermore, for a larger turbine spacing, the deep-water inversion Froude number starts to govern the flow field. As a result, both wavelengths cannot be distinguished anymore, and the script will pick up a slightly smaller 'modulated' wavelength. This effect is,

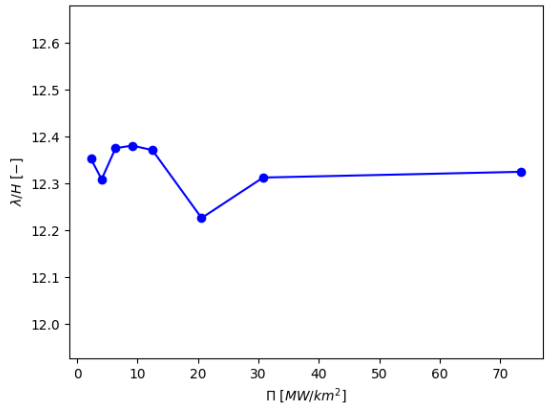

Figure 5.23: Non-dimensional wavelength of the interfacial wave determined from the streamwise background velocity field versus the power density.

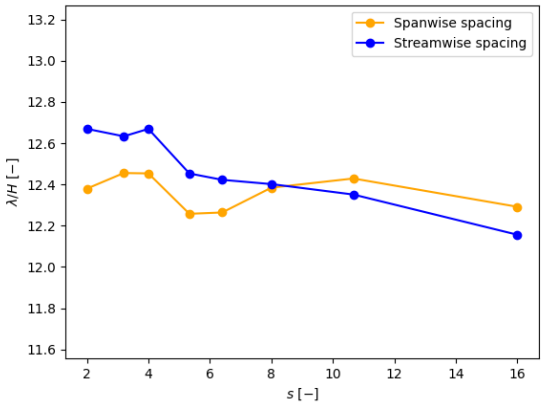

Figure 5.24: Non-dimensional wavelength of the interfacial wave determined from the streamwise background velocity field versus the streamwise and spanwise turbine spacing.

to some extent, also present for smaller spacings, explaining the decrease in wavelength. It is believed that the streamwise turbine spacing does not influence the interfacial wavelength associated with the inversion Froude number.

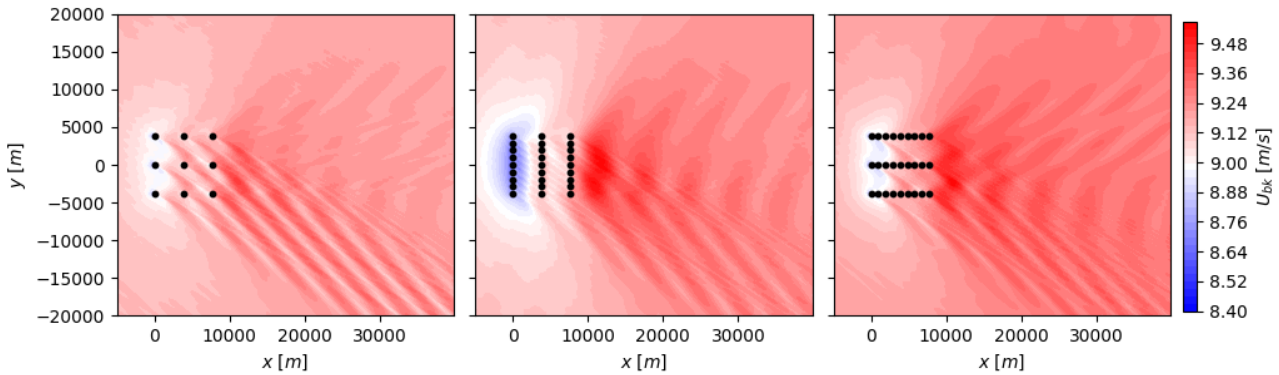

Figure 5.25: Streamwise background velocity fields for simulations that involve large turbine spacings, in, from left to right, both directions, the streamwise direction, and the spanwise direction (simulations PDL8MSC, TSXL8MSC, and TSYL8MSC). On the left the deep-water inversion Froude number is governing, while on the two fields on the right there is no clear governing set of characteristic lines.

Next to determining the wavelength of the interfacial wave, it is interesting to determine whether the inversion Froude number or the deep-water inversion Froude number is the governing non-dimensional number for each of the studied parameters. This can be done by visual inspection of the characteristic lines in the streamwise background velocity field, equal to the analysis of Figure 5.18 through Figure 5.21. As shown in Figure 5.25, the behaviour for the streamwise and spanwise turbine spacing is analogous to that of the power density: the perturbations related to the individual turbines become stronger relative to the perturbations related to the wind farm as an entity for increasing turbine spacings. However, the effect is not as strong as increasing the spacing in both directions at the same time, as is the case for the power density. Rather, both types of perturbations appear equally strong. Thus, it is not the streamwise spacing, but rather the equivalent turbine spacing that is important in the deep-water length scale. Indeed, for simulations TSXL8MSC and TSYL8MSC the equivalent turbine spacing is $8D$, equal to the (effective) turbine spacings in Figure 5.11 and Figure 5.15, which appeared to be the cross-over point in the previous analysis.

Figure 5.26 and Figure 5.27 show the non-dimensional wavelength versus the aspect ratio and the non-dimensional horizontal staggering angle, as defined in Subsection 4.4.1. For both cases, the discrepancies are again attributed to numerical error, concluding that the aspect ratio of the farm and the staggering angle do not influence the interfacial wavelength. Furthermore, for changing aspect ratio, the inversion Froude number still governs the flow, given that the the turbine spacing and farm length are such that the assumptions of shallow-water theory are valid. For an increasing staggering angle, the deep-water inversion Froude number starts governing the flow. It is assumed that the effective streamwise spacing is doubled due to the turbine

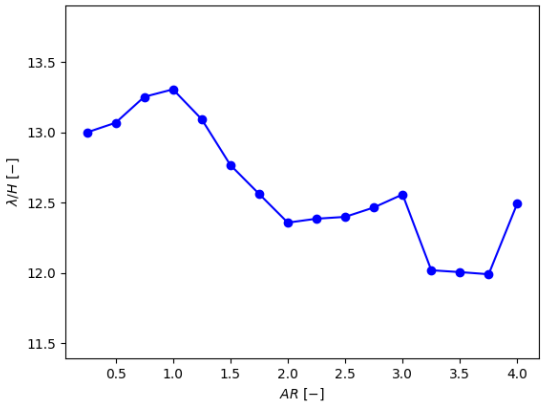

Figure 5.26: Non-dimensional wavelength of the interfacial wave determined from the streamwise background velocity field versus the aspect ratio.

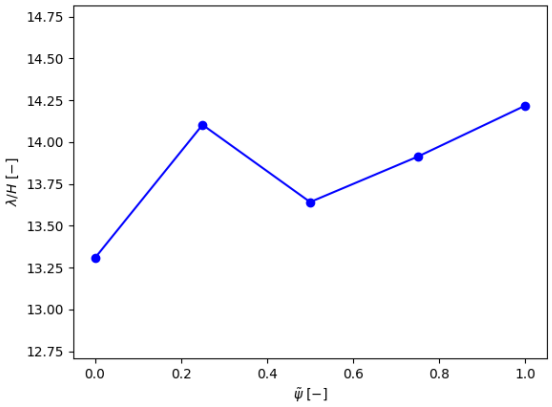

Figure 5.27: Non-dimensional wavelength of the interfacial wave determined from the streamwise background velocity field versus the non-dimensional horizontal staggering angle.

rows not being aligned, and consequently, the perturbation by the individual turbines is stronger relative to the overall perturbation.

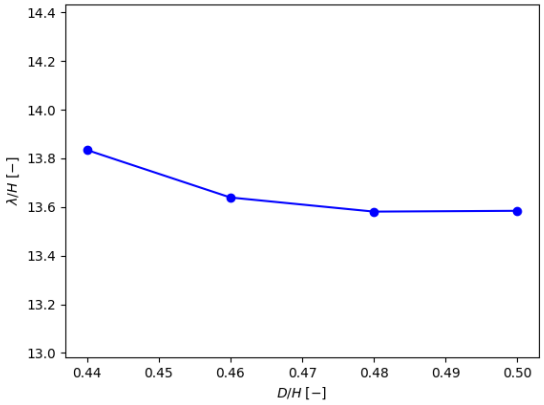

Figure 5.28: Non-dimensional wavelength of the interfacial wave determined from the streamwise background velocity field versus the non-dimensional rotor diameter.

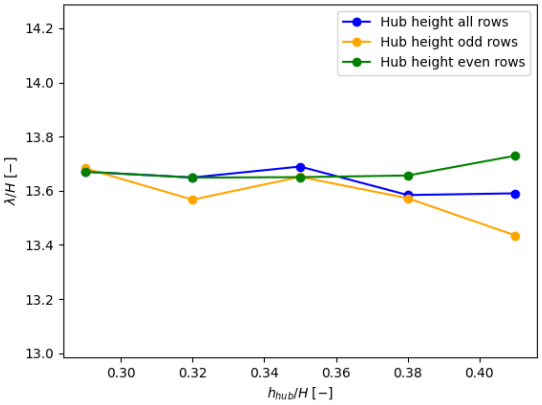

Figure 5.29: Non-dimensional wavelength of the interfacial wave determined from the streamwise background velocity field versus the non-dimensional hub height of all rows, even rows, and odd rows, of which the latter two represent a vertically staggered farm. It must be kept in mind that the two data points on the right are cases for which the hub height limit is exceeded. Although the magnitude of perturbations is still acceptable, care must be taken to include these data points in the analysis.

Figure 5.28 and Figure 5.29 again show the wavelength of the interfacial wave, but this time versus the non-dimensional rotor diameter, and the hub height of either all turbine rows, even turbine rows, or odd turbine rows. The latter two cases correspond to a vertically staggered farm. Even though the wavelength is monotonically decreasing with increasing rotor diameter, no conclusions can be drawn since the difference is less than the cell size of the simulations. The same is true for increasing the hub height in either of the three cases displayed in Figure 5.29. Moreover, as discussed in Subsection 4.5.3, there is an advised limit on the hub height with respect to the capping inversion height. This limit is exceeded for the two data points on the right. However, the velocity and pressure perturbations are such that the assumptions of the linear model are not violated, but still care must be taken to include these data points in any conclusion. For both Figure 5.28 and Figure 5.29, the inversion Froude number governs the flow for all data points. The perturbations due to the individual turbines are clearly visible in the background velocity field, but it is assumed that this is due to the shorter farm length of $4800\,\mathrm{m}$, smaller than the assumed forcing length in the shallow-water theory of $4\pi H$ as discussed in Lanzilao and Meyers, 2024.

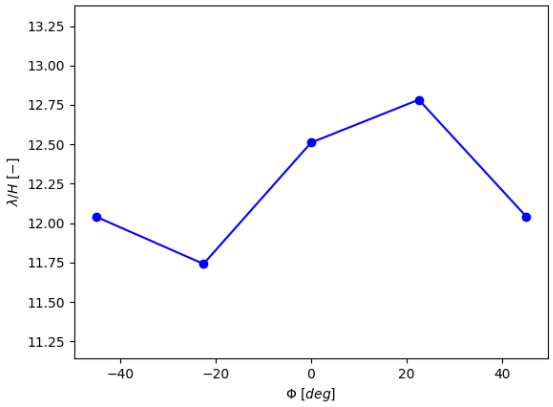

Figure 5.30: Non-dimensional wavelength of the interfacial wave determined from the streamwise background velocity field versus the orientation of a square farm with respect to the freestream.

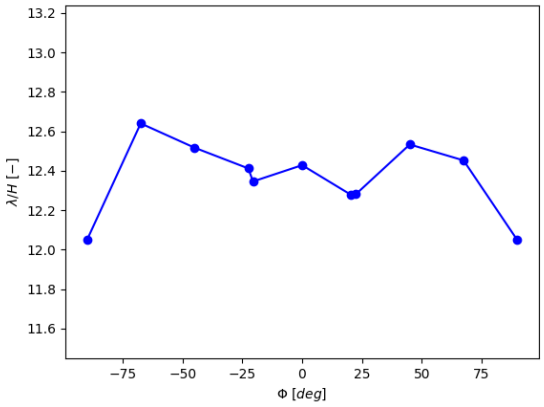

Figure 5.31: Non-dimensional wavelength of the interfacial wave determined from the streamwise background velocity field versus the orientation of a rectangular farm with respect to the freestream.

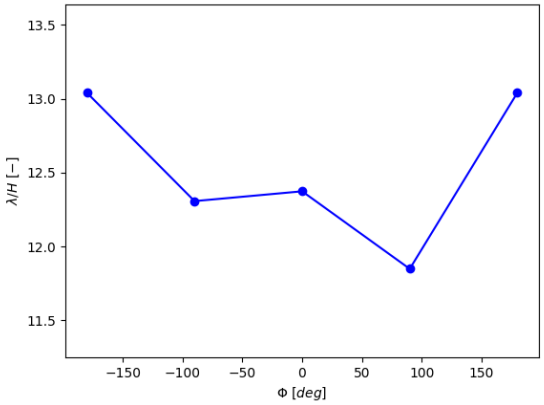

Figure 5.32: Non-dimensional wavelength of the interfacial wave determined from the streamwise background velocity field versus the orientation of a triangular farm with respect to the freestream.

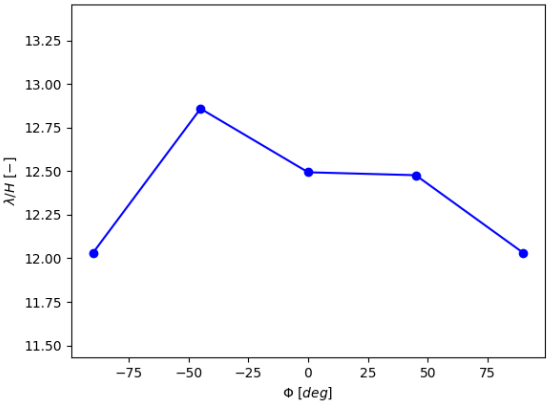

Figure 5.33: Non-dimensional wavelength of the interfacial wave determined from the streamwise background velocity field versus the orientation of an elliptic farm with respect to the freestream.

Finally, Figure 5.30 through Figure 5.33 show the wavelength of the interfacial wave versus a square, rectangular, triangular, or elliptic farm respectively, versus the orientation of the farm with respect to the direction of the freestream. Once more, the deviation of the wavelength with respect to the mean for all directions is small and is attributed to the aforementioned reasons related to numerical error. Whether the deep-water inversion Froude number or the inversion Froude number governs the flow is highly dependent on the orientation of the farm. This indicates that the effective streamwise and spanwise turbine spacings with respect to the freestream must be considered. For example, when a square farm is rotated, the distance until the first turbine downstream of a certain turbine increases, and decreases again until the row or column is aligned with the freestream again. The circular wind farm only has one relevant orientation, and the consequent non-dimensional wavelength is 12. This is in line with the other shapes. Furthermore, the flow for a circular wind farm seems to be governed by the inversion Froude number.

5.3. Wind Farm Performance

Now that the atmospheric gravity wave excitation is discussed, it is time to study the feedback of the excited waves on the wind farm performance. To study the wind farm performance from a gravity wave perspective, wind farm performance will be quantified principally using the non-local farm efficiency defined by Allaerts and Meyers, 2018, shown below in Equation 5.10.

$$\eta_{nl} = \frac{P_1}{P_{th}} \tag{5.10}$$

Here, P_1 is the average power of a first-row turbine. Furthermore, P_{th} is the theoretical turbine power, calculated by Equation 5.11. Note that for some farms the first row of turbines is not clearly defined. In this case, the first row turbines are those that are at most $50\,\mathrm{m}$ downstream of the most upstream turbine.

$$P_{th} = \frac{1}{2} C_p U_{ref}^3 \frac{\pi}{4} D^2 \tag{5.11}$$

The non-local efficiency aims to quantify the loss of wind farm performance caused by the gravity wave-induced pressure gradients throughout the farm. Furthermore, the wake efficiency, albeit a parameter not fully related to gravity wave losses, is of interest since the product of the wake and non-local efficiency is the total farm efficiency. The latter will give a clear image of the performance of the wind farm all factors included. The wake efficiency is defined by Equation 5.12, as shown in Allaerts and Meyers, 2018, where P_{total} is the total farm power output.

$$\eta_w = \frac{P_{\text{total}}}{N_t P_1} \tag{5.12}$$

As many of the literature discusses (e.g. Lanzilao and Meyers, 2022b, M. Khan et al., 2024, or Stipa, Ajay, et al., 2024b), atmospheric gravity waves induce an adverse pressure gradient at the beginning of the wind farm, and a favourable pressure gradient at the end of the wind farm. The adverse pressure gradient causes a global blockage effect, reducing the power of the first-row turbines (Lanzilao and Meyers, 2022b). Therefore, the non-local efficiency is a measure of the pressure feedback of the AGWs on wind farm performance. Moreover, since the inversion Froude number is supercritical, interfacial waves can only travel downstream, and the global blockage effect is only caused by the internal waves (Stipa, Ajay, et al., 2024b). Then, Lanzilao and Meyers, 2022b notes that the favourable pressure gradient at the downstream end of the wind farm can enhance wake recovery, such that also the wake efficiency is, to some extent, a measure for the feedback on wind farm performance as a result of AGW excitation. Finally, the total farm efficiency is the product of the wake efficiency and the non-local efficiency, as shown in Equation 5.13.

$$\eta_f = \eta_w \eta_{nl} \tag{5.13}$$

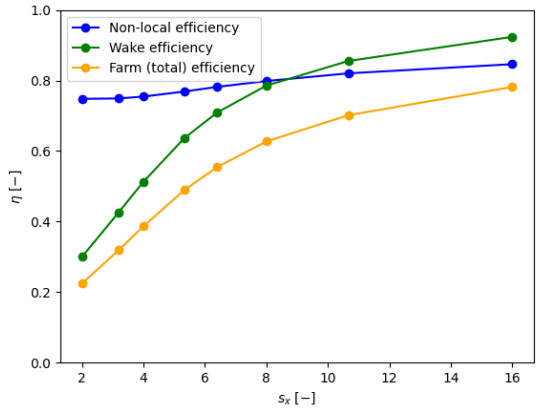

Figure 5.34: Non-local, wake, and total farm efficiency versus the streamwise turbine spacing. The spanwise turbine spacing is $4D$.

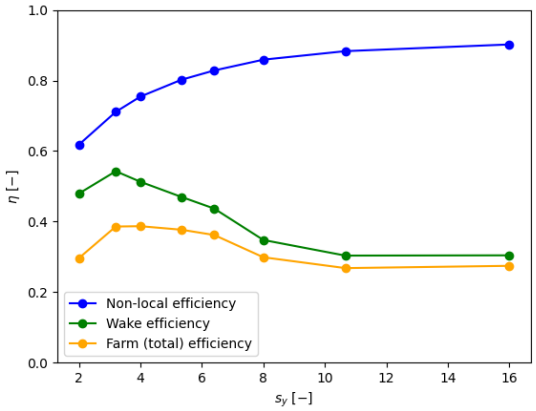

Figure 5.35: Non-local, wake, and total farm efficiency versus the spanwise turbine spacing. The streamwise turbine spacing in $4D$.

In Figure 5.34 and Figure 5.35, the above-defined efficiencies are plotted versus the streamwise and spanwise turbine spacing respectively. It can be observed that the non-local efficiency increases with increasing turbine spacing. The blockage effect induced by the internal waves will be weaker due to the smaller perturbation that is due to the turbines being spaced further apart. Consequently, the first-row power generation and resulting non-local efficiency is higher for larger turbine spacings. Interestingly, the effect of the spanwise turbine spacing is significantly larger than the effect of the streamwise turbine spacing. It is thus suggested that the spanwise turbine spacing is more critical in the determination of the non-local efficiency. The pressure perturbation is significantly higher for small spanwise turbine spacing than small streamwise spacing, and hence the effect of more first-row turbines due to a smaller spanwise turbine spacing is assumed to contribute more to the blockage effect than the turbine rows being closer to each other. Rather, as visible in Figure 5.34, the wake efficiency is significantly increased with increasing streamwise turbine spacing, as the wake has more

time to recover before impacting on the next downstream turbine. Regarding the spanwise turbine spacing, an optimum in the wake efficiency is visible. The fact that there is an optimum is an indication that the wake efficiency is a compromise between the negative effect of a smaller spanwise spacing (since a small spanwise spacing gives less space for the wake to recover by expanding), and the positive effect of a smaller spanwise spacing (since a small spanwise spacing will likely yield stronger internal waves that enhance the wake recovery at the downstream end of the farm).

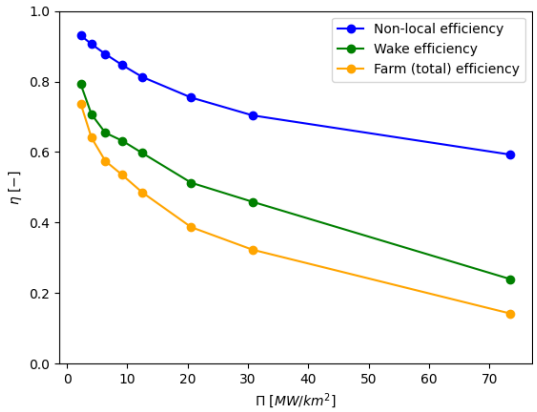

Figure 5.36: Non-local, wake, and total farm efficiency versus the power density.

Figure 5.36 shows the efficiencies versus the power density. The power density is varied by increasing the streamwise and spanwise turbine spacings at the same time, and at an equal rate. Indeed, it is clearly visible that the non-local, wake, and total farm efficiency trends are a superposition of the trends observed in Figure 5.34 and Figure 5.35. The non-local, wake, and thus total farm efficiency approach one for a very low power density, as the turbines are spaced so far apart that the perturbations have damped out and the freestream properties of the flow are restored.

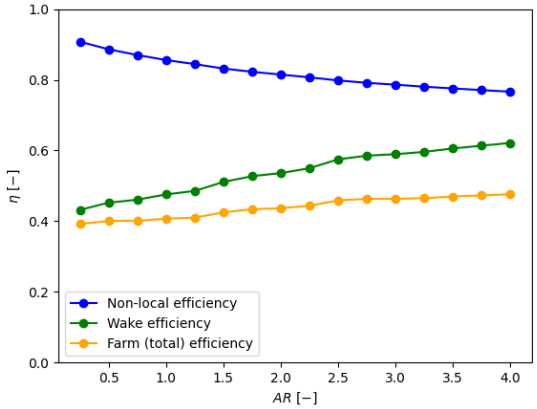

Figure 5.37: Non-local, wake, and total farm efficiency versus the aspect ratio.

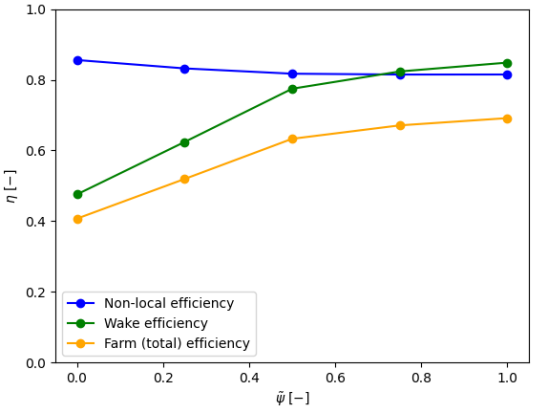

Figure 5.38: Non-local, wake, and total farm efficiency versus the non-dimensional horizontal staggering angle.

The next parameters that are discussed are the aspect ratio and the (non-dimensional) horizontal staggering angle, in Figure 5.37 and Figure 5.38 respectively. The aspect ratio is varied by only increasing the width of the farm. As Allaerts and Meyers, 2019 reports, the power loss increases with the width of the farm (and only approaches an asymptote when the width is two orders of magnitude larger than the capping inversion height). Equivalently, the non-local efficiency decreases with farm width, which is visible in Figure 5.37. In Allaerts and Meyers, 2019, the power loss reaches a maximum for a certain aspect ratio and drops off on both sides of the maximum. This is due to the fact that Allaerts and Meyers, 2019 considers a constant number of turbines. Then, a very wide but short farm (which only perturbs the flow slightly), and a very long but narrow farm (which the flow can go around easily), do not have high power losses. Since the length of the farm is not

changed in the present case, it is expected that it is actually the width that governs the behaviour shown in Figure 5.37. As a consequence of the stronger internal waves, the wake efficiency is believed to increase due to enhanced wake recovery as a result of the favourable pressure gradient. The non-local efficiency shows a slight decrease with the non-dimensional horizontal staggering angle. It is suggested that this is caused by the marginally increased width due to the staggered turbine rows. As mentioned above, an increased width is associated with a smaller non-local efficiency. The wake efficiency increases as expected, since the staggering of the turbine rows gives more space to the turbine wakes to recover.

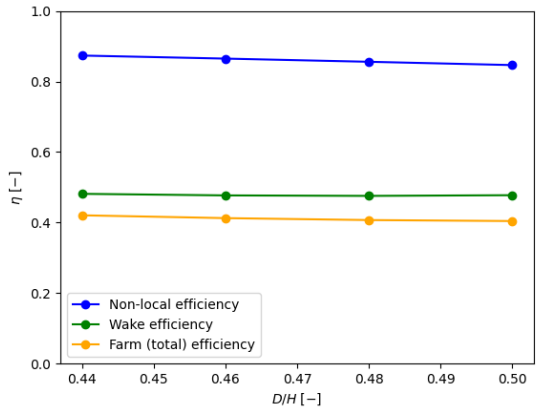

Figure 5.39: Non-local, wake, and total farm efficiency versus the non-dimensional rotor diameter.

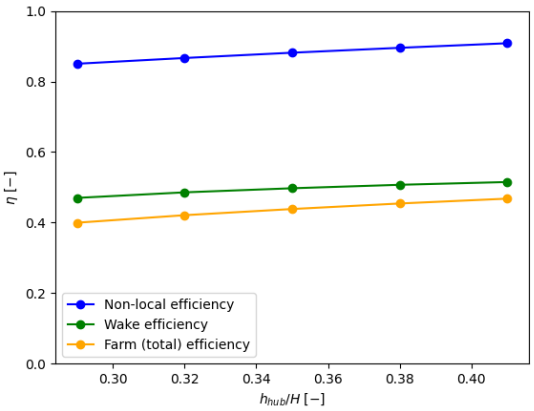

Figure 5.40: Non-local, wake, and total farm efficiency versus the hub height. It must be kept in mind that the two data points on the right are cases for which the hub height limit is exceeded. Although the magnitude of perturbations is still acceptable, care must be taken to include these data points in the analysis.

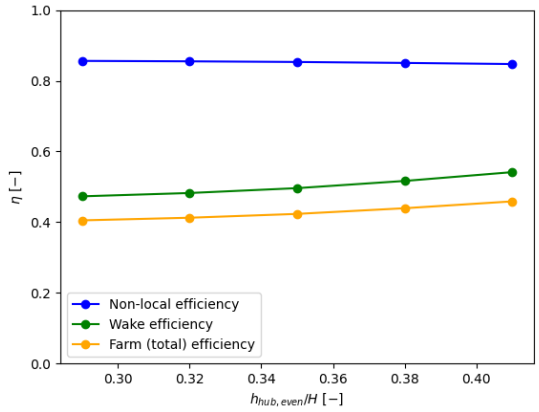

Figure 5.41: Non-local, wake, and total farm efficiency versus the hub height of the even turbine rows in a vertically staggered farm. It must be kept in mind that the two data points on the right are cases for which the hub height limit is exceeded. Although the magnitude of perturbations is still acceptable, care must be taken to include these data points in the analysis.

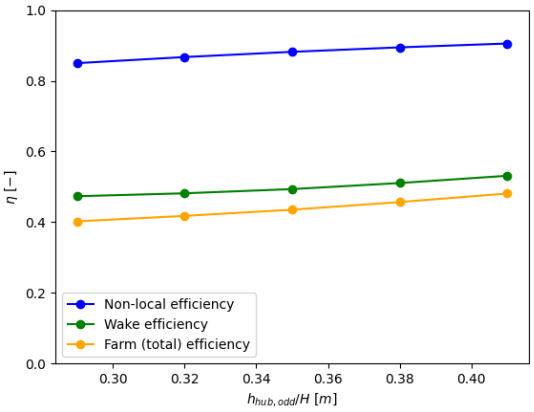

Figure 5.42: Non-local, wake, and total farm efficiency versus the hub height of the odd turbine rows in a vertically staggered farm. It must be kept in mind that the two data points on the right are cases for which the hub height limit is exceeded. Although the magnitude of perturbations is still acceptable, care must be taken to include these data points in the analysis.

Then, the rotor diameter and hub height of the turbines in a five-by-five wind farm are varied in Figure 5.39 and Figure 5.40, while the effect of the hub height of the even and odd turbine rows of a vertically staggered farm are shown in Figure 5.41 and Figure 5.42 respectively. First of all, the non-local efficiency marginally decreases with increasing rotor diameter. The non-dimensionalisation of the rotor diameter with the capping inversion height shows that a larger diameter occupies a larger ratio of the boundary layer height. As a result, the blockage effect is higher due to stronger internal waves. The wake efficiency is not altered by an increasing rotor diameter. The larger rotor diameter is associated with a larger energy extraction. As a consequence of the larger diameter, the wake is wider and the velocity deficit is larger resulting in a lower wake efficiency. On the contrary, since the rotor occupies a larger portion of the ABL, the velocity surrounding the wake is higher because of increased flow acceleration around the rotor to maintain mass and momentum conserva-

tion, enhancing wake recovery. The wake recovery is then further enhanced as a result of the slightly stronger favourable pressure gradient. The effects seem to be balanced, as the wake efficiency is practically constant. For cases where the hub height is increased, a smaller non-local efficiency would be expected since a stronger perturbation would be associated with the turbine being closer to the capping inversion. However, due to the velocity profile in the ABL, a higher turbine would experience an incoming flow with a higher velocity, increasing the first-row power output and consequently the non-local efficiency. This effect is only present when the first row of turbines is elevated, as is the case for Figure 5.40 and Figure 5.42. In Figure 5.41 the non-local efficiency indeed decreases, albeit marginally. Whenever the hub height is increased, the wake efficiency also increases, as the higher velocity enhances wake recovery. Additionally, for a vertically staggered farm, only part of the wake of a turbine impacts on the downstream turbine, further increasing wake efficiency.

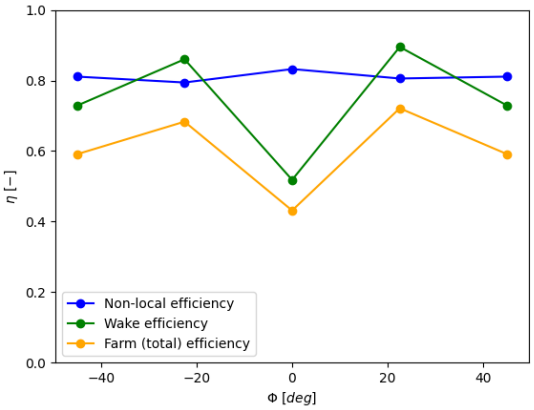

Figure 5.43: Non-local, wake, and total farm efficiency versus the orientation of a square farm with respect to the freestream.

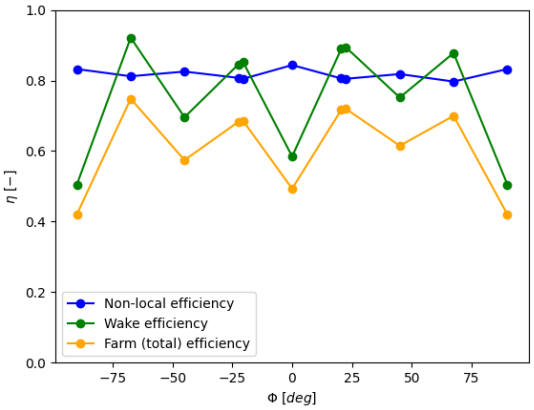

Figure 5.44: Non-local, wake, and total farm efficiency versus the orientation of a rectangular farm with respect to the freestream.

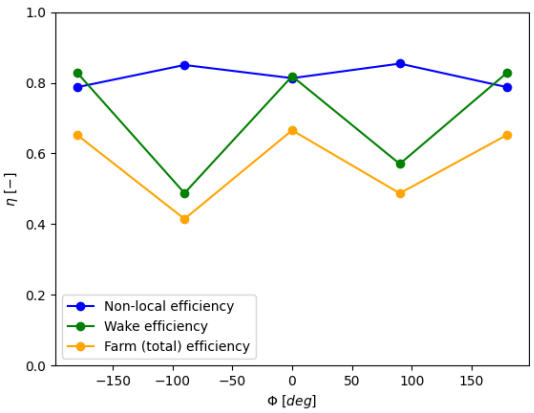

Figure 5.45: Non-local, wake, and total farm efficiency versus the orientation of a triangular farm with respect to the freestream.

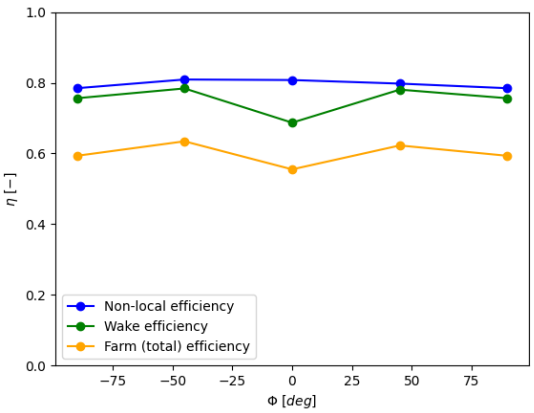

Figure 5.46: Non-local, wake, and total farm efficiency versus the orientation of an elliptic farm with respect to the freestream.

Finally, Figure 5.43 through Figure 5.46 show the efficiencies versus the orientation of a square, rectangular, triangular, and elliptic farm respectively. The behaviour of the efficiencies can be explained using the trends observed in Figure 5.34 and Figure 5.35. From Figure 5.43 through Figure 5.46, it can be concluded that the wake efficiency has a (local) maximum when the turbines in the farm are aligned, which is expected since in that case the effective turbine spacing is minimum and the wake has the shortest distance to recover. Furthermore, when the wake efficiency is at a local maximum, the non-local efficiency is at a local minimum. After all, as was already concluded from Figure 5.34 and Figure 5.35, the internal waves are stronger for smaller turbine spacings, and the non-local efficiency is smaller. Indeed, this thought can be extended to the effective turbine spacings of rotated farms. Again, the circular farm has only one relevant orientation, and therefore no trends can be observed. However, similar efficiencies as the elliptic farm are observed, with the non-local, wake, and total efficiencies being 0.81, 0.78, and 0.63 respectively.

5.4. Developer's Perspective

In the previous sections, all farms considered had a constant farm length, allowing for a proper OFAT discussion of the results. In real life, it might be more realistic that a developer has to adhere to a certain budget, that allows for a certain number of turbines. Therefore, in this section results are displayed for the previously studied parameters, varying them using a constant number of turbines rather than a constant farm length. Since for most parameters both the farm length and number of turbines was constant, only the streamwise turbine spacing, spanwise turbine spacing, power density, and aspect ratio are discussed. Furthermore, the reference layouts by Kainz et al., 2024 are evaluated. Note that a constant farm length could represent a certain area that is allocated to a project, and therefore the above results are deemed useful also in practical scenarios. Finally, the present section will reason from an efficiency perspective, and consequently the highest efficiency is deemed to be the 'best' scenario for wind farm design. Of course, there is a trade-off between the efficiency of the wind farm, the wind farm area, and the number of turbines. A developer can opt for a lower wind farm efficiency if that means more turbines can be installed on a certain location. This is out of the scope of the present study, due to the large parameter space including, for example, turbine power or turbine type, turbine cost, land cost, etc.

Figure 5.47 and Figure 5.48 show the non-local, wake and total farm efficiency versus the streamwise and spanwise turbine spacing respectively. It can be observed that the variation in non-local efficiency is significantly less than for a constant farm length. This effect is attributed to the fact that when varying the turbine spacing for a constant number of turbines, the length or width of the farm is also increased. As shown in Allaerts and Meyers, 2019, increasing farm size is associated with increasing power losses. This effect counters the positive effect a larger turbine spacing has on the blockage effect, as shown in Figure 5.34 and Figure 5.35. Consequently, the slope of the increase in non-local efficiency is significantly smaller for Figure 5.48, and even diminishes in Figure 5.47. As expected, the wake efficiency increases with increased streamwise turbine spacing, as the wake is given more time to recover. The spanwise turbine spacing only improves wake recovery up until a certain point, as seen in Figure 5.35, which has an optimal wake efficiency. Figure 5.48 is deemed to be to the right of this optimum, and thus only the effect of decreased wake recovery with increased spanwise turbine spacing due to weaker internal waves is observed.

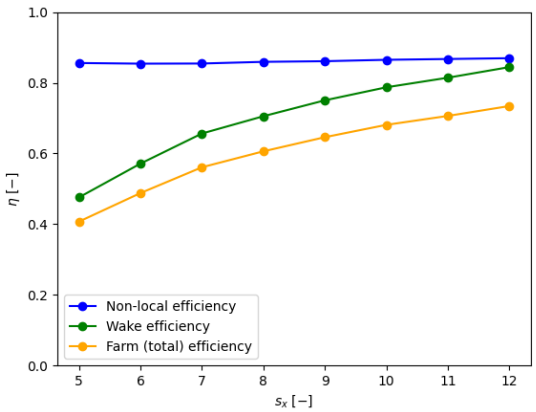

Figure 5.47: Non-local, wake, and total farm efficiency versus the streamwise turbine spacing for a farm with a constant number of turbines. The spanwise turbine spacing is $5D$.

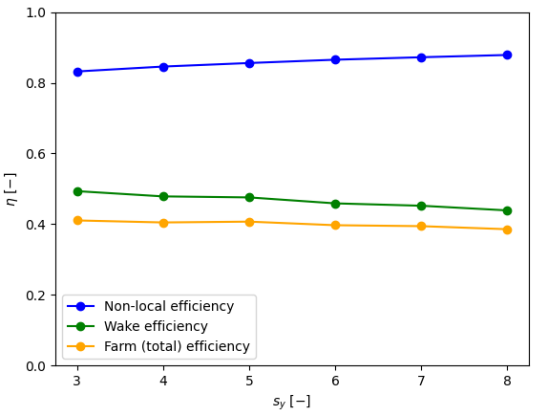

Figure 5.48: Non-local, wake, and total farm efficiency versus the spanwise turbine spacing for a farm with a constant number of turbines. The streamwise turbine spacing is $5D$.

As can be appreciated from Figure 5.49, the trends in the non-local, wake, and total farm efficiency versus the power density are once more the superposition of the trends observed in Figure 5.47 and Figure 5.48. The qualitative behaviour of the efficiencies in comparison to a constant farm length in Figure 5.36 does not change, since the efficiencies still approach unity when the power density approaches zero. Note that the power density has a smaller range, and thus the effect seems less pronounced than in Figure 5.36.

In Figure 5.50, the efficiencies are plotted versus the aspect ratio. Note that the farm length is not a constant anymore, and thus a low aspect ratio means a narrow and long farm, while a high aspect ratio means a wide and short farm, consistent with Allaerts and Meyers, 2019. To clearly show the behaviour of the non-local efficiency, it is shown on an enlarged y-scale in Figure 5.51. Contrary to Figure 5.37, there is now a minimum value of the non-local efficiency, consistent with Allaerts and Meyers, 2019. The aspect ratio corresponding

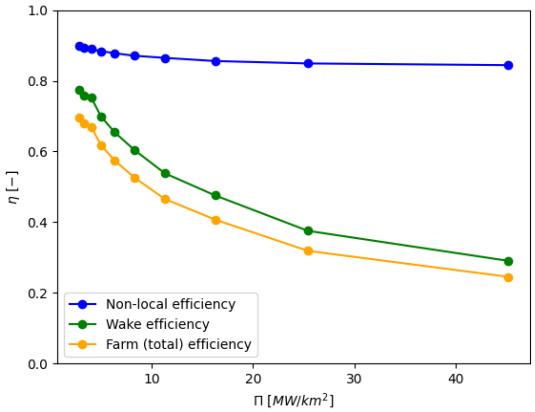

Figure 5.49: Non-local, wake, and total farm efficiency versus the power density for a farm with a constant number of turbines.

with maximum power losses due to gravity waves is reported to be 1.5 by Allaerts and Meyers, 2019. This value is close to the location of the minimum in Figure 5.51. For low aspect ratios, the length of the farm is so short that the blockage effect is small, while for high aspect ratios, the flow can go easily around the farm, which explains the minimum of the non-local efficiency as explained in Allaerts and Meyers, 2019. The wake efficiency increases when the aspect ratio increases, as the number of turbine rows decreases. For long farms, the enhanced wake recovery at the downstream end of the farm seems to improve the wake efficiency at first, but the superposition of many wakes in very long farms is eventually the dominant effect, rapidly decreasing the wake efficiency. This behaviour is again consistent with Allaerts and Meyers, 2019.

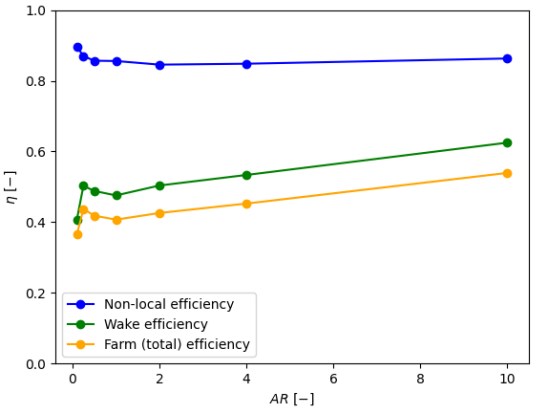

Figure 5.50: Non-local, wake, and total farm efficiency versus the aspect ratio for a farm with a constant number of turbines.

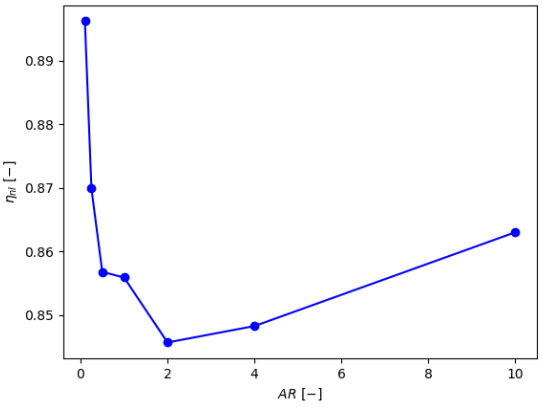

Figure 5.51: Non-local efficiency versus the aspect ratio for a farm with a constant number of turbines with an enlarged y-scale.

Table 5.1 shows the results for the reference layouts considered in Kainz et al., 2024. For a certain plot of land and a certain number of turbines, two layout are considered. In FLNU1MSC, the turbines are uniformly distributed over the land, with an average turbine spacing of $7D$. In FLNU2MSC, the turbines are concentrated on the boundaries of the wind farm. Here, the turbines on the boundaries are spaced at a distance of $2D$ from each other. Firstly, it can be noted that for the highly irregular wind farm shape and turbine placement, the wavelength of the interfacial wave related to the inversion Froude number is still in the order of the predicted value from linear theory. Then, even though the blockage effect is higher for FLNU2MSC, which has many more first-row turbines, the non-local efficiency is slightly higher. It is hypothesized that this is due to the favourable pressure gradient that acts on the many turbines on the downstream boundary of the wind farm. The wake efficiency is slightly lower, since in FLNU1MSC the rows of turbines are staggered, while in FLNU2MSC the dense first row acts as a 'wall' for downstream turbines. As can be deduced from the total farm efficiency, the two effects seem to be balanced.

Table 5.1: Wavelength of the interfacial wave related to the inversion Froude number and non-local, wake, and total farm efficiency for the reference farm layouts presented in Kainz et al., 2024.

Identifier	Wavelength λ	Non-Local Efficiency η_{nl}	Wake Efficiency η_w	Farm Efficiency η_f
FLNU1MSC	$5700\,\mathrm{m}$	0.780	0.991	0.773
FLNU2MSC	$6000\,\mathrm{m}$	0.793	0.974	0.773

5.5. Comparison and Validation

The present section will study the effect of certain choices made in this study, such as the inclusion of the Coriolis effect and the usage of the Nieuwstadt model, and validate the numerical setup of the LES simulations, as well as the results of the MSC model. To validate the MSC results, the LES results are assumed to be the ground truth, such that validation can be performed rather than verification.

5.5.1. Influence of the Coriolis Effect

To investigate what the effect is of a different Coriolis parameter, the simulations using the MSC model involved with a varying power density are rerun for $f_c = 0\,\mathrm{s}^{-1}$. This corresponds to a farm located at the equator, where the Coriolis effect is absent. In Figure 5.52 the wavelength of the interfacial wave that is associated with the inversion Froude number versus the power density is plotted for the two scenarios. First of all, it can be concluded that the qualitative behaviour of the wavelength is similar, in either case, the wavelength is constant with power density. However, the absolute value of the wavelength is significantly higher. This can be attributed to the higher geostrophic velocity when $f_c = 0\,\mathrm{s}^{-1}$ (although the name geostrophic velocity is incorrect when the geostrophic balance breaks down at the equator). The geostrophic velocity, which in this case is only a result of the pressure gradient, is determined to be $14.1\,\mathrm{m\,s}^{-1}$ using the MSC model. When Equation 5.4 is used to calculate the expected wavelength using this new velocity, $7700\,\mathrm{m}$ is obtained, and a close match with Figure 5.52 is observed, since non-dimensionalisation of the above value yields 15.4. In conclusion, the Coriolis effect does not change the qualitative behaviour. Note that this conclusion cannot be readily extrapolated to higher Coriolis parameters. For example, at high Coriolis parameters, the geostrophic velocity might be low enough such that the inversion Froude number changes from super- to subcritical.

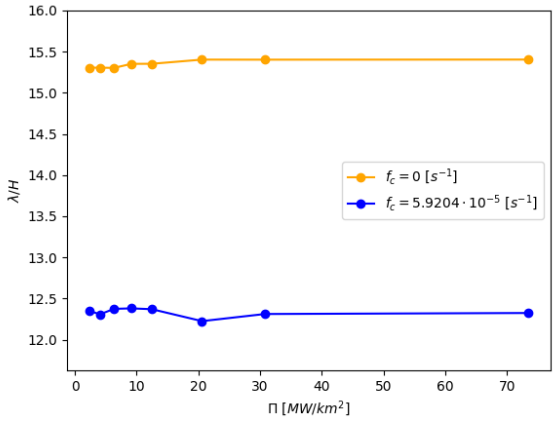

Figure 5.52: Non-dimensional wavelength of the interfacial wave determined from the streamwise background velocity field versus the power density for cases where the Coriolis effect is either absent or present.

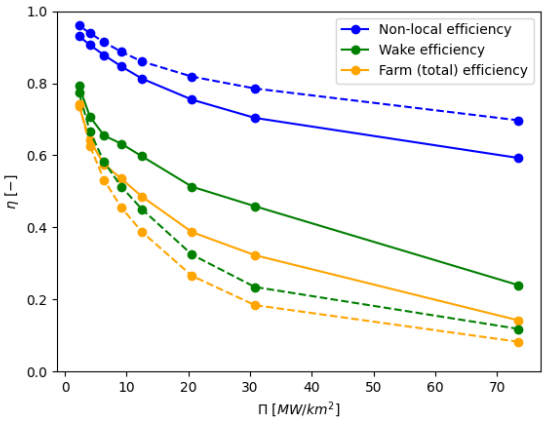

Figure 5.53: Non-local, wake, and total farm efficiency versus the power density for cases where the Coriolis effect is either absent (dashed lines) or present (solid lines).

Figure 5.53 shows the non-local, wake, and total farm efficiency versus the power density in case the Coriolis effect is present (solid lines), and absent (dashed lines). Firstly, the non-local efficiency is larger when the Coriolis effect is excluded. This is because the turning of the flow due to the Coriolis effect causes the flow to 'see' a larger effective farm width. As demonstrated by Allaerts and Meyers, 2019, a larger wind farm width is associated with higher power losses. On the contrary, the turning of the flow causes the wake efficiency to increase. Since the wake is advected by the flow, the direction of the wake will also change, causing only part of it to impact on the downstream turbine, thus increasing the wake efficiency. Both effects are larger for high power densities, where the turbines are close to each other and the above effects play a larger role. Indeed, when the turbines are very far apart, the dashed and solid lines approach each other. In conclusion, when the results of the present study are used for wind farms closer to the equator, the non-local efficiency is

underestimated, and the wake efficiency is overestimated. Since the latter is the stronger effect, the total farm efficiency is overestimated. For farms located north of the latitude used in the present study, the reverse is not necessarily true, since the behaviour of the interfacial waves might be changed due to the lower geostrophic velocity.

5.5.2. Influence of the Inflow Data for the MSC Model

As mentioned in Subsection 4.2.1, the Nieuwstadt, 1983 model is used in the present study as precursor data might not be readily available in real-life scenarios. Therefore, the current section elaborates upon the differences in the MSC results when using the Nieuwstadt model versus using the (processed) precursor data.

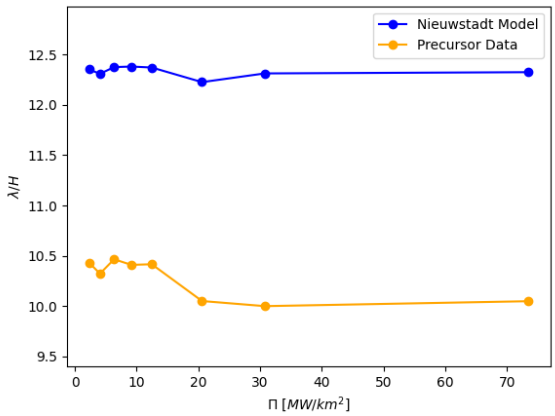

Figure 5.54: Non-dimensional wavelength of the interfacial wave determined from the streamwise background velocity field versus the power density for cases where the Nieuwstadt model and the precursor data is used.

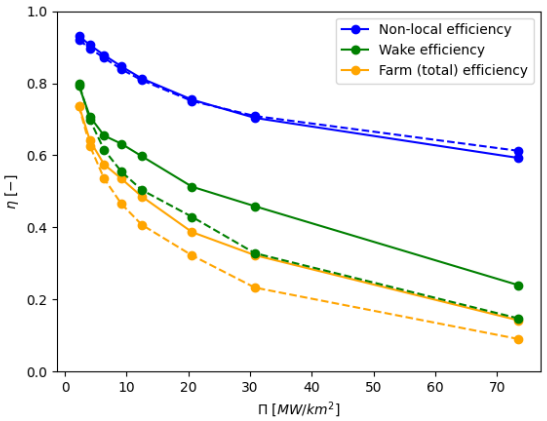

Figure 5.55: Non-local, wake, and total farm efficiency versus the power density for cases where the Nieuwstadt model is used (solid lines) or the precursor data (dashed lines).

In Figure 5.54 the wavelength of the interfacial wave associated with the inversion Froude number is shown. Again, the qualitative behaviour of the wavelength versus the power density is the same for both cases. However, the magnitude of the wavelengths differ. This is once more caused by the difference in geostrophic velocity. The expected wavelength from linear theory corresponding to the geostrophic velocity of $9.31\,\mathrm{m\,s^{-1}}$ in the precursor data is $4700\,\mathrm{m}$ (for which the non-dimensional wavelength is 9.4). This value indeed is in the vicinity of the values observed in Figure 5.54. Next, Figure 5.55 shows the non-local, wake, and farm efficiency versus the power density for the cases where the Nieuwstadt model is used (solid lines) and where the precursor data is used (dashed lines). Firstly, there is an excellent match between the non-local efficiencies of both cases. Therefore, both the Nieuwstadt model and precursor simulation are suitable to quantify the global blockage effect and the associated non-local efficiency. The wake efficiency is larger when the Nieuwstadt model is used. This is due to the fact that the velocity in the boundary layer above the hub height is higher when the Nieuwstadt model is used, as can be appreciated from Figure 4.1, consequently enhancing wake recovery. In conclusion, the Nieuwstadt model adequately describes the gravity wave effects, but an overestimation of the wake efficiency and thus the farm efficiency must be kept in mind.

5.5.3. Validation of LES Domain Setup

In the design of the domain for the Largy Eddy Simulations, some wave characteristics need to be determined a priori, for example for the sizing of the damping layers. The present section will validate the assumptions made in the domain design.

First of all, the top Rayleigh Damping Layer is sized with the maximum vertical wavelength, which was determined to be $5250\,\mathrm{m}$. However, the maximum observed value is $5475\,\mathrm{m}$. It can be checked whether the damping of the RDL is still suitable. As mentioned by Stipa, Ahmed Khan, et al., 2024, reflections occur when the damping is too strong or too weak. If the damping is too strong, the RDL would act as a physical boundary. In this case, a discrete jump in the variable fields would be observed, which is not the case. If the damping is too weak, the AGWs are not damped before the end of the domain. As can be appreciated from Figure 5.56, where the vertical velocity is plotted with height for different streamwise locations, the waves are properly damped before they reach the top of the domain. Therefore, the damping of the RDL is adequate.

Then, the buffer zone of the advection damping layer is sized using the trapped gravity wave (TGW) wave-

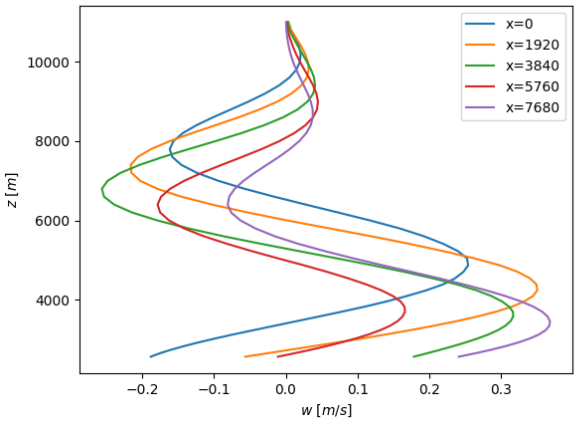

Figure 5.56: Vertical velocity with height for different streamwise locations for simulation PD1LES. It can be observed that the wavelike motion is adequately damped.

length. As reported in Subsection 5.1.2, the wavelength of the interfacial waves ranges from $3700\,\mathrm{m}$ to $4200\,\mathrm{m}$. Since it is assumed that the wavelength of the interfacial wave is approximately equal to the wavelength of the trapped gravity wave, the advection damping layer is thus sized correctly. At the beginning of the advection damping layer, where it overlaps with the inlet RDL, an accumulation of wave energy is visible in the vertical velocity field. As a consequence, spurious waves are generated at the boundary layer height. These spurious waves are only visible in the instantaneous results and therefore do not affect the analysis of the average variable fields. Furthermore, the spurious waves travel upwards and are subsequently handled by the top RDL. In conclusion, the observed spurious waves do not affect the results.

Finally, it was assumed that the domain width of $12\,000\,\mathrm{m}$ is sufficient and that the waves exiting through the lateral boundaries are not reintroduced into the domain since the symmetry in the flow acts as a mirror at the boundary. As observed in the vertical velocity field in the $x-y$-plane just above the capping inversion, as shown in Figure 5.57, the 'mirror' is not located exactly at the lateral boundary due to the slight asymmetry in the flow as a result of the Coriolis effect. However, the reintroduced waves at the lateral boundary mirror the exiting waves away from the farm, and therefore the smaller domain width is deemed to not influence the results.

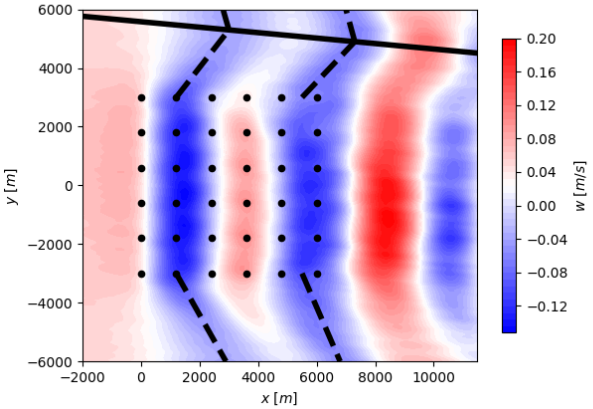

Figure 5.57: Vertical velocity field just above the capping inversion for simulation SFSNU1LES, where the solid line shows the location where the exiting wave is mirrored by the reintroduced wave.

5.5.4. Validation of MSC Results

The non-local, wake, and farm efficiency are suitable metrics for validating the MSC results. Even though in its essence the present section is a verification of the MSC results since a code-to-code comparison is presented, the term validation is used, since the LES results are here assumed to be the ground truth.

Table 5.2, Table 5.3, and Table 5.4 show the non-local, wake, and farm efficiency respectively, in a comparison between the MSC model using the Nieuwstadt inflow profiles, the MSC model using the precursor inflow profiles, and the LES results. Furthermore, the last column shows the error of the efficiency based on the MSC model using the precursor data, and the LES results as the 'truth'. The error is determined using Equation 5.14.

$$\text{error} = \frac{\eta_{LES} - \eta_{MSC}}{\eta_{LES}} \cdot 100\% \tag{5.14}$$

Table 5.2: Comparison of the non-local efficiency between the MSC model using the Nieuwstadt model, the MSC model using the precursor data, and the LES results. The relative error of the MSC model using the precursor data with respect to the LES results is shown on the right.

Identifier (MSC Nieuwstadt)	**Non-Local Efficiency** η_{nl}	**Identifier (MSC Precursor)**	**Non-Local Efficiency** η_{nl}	**Identifier (LES)**	**Non-Local Efficiency** η_{nl}	**Error**
PDL1MSC	0.593	PDL1MSC_P	0.612	PD1LES	0.417	47%
PDL3MSC	0.754	PDL3MSC_P	0.751	PD2LES	0.696	8%
PDL6MSC	0.878	PDL6MSC_P	0.870	PD3LES	0.898	3%
PDL8MSC	0.931	PDL8MSC_P	0.920	PD4LES	1.024	10%
SFSNU1MSC	0.832	SFSNU1MSC_P	0.826	SFSNU1LES	0.610	35%
SFSNU2MSC	0.805	SFSNU2MSC_P	0.787	SFSNU2LES	0.676	16%
SFSNU3MSC	0.811	SFSNU3MSC_P	0.807	SFSNU3LES	0.748	8%

It can be observed that the error is largest for simulations where the turbine spacing is small. This is an expected result, since for small turbine spacings, the perturbation is large. Since the MSC model is a linear model, large perturbations will give larger discrepancies. The non-local efficiency of simulation PD4LES is larger than one. Usually, the theoretical power is determined using an LES of the individual turbine. In the present study, the power is determined using Equation 5.11 and the difference in the theoretical power is assumed to explain the non-local efficiency being larger than one.

Table 5.3: Comparison of the wake efficiency between the MSC model using the Nieuwstadt model, the MSC model using the precursor data, and the LES results. The relative error of the MSC model using the precursor data with respect to the LES results is shown on the right.

Identifier (MSC Nieuwstadt)	**Wake Efficiency** η_w	**Identifier (MSC Precursor)**	**Wake Efficiency** η_w	**Identifier (LES)**	**Wake Efficiency** η_w	**Error**
PDL1MSC	0.239	PDL1MSC_P	0.147	PD1LES	0.587	75%
PDL3MSC	0.513	PDL3MSC_P	0.429	PD2LES	0.654	34%
PDL6MSC	0.655	PDL6MSC_P	0.615	PD3LES	0.704	13%
PDL8MSC	0.792	PDL8MSC_P	0.799	PD4LES	0.815	2%
SFSNU1MSC	0.518	SFSNU1MSC_P	0.461	SFSNU1LES	0.662	30%
SFSNU2MSC	0.895	SFSNU2MSC_P	0.897	SFSNU2LES	0.981	9%
SFSNU3MSC	0.729	SFSNU3MSC_P	0.650	SFSNU3LES	0.802	19%

Moreover, the error in the wake efficiency is in general larger than the error in the non-local efficiency. It is hypothesized that the inclusion of deep-array effects might improve the estimation of the MSC model since it will improve the estimation of the wake recovery at the exit of the farm. It is assumed that the error level can be related to the perturbation level, and since the perturbation level for simulation PDL1MSC represents an extreme case within this study, the MSC model performs well for the majority of the simulations.

Table 5.4: Comparison of the total farm efficiency between the MSC model using the Nieuwstadt model, the MSC model using the precursor data, and the LES results. The relative error of the MSC model using the precursor data with respect to the LES results is shown on the right.

Identifier (MSC Nieuwstadt)	**Farm Efficiency** η_f	**Identifier (MSC Precursor)**	**Farm Efficiency** η_f	**Identifier (LES)**	**Farm Efficiency** η_f	**Error**
PDL1MSC	0.141	PDL1MSC_P	0.090	PD1LES	0.245	63%
PDL3MSC	0.387	PDL3MSC_P	0.322	PD2LES	0.455	29%
PDL6MSC	0.575	PDL6MSC_P	0.536	PD3LES	0.632	15%
PDL8MSC	0.737	PDL8MSC_P	0.735	PD4LES	0.835	12%
SFSNU1MSC	0.431	SFSNU1MSC_P	0.381	SFSNU1LES	0.404	6%
SFSNU2MSC	0.721	SFSNU2MSC_P	0.706	SFSNU2LES	0.664	6%
SFSNU3MSC	0.591	SFSNU3MSC_P	0.525	SFSNU3LES	0.600	13%

To give an insight into the origin of the errors in the efficiencies, the streamwise perturbation and spanwise (lateral) velocity fields of the LES and MSC results are compared, analogously to the efficiencies above. Figure 5.58 and Figure 5.59 compare simulation PD1LES with PDL1MSC, for which the error in the efficiencies is largest. The error is scaled with the reference velocity and is determined using Equation 5.15.

$$\text{error} = \frac{U'_{LES} - U'_{MSC}}{U_{ref}} \cdot 100\% \quad \text{or} \quad \text{error} = \frac{V_{LES} - V_{MSC}}{U_{ref}} \cdot 100\% \tag{5.15}$$

There are two main effects that are visible. First of all, the streamwise (perturbation) velocity plot in Figure 5.58 shows that the error is only significant in the wake of the turbines. This is an expected result since the representation of the turbines is different in the LES framework and MSC model. However, as a consequence the turbine power generation can differ, causing differences in the efficiencies. As discussed above, including the deep-array effects in the MSC model might improve the match.

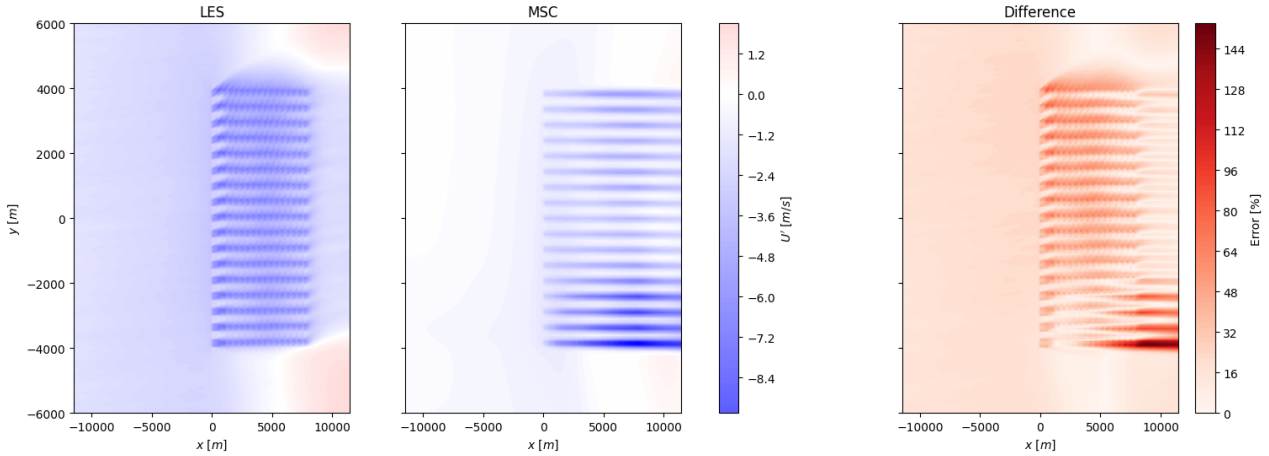

Figure 5.58: Comparison of the LES and MSC streamwise perturbation velocity fields together with the percentual difference, which is scaled with the reference velocity, for simulation PD1LES and PDL1MSC respectively, which have a square farm with a power density of $73\,\mathrm{MW\,km^{-2}}$.

Next, the spanwise velocity plot in Figure 5.59 shows that the flow field differs between the LES and MSC results. In the MSC results, there is a large area that has a negative lateral velocity, indicating that the flow goes around the farm. This is not visible in the LES results, where the spanwise velocity field is more uniform. It is possible that the flow is restricted due to the smaller domain size (than the MSC simulations), and it is forced in the streamwise direction. However, the LES results are deemed not to be affected, because if the sideways 'expansion' of the flow is restricted, one would expect a significant increase in streamwise velocity on the sides of the farm, which is not present. Only further downstream the streamwise velocity increases, but this effect is also visible in the MSC results. It must be noted that the above is not a direct comparison, since the MSC results are depth-averaged. This depth-averaged solution is supposed to represent the solution at hub height, which is why it is compared to the LES solution at hub height. However, the spanwise velocity is also influenced by the Coriolis effect, which on its turn is affected by the height. Consequently, the difference

in spanwise velocity might also be (partly) attributed to the fact that the MSC solution is depth-averaged, while the LES results are not. Note that the analysis for other simulations is similar (although the above effects are less pronounced), and the reader is referred to Appendix C for the visualization of the flow fields for all simulations (that have an LES counterpart).

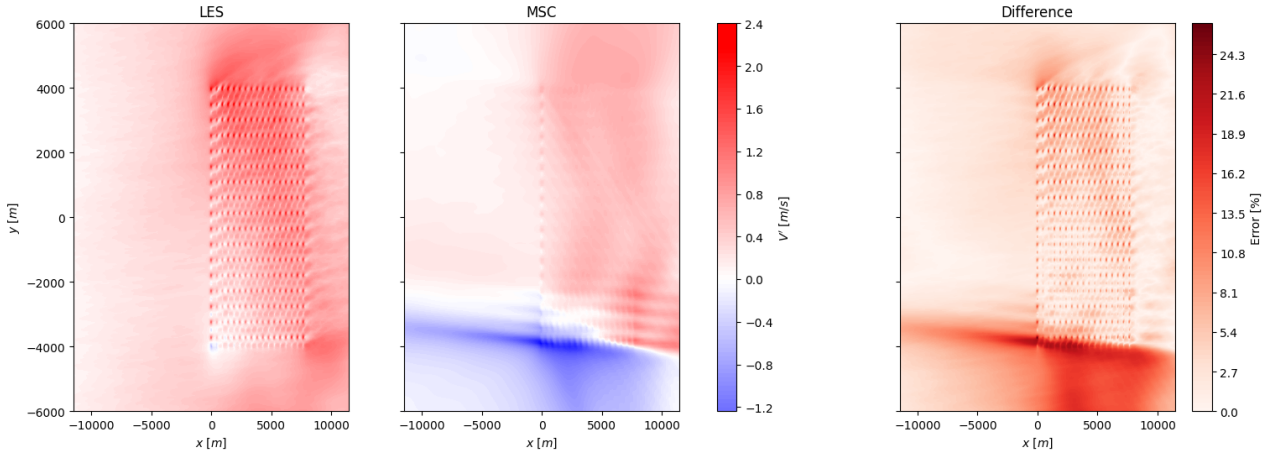

Figure 5.59: Comparison of the LES and MSC spanwise velocity fields together with the percentual difference, which is scaled with the reference velocity, for simulation PD1LES and PDL1MSC respectively, which have a square farm with a power density of $73\,\mathrm{MW\,km^{-2}}$.

Finally, a comparison can be made between the atmospheric boundary layer displacement obtained from either the LES or MSC results. The discussion of the differences between the two solutions must be prefaced by indicating the different ways of obtaining the atmospheric boundary layer displacement. Within the LES framework, the atmospheric boundary layer displacement is obtained by tracing a streamline using the streamwise and vertical velocity fields. On the other hand, the atmospheric boundary layer displacement is an integral part of the solution of the MSC model. It is hypothesized that this might give an unfair comparison between the absolute atmospheric boundary layer displacement of the two solution. For example, selecting a lower streamline from the LES results might result in a better match. The visualized streamline is that of the middle of the capping inversion. Consequently, the analysis of the error will be qualitative in nature.

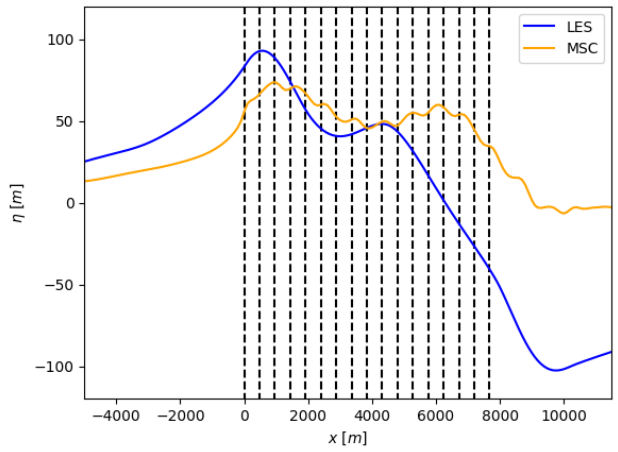

Figure 5.60: Comparison of the LES and MSC atmospheric boundary layer displacement together with the percentual difference, which is scaled with the capping inversion height, for simulation PD1LES and PDL1MSC respectively, which have a square farm with a power density of $73\,\mathrm{MW\,km^{-2}}$. The turbine locations are indicated with dashed lines.

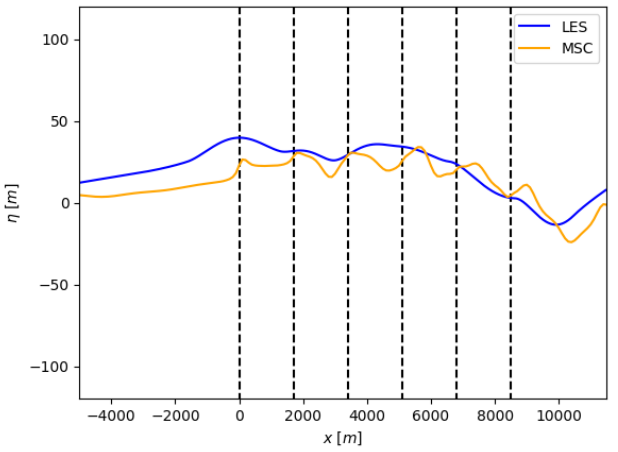

Figure 5.61: Comparison of the LES and MSC atmospheric boundary layer displacement together with the percentual difference, which is scaled with the capping inversion height, for simulation SFSNU3LES and SFSNU3MSC respectively, which have a square farm with a power density of $15\,\mathrm{MW\,km^{-2}}$. The turbine locations are indicated with dashed lines.

Figure 5.60 shows the atmospheric boundary layer displacement for simulations PD1LES (in blue) and PDL1MSC (in orange). Here, the difference between the LES and MSC results is maximal, which is also visible in the efficiencies and flow fields above. As expected, the linearity of the MSC model will yield larger errors when the perturbation is large. Indeed, the deviation from the LES results is significant, especially at

the exit of the farm. However, it must be noted that the MSC model captures the correct qualitative behaviour, with two peaks in the displacement within the length of the farm. It can also be noted that the perturbations due to the individual turbines are visible in the MSC results, while they are not in the LES results. When the perturbations are smaller, the match significantly improves, which is visible in Figure 5.61, where simulations SFSNU3LES (in blue) and SFSNU3MSC (in orange) are compared. For a comparison of the atmospheric boundary layer displacement for other simulations, the reader is again referred to Appendix C.

6

Conclusion

The present chapter aims to summarize the findings from Chapter 5 and present the conclusions in a comprehensive way. To do so, Section 6.1 lists the main conclusions of this study. Next, Section 6.2 intents to find exploratory guidelines that serve as a practical output of the research. Finally, Section 6.3 does recommendations for future work that build on or extend the present thesis.

6.1. Summary of Findings

The list below summarizes the main conclusions of the current thesis. The order of the conclusions is dictated by their appearance in Chapter 5.

- The Froude number that governs the internal waves is determined using the geostrophic velocity, the Brunt-Väisälä frequency, and a characteristic length scale. For square farms, this characteristic length scale is indeed the length of the wind farm for small to moderate turbine spacings. At large turbine spacings, the suggested length scale is the equivalent turbine spacing. The cross-over point between the two length scales is expected to be somewhere between $8D$ and $16D$. Consequently, the farm length is the characteristic length scale for practical turbine spacings. It is assumed that the length scales can be extended to rectangular farms, and farms where the streamwise and spanwise turbine spacings are different.

- The Froude number that governs the internal waves includes a characteristic length scale, as mentioned above. For non-uniform farms, this characteristic length scale is suggested to be the farm length averaged in the spanwise direction, or in other words, the farm's surface area divided by the farm's width.

- The inversion Froude number that governs the interfacial waves is determined using the geostrophic velocity, the reduced gravity, and a characteristic length scale, as deduced from shallow-water theory. For both uniform and non-uniform farms, the capping inversion height, or equivalently, the atmospheric boundary layer height is indeed the characteristic length scale when the turbine spacing is small to moderate. The dominant interfacial waves are in this case caused by the perturbations induced by the wind farm as an entity. When the turbine spacing is large, the dominant interfacial waves are caused by the perturbations induced by the individual turbines. The phase speed of the interfacial waves should in this case be determined using deep-water theory, as the assumptions on the forcing length scale (which was previously the farm length) from shallow-water theory seem to be violated. As a result, the characteristic length scale is a function of the capping inversion height and the equivalent turbine spacing. This result can readily be extended to non-uniform farms, given that the effective turbine spacing in the streamwise and spanwise directions are used. The cross-over point is observed to be in the vicinity of a turbine spacing of $8D$. Below this spacing, the interfacial waves are governed by the inversion Froude number which is defined with the phase speed determined from shallow-water theory. Above this spacing, the interfacial waves are governed by the inversion Froude number which is defined with the phase speed determined from deep-water theory.

- As a result of the above conclusions, a farm is assumed to act as an entity when the turbine spacing is significantly below $8D$, while significantly above this turbine spacing the farm acts as a collection of individual turbines.

- The wavelength of the interfacial wave that is associated with the shallow-water inversion Froude number does not change with the power density, streamwise or spanwise turbine spacing, aspect ratio, horizontal

staggering angle, rotor diameter, hub height (of a vertically staggered farm), or the orientation of the farm with respect to the freestream. It is assumed (and argued) that the wavelength that can be extracted from the streamwise background velocity field is indeed the wavelength of the interfacial wave.

- When the length of a wind farm is constant, the non-local efficiency is primarily governed by the streamwise and spanwise turbine spacing (and consequently the power density), and the aspect ratio.
- When a non-uniform farm is rotated with respect to the freestream, it is the effective streamwise and spanwise turbine spacing that is critical in the determination of the non-local and wake efficiency.
- When the number of turbines of a farm is constant, the effect of the streamwise and spanwise spacing on the non-local efficiency is less pronounced.
- When the number of turbines of a farm is constant, the non-local efficiency displays a minimum at an aspect ratio of approximately $1.5 - 2$.

6.2. Exploratory Guidelines for Wind Farm Design

The present section will bundle the conclusions related to wind farm performance, to give exploratory guidelines for wind farm design from the perspective of this study. In other words, the present section tries to overlook the OFAT methodology applied in this thesis to advise on a certain wind farm layout.

If the requirements allow for a certain number of turbines, the ideal farm is very wide and short, to achieve a low aspect ratio. The turbines are horizontally staggered, as well as vertically staggered, where the odd turbine rows are elevated. The streamwise turbine spacing is as large as possible, while the spanwise turbine spacing is large to increase the wind farm width.

If the requirements allow for a certain plot of land, the spanwise turbine spacing should be approximately $4D$, while the streamwise turbine spacing should be as large as possible. Furthermore, the farm should be horizontally and vertically staggered. Vertical staggering is achieved by elevating the odd turbine rows.

It is essential to note that these statements are highly introductory, as they only serve to show that the present study has real-life applicability. Indeed, the statements are only based on the efficiency of the wind farm (not on total power generation) and do not include the many factors involved in wind farm (site) design.

6.3. Recommendations for Future Work

The list below enumerates the recommendations for future work that can act as an extension or improvement of the present work.

- To strengthen the selection of new characteristic length scales for non-uniform or sparse farms, more turbine spacings and more farm shapes need to be considered to increase the resolution in the data. Furthermore, different turbines and atmospheric states need to be considered to extend the scope of the suggested length scales. Different turbines are also necessary to investigate whether the cross-over point between length scales is determined by the non-dimensional or dimensional turbine spacing. Finally, the streamwise and spanwise turbine spacings should be varied independently to verify whether the equivalent turbine spacing or either the streamwise or spanwise spacing is the dominant parameter.
- It should be investigated whether the aspect ratio, horizontal staggering angle, rotor diameter, or the hub height (of a vertically staggered farm) has an influence on the wavelength of the interfacial wave associated with the deep-water inversion Froude number.
- It is recommended to study what the first-row turbines are for a non-uniform or rotated farm, as the non-local efficiency is highly dependent on which turbines are included in the average power generation of the first-row power output.
- It is recommended to extend the present work to higher latitudes and subcritical (both shallow-water and deep-water) inversion Froude numbers.
- It is suggested to extend the present work to different boundary layer types or onshore conditions.
- It should be investigated how the equivalent turbine spacing must be determined for rotated or non-uniform farms.
- It is recommended to investigate the influence of including deep-array effects in the MSC model.

- It is recommended to study the influence of the turbine representation on the results, such as a varying thrust and power coefficient for the MSC model, or the usage of the actuator line model (ALM), or actuator disk model with rotation in the LES framework.

A

Simulation Suite

Table A.1: Abbreviations used in simulation identifiers. All identifiers consist of a combination of the below abbreviations and a number.

Abbreviation	Explanation
AR	Aspect Ratio
CFSNU	Circular Farm Shape Non-Uniformity
EFSNU	Elliptic Farm Shape Non-Uniformity
FL	Farm Length
FLNU	Farm Layout Non-Uniformity
HH	Hub Height
HS	Horizontal Staggering
PD	Power Density
RD	Rotor Diameter
RFSNU	Rectangular Farm Shape Non-Uniformity
SFSNU	Square Farm Shape Non-Uniformity
TFSNU	Triangular Farm Shape Non-Uniformity
TSX	Streamwise Turbine Spacing
TSY	Spanwise Turbine Spacing
VS	Vertical Staggering
VSR	Reverse Vertical Staggering
T	Constant Number of Turbines
L	Constant Farm Length
MSC	Multi-Scale Coupled model
LES	Large Eddy Simulation

Table A.2: Simulation suite.

Identifier	Number of Turbines $N_{T_x} \times N_{T_y}$ or N_T	Turbine Spacing $s_x \times s_y$ or $\bar{s}$	Wind Farm Size $L_{f_x} \times L_{f_y}$ or $L_{f_\varnothing}$ [km]	Orientation Φ [°]	Staggering Angle $\tilde{\psi}$	Aspect Ratio AR	Power Density Π [MW km^{-2}]	Hub Height $h_{\mathrm{hub,odd}} \times h_{\mathrm{hub,even}}$ or h_{hub} [m]	Rotor Diameter D [m]
ART1MSC	2×11	5×5	1.20×12.00	0	0	10	22.92	150	240
ART2MSC	3×9	5×5	2.40×9.60	0	0	4	17.58	150	240
ART3MSC	4×7	5×5	3.60×7.20	0	0	2	16.20	150	240
ART4MSC	5×5	5×5	4.80×4.80	0	0	1	16.28	150	240
ART5MSC	7×4	5×5	7.20×3.60	0	0	0.5	16.20	150	240
ART6MSC	9×3	5×5	9.60×2.40	0	0	0.25	17.58	150	240
ART7MSC	11×2	5×5	12.00×1.20	0	0	0.1	22.92	150	240
ARL1MSC	5×2	5×5	4.80×1.20	0	0	0.25	26.04	150	240
ARL2MSC	5×3	5×5	4.80×2.40	0	0	0.5	19.53	150	240
ARL3MSC	5×4	5×5	4.80×3.60	0	0	0.75	17.36	150	240
ARL4MSC	5×5	5×5	4.80×4.80	0	0	1	16.28	150	240
ARL5MSC	5×6	5×5	4.80×6.00	0	0	1.25	15.63	150	240
ARL6MSC	5×7	5×5	4.80×7.20	0	0	1.5	15.19	150	240
ARL7MSC	5×8	5×5	4.80×8.40	0	0	1.75	14.88	150	240
ARL8MSC	5×9	5×5	4.80×9.60	0	0	2	14.65	150	240
ARL9MSC	5×10	5×5	4.80×10.80	0	0	2.25	14.47	150	240
ARL10MSC	5×11	5×5	4.80×12.00	0	0	2.5	14.32	150	240
ARL11MSC	5×12	5×5	4.80×13.20	0	0	2.75	14.20	150	240
ARL12MSC	5×13	5×5	4.80×14.40	0	0	3	14.11	150	240
ART13MSC	5×14	5×5	4.80×15.60	0	0	3.25	14.02	150	240
ART14MSC	5×15	5×5	4.80×16.80	0	0	3.5	13.95	150	240
ART15MSC	5×16	5×5	4.80×18.00	0	0	3.75	13.89	150	240
ART16MSC	5×17	5×5	4.80×19.20	0	0	4	13.83	150	240
CFSNU1MSC	37	5	⌀6.9	0	N/A	N/A	15.10	150	240
EFSNU1MSC	39	5	⌀10.5×4.8	0	N/A	N/A	15.92	150	240
EFSNU2MSC	39	5	⌀10.5×4.8	45	N/A	N/A	15.92	150	240
EFSNU3MSC	39	5	⌀10.5×4.8	90	N/A	N/A	15.92	150	240
EFSNU3MSC	39	5	⌀10.5×4.8	-45	N/A	N/A	15.92	150	240
FL1MSC	2×5	5×5	1.20×4.80	0	0	4	26.04	150	240
FL2MSC	3×5	5×5	2.40×4.80	0	0	4	19.53	150	240
FL3MSC	4×5	5×5	3.60×4.80	0	0	4	17.36	150	240
FL4MSC	5×5	5×5	4.80×4.80	0	0	4	16.28	150	240
FL5MSC	6×5	5×5	6.00×4.80	0	0	4	15.63	150	240
FL6MSC	7×5	5×5	7.20×4.80	0	0	4	15.19	150	240
FL7MSC	8×5	5×5	8.40×4.80	0	0	4	14.88	150	240
FL8MSC	9×5	5×5	9.60×4.80	0	0	4	14.65	150	240
FL9MSC	10×5	5×5	10.80×4.80	0	0	4	14.47	150	240
FL10MSC	11×5	5×5	12.00×4.80	0	0	4	14.32	150	240

Continued on next page

Table A.2 – continued from previous page

Identifier	Number of Turbines $N_{T_x} \times N_{T_y}$ or N_T	Turbine Spacing $s_x \times s_y$ or $\bar{s}$	Wind Farm Size $L_{f_x} \times L_{f_y}$ or $L_{f_\circ}$ [km]	Orientation Φ [°]	Staggering Angle $\tilde{\psi}$	Aspect Ratio A	Power Density Π [MW km^{-2}]	Hub Height $h_{\mathrm{hub,odd}}$ or $h_{\mathrm{hub,even}}$ or h_{hub} [m]	Rotor Diameter D [m]
FL11MSC	12×5	5×5	13.20×4.80	0	0	4	14.20	150	240
FLNU1MSC	74	7.1	14.63×23.63	0	N/A	N/A	6.11	150	240
FLNU2MSC	74	2.2[1]	14.63×23.63	0	N/A	N/A	6.11	150	240
HH1MSC	5×5	5×5	4.80×4.80	0	0	1	16.28	145	240
HH2MSC	5×5	5×5	4.80×4.80	0	0	1	16.28	160	240
HH3MSC	5×5	5×5	4.80×4.80	0	0	1	16.28	175	240
HH4MSC	5×5	5×5	4.80×4.80	0	0	1	16.28	190	240
HH5MSC	5×5	5×5	4.80×4.80	0	0	1	16.28	205	240
HS1MSC	5×5	5×5	4.80×4.80	0	0	1	16.28	150	240
HS2MSC	5×5	5×5	4.80×4.94	0	0.25	1	15.81	150	240
HS3MSC	5×5	5×5	4.80×5.08	0	0.5	1	15.38	150	240
HS4MSC	5×5	5×5	4.80×5.23	0	0.75	1	14.94	150	240
HS5MSC	5×5	5×5	4.80×5.40	0	1	1	14.47	150	240
PDL1LES	17×17	2×2	7.68×7.68	0	0	1	73.50	150	240
PDL2LES	9×9	4×4	7.68×7.68	0	0	1	20.60	150	240
PDL3LES	5×5	8×8	7.68×7.68	0	0	1	6.36	150	240
PDL4LES	3×3	16×16	7.68×7.68	0	0	1	2.29	150	240
PDL1MSC	17×17	2×2	7.68×7.68	0	0	1	73.50	150	240
PDL2MSC	11×11	3.2×3.2	7.68×7.68	0	0	1	30.77	150	240
PDL3MSC	9×9	4×4	7.68×7.68	0	0	1	20.60	150	240
PDL4MSC	7×7	5.3×5.3	7.68×7.68	0	0	1	12.46	150	240
PDL5MSC	6×6	6.4×6.4	7.68×7.68	0	0	1	9.16	150	240
PDL6MSC	5×5	8×8	7.68×7.68	0	0	1	6.36	150	240
PDL7MSC	4×4	10.7×10.7	7.68×7.68	0	0	1	4.07	150	240
PDL8MSC	3×3	16×16	7.68×7.68	0	0	1	2.29	150	240
PDL1MSC_NC	17×17	2×2	7.68×7.68	0	0	1	73.50	150	240
PDL2MSC_NC	11×11	3.2×3.2	7.68×7.68	0	0	1	30.77	150	240
PDL3MSC_NC	9×9	4×4	7.68×7.68	0	0	1	20.60	150	240
PDL4MSC_NC	7×7	5.3×5.3	7.68×7.68	0	0	1	12.46	150	240
PDL5MSC_NC	6×6	6.4×6.4	7.68×7.68	0	0	1	9.16	150	240
PDL6MSC_NC	5×5	8×8	7.68×7.68	0	0	1	6.36	150	240
PDL7MSC_NC	4×4	10.7×10.7	7.68×7.68	0	0	1	4.07	150	240
PDL8MSC_NC	3×3	16×16	7.68×7.68	0	0	1	2.29	150	240
PDL1MSC_P	17×17	2×2	7.68×7.68	0	0	1	73.50	150	240
PDL2MSC_P	11×11	3.2×3.2	7.68×7.68	0	0	1	30.77	150	240
PDL3MSC_P	9×9	4×4	7.68×7.68	0	0	1	20.60	150	240

Continued on next page

[1] Minimum spacing

Table A.2 – continued from previous page

Identifier	Number of Turbines $N_{T_x} \times N_{T_y}$ or N_T	Turbine Spacing $s_x \times s_y$ or $\bar{s}$	Wind Farm Size $L_{f_x} \times L_{f_y}$ or $L_{f_\circ}$ [km]	Orientation Φ [°]	Staggering Angle $\tilde{\psi}$	Aspect Ratio A	Power Density Π [MW km^{-2}]	Hub Height $h_{\mathrm{hub,odd}}$ or $h_{\mathrm{hub,even}}$ or h_{hub} [m]	Rotor Diameter D [m]
PDL4MSC_P	7×7	5.3×5.3	7.68×7.68	0	0	1	12.46	150	240
PDL5MSC_P	6×6	6.4×6.4	7.68×7.68	0	0	1	9.16	150	240
PDL6MSC_P	5×5	8×8	7.68×7.68	0	0	1	6.36	150	240
PDL7MSC_P	4×4	10.7×10.7	7.68×7.68	0	0	1	4.07	150	240
PDL8MSC_P	3×3	16×16	7.68×7.68	0	0	1	2.29	150	240
PDT1MSC	5×5	3×3	2.88×2.88	0	0	1	45.21	150	240
PDT2MSC	5×5	4×4	3.84×3.84	0	0	1	25.43	150	240
PDT3MSC	5×5	5×5	4.80×4.80	0	0	1	16.28	150	240
PDT4MSC	5×5	6×6	5.76×5.76	0	0	1	11.30	150	240
PDT5MSC	5×5	7×7	6.72×6.72	0	0	1	8.30	150	240
PDT6MSC	5×5	8×8	7.68×7.68	0	0	1	6.36	150	240
PDT7MSC	5×5	9×9	8.64×8.64	0	0	1	5.02	150	240
PDT8MSC	5×5	10×10	9.60×9.60	0	0	1	4.07	150	240
PDT9MSC	5×5	11×11	10.56×10.56	0	0	1	3.36	150	240
PDT10MSC	5×5	12×12	11.52×11.52	0	0	1	2.83	150	240
RD1MSC	5×5	5×5	4.80×4.80	0	0	1	16.28	150	220
RD2MSC	5×5	5×5	4.80×4.80	0	0	1	16.28	150	230
RD3MSC	5×5	5×5	4.80×4.80	0	0	1	16.28	150	240
RD4MSC	5×5	5×5	4.80×4.80	0	0	1	16.28	150	250
RFSNU1MSC	9×4	5×5	9.60×3.60	0	0	0.375	15.63	150	240
RFSNU2MSC	9×4	5×5	9.60×3.60	20.6	0	0.375	15.63	150	240
RFSNU3MSC	9×4	5×5	9.60×3.60	22.5	0	0.375	15.63	150	240
RFSNU4MSC	9×4	5×5	9.60×3.60	45	0	0.375	15.63	150	240
RFSNU5MSC	9×4	5×5	9.60×3.60	67.5	0	0.375	15.63	150	240
RFSNU6MSC	9×4	5×5	9.60×3.60	90	0	0.375	15.63	150	240
RFSNU7MSC	9×4	5×5	9.60×3.60	-20.6	0	0.375	15.63	150	240
RFSNU8MSC	9×4	5×5	9.60×3.60	-22.5	0	0.375	15.63	150	240
RFSNU9MSC	9×4	5×5	9.60×3.60	-45	0	0.375	15.63	150	240
RFSNU10MSC	9×4	5×5	9.60×3.60	-67.5	0	0.375	15.63	150	240
SFSNU1LES	6×6	5×5	6.00×6.00	0	0	1	15	150	240
SFSNU2LES	6×6	5×5	6.00×6.00	22.5	0	1	15	150	240
SFSNU3LES	6×6	5×5	6.00×6.00	45	0	1	15	150	240
SFSNU1MSC	6×6	5×5	6.00×6.00	0	0	1	15	150	240
SFSNU2MSC	6×6	5×5	6.00×6.00	22.5	0	1	15	150	240
SFSNU3MSC	6×6	5×5	6.00×6.00	45	0	1	15	150	240
SFSNU4MSC	6×6	5×5	6.00×6.00	-22.5	0	1	15	150	240
SFSNU1MSC_P	6×6	5×5	6.00×6.00	0	0	1	15	150	240
SFSNU2MSC_P	6×6	5×5	6.00×6.00	22.5	0	1	15	150	240

Continued on next page

Table A.2 – continued from previous page

Identifier	Number of Turbines $N_{T_x} \times N_{T_y}$ or N_T	Turbine Spacing $s_x \times s_y$ or $\bar{s}$	Wind Farm Size $L_{f_x} \times L_{f_y}$ or $L_{f_\circ}$ [km]	Orientation Φ [°]	Staggering Angle $\tilde{\psi}$	Aspect Ratio A	Power Density Π [MW km^{-2}]	Hub Height $h_{\mathrm{hub,odd}}$ or $h_{\mathrm{hub,even}}$ or h_{hub} [m]	Rotor Diameter D [m]
SFSNU3MSC_P	6×6	5×5	6.00×6.00	45	0	1	15	150	240
SFSNU4MSC_P	6×6	5×5	6.00×6.00	-22.5	0	1	15	150	240
TFSNU1MSC	36	5	7.27×8.40	0	N/A	N/A	17.67	150	240
TFSNU2MSC	36	5	7.27×8.40	30	N/A	N/A	17.67	150	240
TFSNU3MSC	36	5	7.27×8.40	60	N/A	N/A	17.67	150	240
TFSNU4MSC	36	5	7.27×8.40	90	N/A	N/A	17.67	150	240
TSXL1MSC	17×9	2×4	7.68×7.68	0	0	1	38.91	150	240
TSXL2MSC	11×9	3.2×4	7.68×7.68	0	0	1	25.18	150	240
TSXL3MSC	9×9	4×4	7.68×7.68 0	0	1	20.60	150	240	
TSXL4MSC	7×9	5.3×4	7.68×7.68	0	0	1	16.02	150	240
TSXL5MSC	6×9	6.4×4	7.68×7.68	0	0	1	13.73	150	240
TSXL6MSC	5×9	8×4	7.68×7.68	0	0	1	11.44	150	240
TSXL7MSC	4×9	10.7×4	7.68×7.68	0	0	1	9.16	150	240
TSXL8MSC	3×9	16×4	7.68×7.68	0	0	1	6.87	150	240
TSXT1MSC	5×5	5×5	4.80×4.80	0	0	1	16.28	150	240
TSXT2MSC	5×5	6×5	5.76×4.80	0	0	0.83	13.56	150	240
TSXT3MSC	5×5	7×5	6.72×4.80	0	0	0.71	11.63	150	240
TSXT4MSC	5×5	8×5	7.68×4.80	0	0	0.63	10.17	150	240
TSXT5MSC	5×5	9×5	8.64×4.80	0	0	0.56	9.04	150	240
TSXT6MSC	5×5	10×5	9.60×4.80	0	0	0.5	8.14	150	240
TSXT7MSC	5×5	11×5	10.56×4.80	0	0	0.45	7.40	150	240
TSXT8MSC	5×5	12×5	11.52×4.80	0	0	0.42	6.78	150	240
TSYL1MSC	9×17	4×2	7.68×7.68	0	0	1	38.91	150	240
TSYL2MSC	9×11	4×3.2	7.68×7.68	0	0	1	25.18	150	240
TSYL3MSC	9×9	4×4	7.68×7.68 0	0	1	20.60	150	240	
TSYL4MSC	9×7	4×5.3	7.68×7.68	0	0	1	16.02	150	240
TSYL5MSC	9×6	4×6.4	7.68×7.68	0	0	1	13.73	150	240
TSYL6MSC	9×5	4×8	7.68×7.68	0	0	1	11.44	150	240
TSYL7MSC	9×4	4×10.7	7.68×7.68	0	0	1	9.16	150	240
TSYL8MSC	9×3	4×16	7.68×7.68	0	0	1	6.87	150	240
TSYT1MSC	5×5	5×3	4.80×2.88	0	0	0.6	27.13	150	240
TSYT2MSC	5×5	5×4	4.80×3.84	0	0	0.8	20.35	150	240
TSYT3MSC	5×5	5×5	4.80×4.80	0	0	1	16.28	150	240
TSYT4MSC	5×5	5×6	4.80×5.76	0	0	1.2	13.56	150	240
TSYT5MSC	5×5	5×7	4.80×6.72	0	0	1.4	11.63	150	240
TSYT6MSC	5×5	5×8	4.80×7.68	0	0	1.6	10.17	150	240
VS1MSC	5×5	5×5	4.80×4.80	0	0	1	16.28	150×145	240
VS2MSC	5×5	5×5	4.80×4.80	0	0	1	16.28	150×160	240

Continued on next page

Table A.2 – continued from previous page

Identifier	Number of Turbines $N_{T_x} \times N_{T_y}$ or N_T	Turbine Spacing $s_x \times s_y$ or $\bar{s}$	Wind Farm Size $L_{f_x} \times L_{f_y}$ or $L_{f_\circ}$ [km]	Orientation Φ [°]	Staggering Angle $\tilde{\psi}$	Aspect Ratio A	Power Density Π [MW km^{-2}]	Hub Height $h_{\mathrm{hub,odd}}$ or $h_{\mathrm{hub,even}}$ or h_{hub} [m]	Rotor Diameter D [m]
VS3MSC	5×5	5×5	4.80×4.80	0	0	1	16.28	150×175	240
VS4MSC	5×5	5×5	4.80×4.80	0	0	1	16.28	150×190	240
VS5MSC	5×5	5×5	4.80×4.80	0	0	1	16.28	150×205	240
VSR1MSC	5×5	5×5	4.80×4.80	0	0	1	16.28	145×150	240
VSR2MSC	5×5	5×5	4.80×4.80	0	0	1	16.28	160×150	240
VSR3MSC	5×5	5×5	4.80×4.80	0	0	1	16.28	175×150	240
VSR4MSC	5×5	5×5	4.80×4.80	0	0	1	16.28	190×150	240
VSR5MSC	5×5	5×5	4.80×4.80	0	0	1	16.28	205×150	240

B

LES Setup Files

ABLProperties.dat

```
# TOSCA Input file - ABL Properties
# ---------------------------------

# Reference velocity and height for the velocity controller.
uRef 9.21
hRef 150.0

# Reference potential temperature.
tRef 300.0

# Equivalent Roughness length.
hRough 0.0001

# Height of the center of the inversion layer.
hInv 500.0

# Width of the inversion layer.
dInv 100.0

# Potential temperature jump across the inversion layer.
gInv 5

# Potential temperature gradient on top of the inversion layer.
gTop 0.004

# Potential temperature gradient below the inversion layer.
gABL 0.000

# Von Karman Constant.
vkConst 0.4

# Rampanelli and Zardi temperature model parameter.
smearT 0.3

# Coriolis parameter: 2*7.272205217e-5 * sin(latitude)
fCoriolis 5.9204e-05

# Activation flags
coriolisActive 1
controllerActive 1
controllerActiveT 0
controllerActivePrecursorT 0
controllerTypeT   initial

controllerProperties
```

```
{
    # Velocity controller type (write->pressure/geostrphic/directProfileAssimilation, read->timeSeri
    controllerAction read
    controllerType timeAverageSeries

    uGeoMag 9.31

    # Velocity controller gain factor
    relaxPI 0.7

    # Velocity controller proportional over integral contribution ratio
    alphaPI 0.9

    # Velocity controller time filter
    timeWindowPI 3600

    # Velocity controller max height of influence
    controllerMaxHeight 100000.0

    # Start time for the given momentum source average (only controller type 'average')
    controllerAvgStartTime 100000.0

    # Perform geostrophic damping (only pressure controller)
    geostrophicDamping 0

    # Geostrophic height
    hGeo 900

    # Geostrophic angle
    alphaGeo 0
}

# Fringe layers properties (activate in the control.dat - zDampingLayer = 1, xDampingLayer = 1)
zDampingProperties
{
    zDampingStart   5750
    zDampingEnd     11000
    zDampingAlpha   0.1
    zDampingAlsoXY  0
    zDampingXYType  2
}

kLeftDampingProperties
{
    kLeftPatchDist      3500
    kLeftDampingAlpha   0.1
    kLeftDampingUBar    (9.21 -1.35 0.0)
    kLeftFilterHeight   500.0
    kLeftFilterWidth    100.0
}
advectionDampingProperties
{
    advDampingStart      -17500
    advDampingEnd        -11500
    advDampingDeltaStart  1000
    advDampingDeltaEnd    1000
}

#velocity perturbations to trigger turbulence
perturbations 0

```

control.dat

```
# OKWind Input file - Control.dat
# ---------------------------------

# Simulation
# ---------------------------------
-startFrom                 startTime
-startTime                 100000
-endTime                   110000
-cfl                       0.9
-adjustTimeStep            1
-timeStep                  0.5
-timePrecision             6

# Write Data
# ---------------------------------
-intervalType              adjustableTime
-timeInterval              250
-purgeWrite                1

# Solution
# ---------------------------------
-potentialT                1
-abl                       1
-zDampingLayer             1
-xDampingLayer             0
-kLeftRayleigh^^I^^I       1
-precursorSpinUp           0
-advectionDamping          1

-absTolU                   1e-7
-absTolT                   1e-7
-poissonIt                 8
-poissonTol                1e-6
-poissonSolver             HYPRE

# Turbulence Model
# ---------------------------------
-les                       4
-max_cs                    10

# Numerical Schemes
# ---------------------------------
-dUdtScheme                backwardEuler
-dTdtScheme                backwardEuler
-divScheme                 centralUpwindW

# Wind Turbine
# ---------------------------------
-windplant                 1

# Constants
# ---------------------------------
-nu                        1.5e-5
-rho                       1.225
-Pr                        0.71

# Mesh
# ---------------------------------
-meshFileType             cartesian

# Acquisition
# ---------------------------------
-probes                   0
```

```
-sections                1

-averageABL              1
-avgABLPeriod            10
-avgABLStartTime         103500.0

-average3LM              0
-perturbABL              1
-keBudgets               0

-averaging               1
-avgPeriod               10
-avgStartTime            103500.00

-pvCatalyst              0

# PostProcessing
# ---------------------------------
-writeRaster             0
-postProcessFields       0
-postProcessPrecursor    0

```

iSections

```
surfaceNumber 7
timeStart     100000
intervalType  adjustableTime
timeInterval  250
coordinates
-6000.0
-5000.0
-3840.0
0.0
3840.0
5000.0
6000.0
```

jSections

```
surfaceNumber 9
timeStart     100000
intervalType  adjustableTime
timeInterval  250
coordinates
0.0
150.0
400.0
500.0
600.0
1000.0
3000.0
5000.0
10000.0
```

kSections

```
surfaceNumber 8
timeStart     100000
intervalType  adjustableTime
timeInterval  250
coordinates
```

```
-20000.0
-18500.0
-14500.0
-9000.0
0.0
3840.0
7680.0
11500.0
```

C

MSC Validation

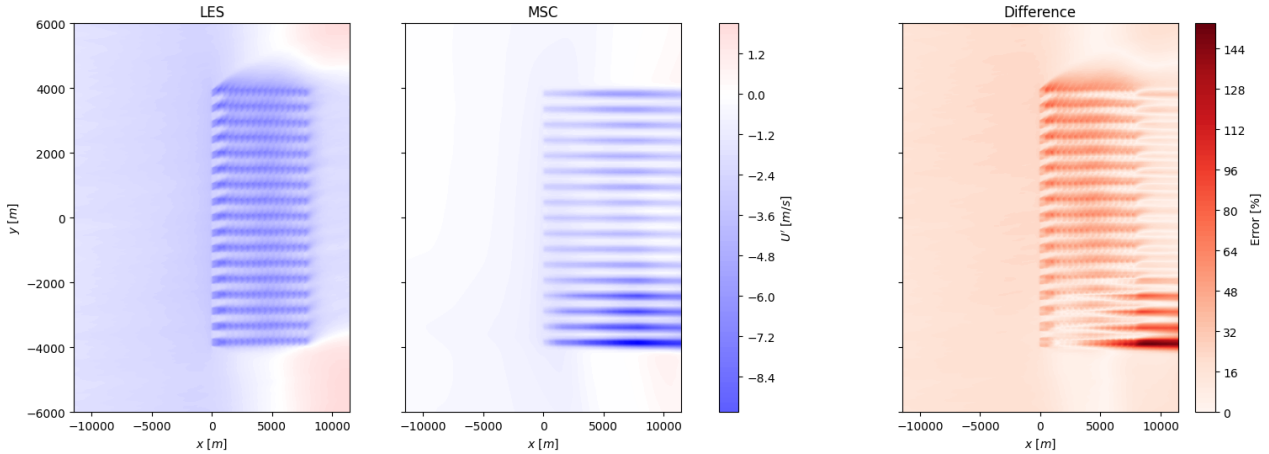

Figure C.1: Comparison of the LES and MSC streamwise perturbation velocity fields together with the percentual difference, which is scaled with the reference velocity, for simulation PD1LES and PDL1MSC respectively, which have a square farm with a power density of $73\,\mathrm{MW\,km^{-2}}$.

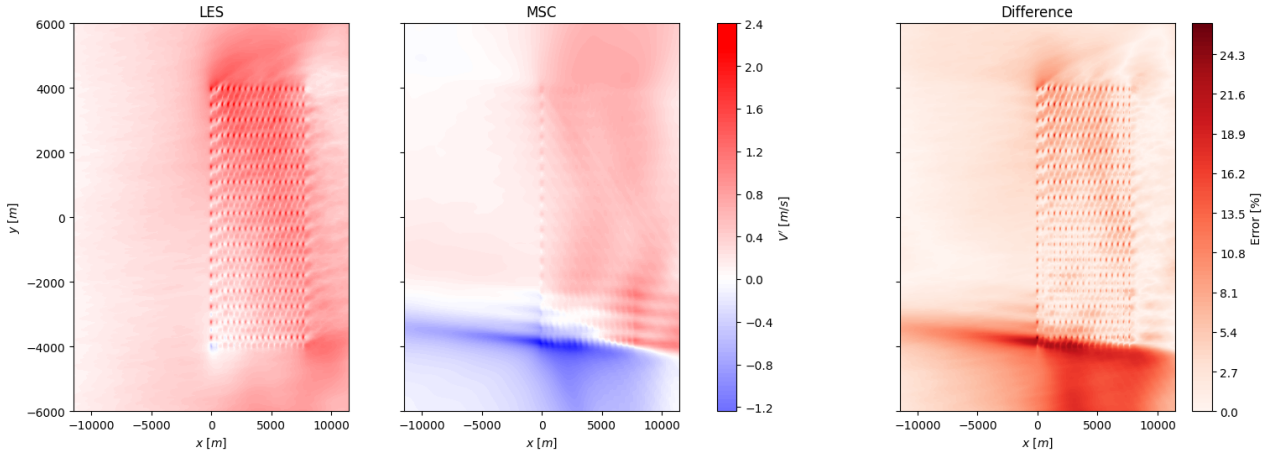

Figure C.2: Comparison of the LES and MSC spanwise velocity fields together with the percentual difference, which is scaled with the reference velocity, for simulation PD1LES and PDL1MSC respectively, which have a square farm with a power density of $73\,\mathrm{MW\,km^{-2}}$.

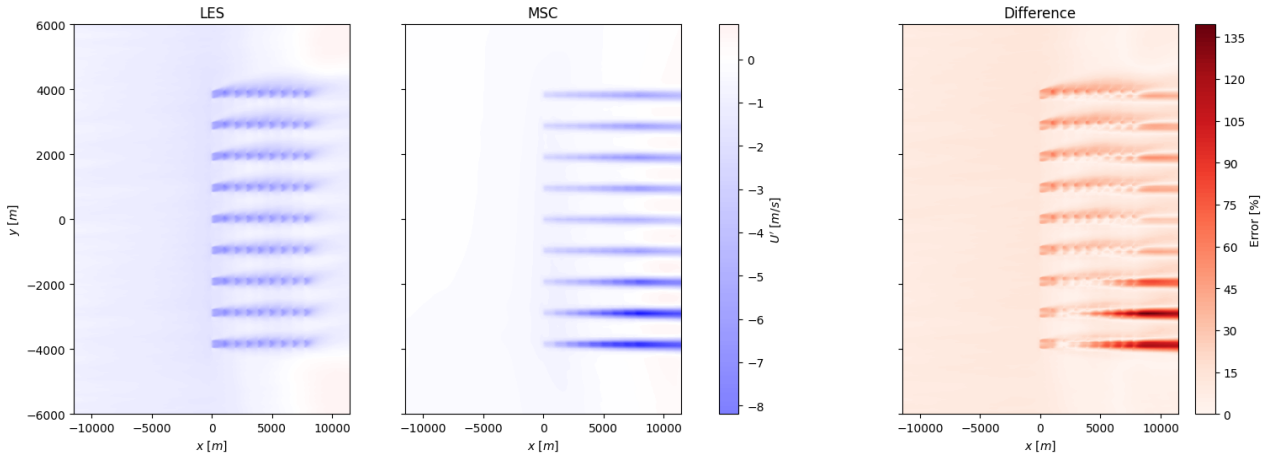

Figure C.3: Comparison of the LES and MSC streamwise perturbation velocity fields together with the percentual difference, which is scaled with the reference velocity, for simulation PD2LES and PDL3MSC respectively, which have a square farm with a power density of $21\,\mathrm{MW\,km^{-2}}$.

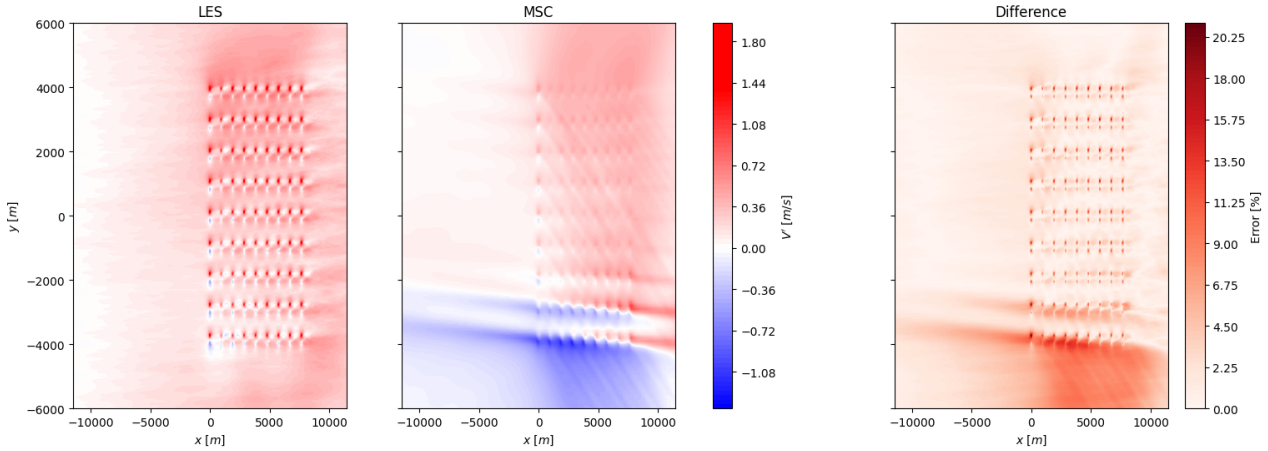

Figure C.4: Comparison of the LES and MSC spanwise velocity fields together with the percentual difference, which is scaled with the reference velocity, for simulation PD2LES and PDL3MSC respectively, which have a square farm with a power density of $21\,\mathrm{MW\,km^{-2}}$.

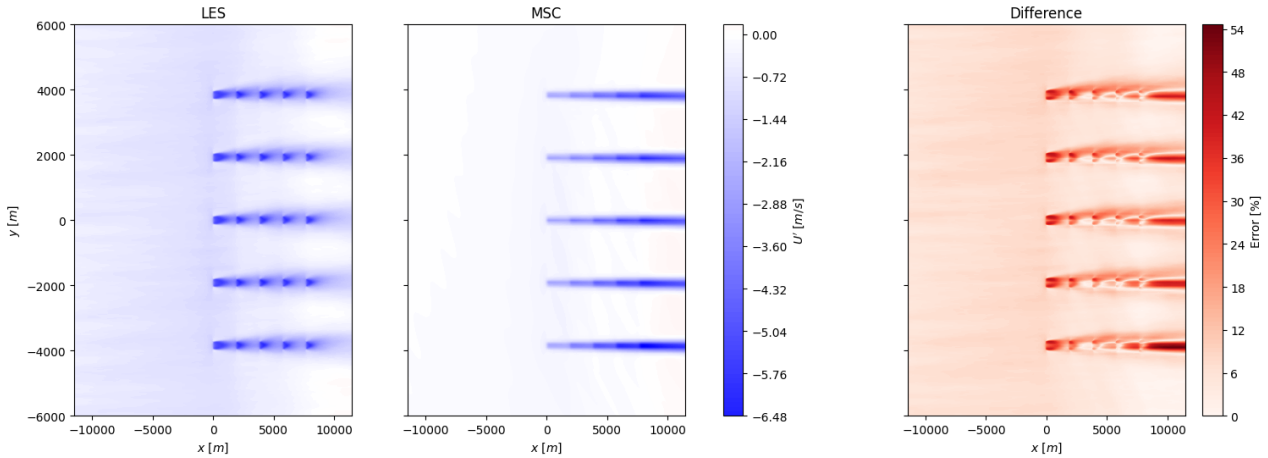

Figure C.5: Comparison of the LES and MSC streamwise perturbation velocity fields together with the percentual difference, which is scaled with the reference velocity, for simulation PD3LES and PDL6MSC respectively, which have a square farm with a power density of $6\,\mathrm{MW\,km^{-2}}$.

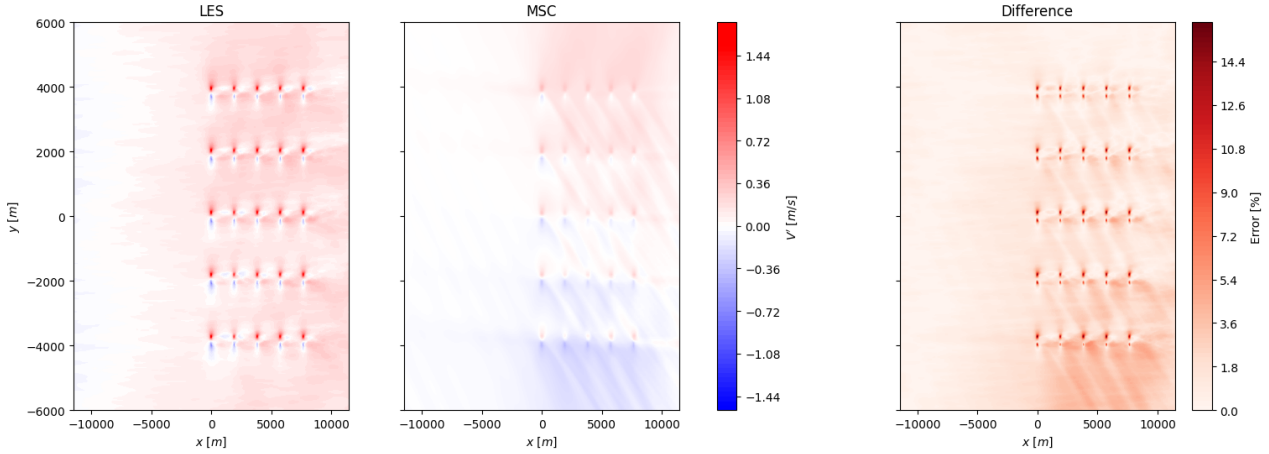

Figure C.6: Comparison of the LES and MSC spanwise velocity fields together with the percentual difference, which is scaled with the reference velocity, for simulation PD3LES and PDL6MSC respectively, which have a square farm with a power density of $6\,\mathrm{MW\,km^{-2}}$.

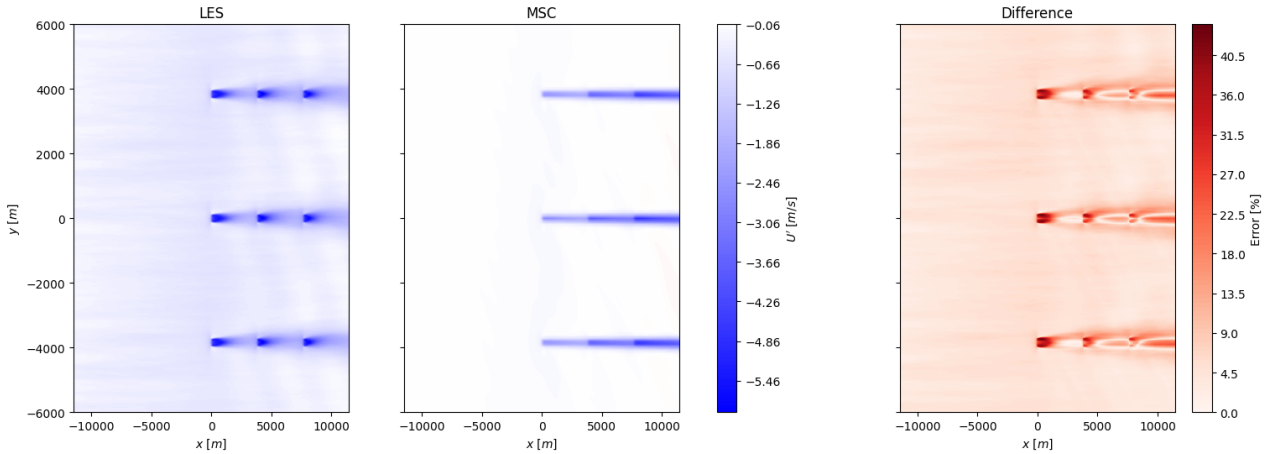

Figure C.7: Comparison of the LES and MSC streamwise perturbation velocity fields together with the percentual difference, which is scaled with the reference velocity, for simulation PD4LES and PDL8MSC respectively, which have a square farm with a power density of $2\,\mathrm{MW\,km^{-2}}$.

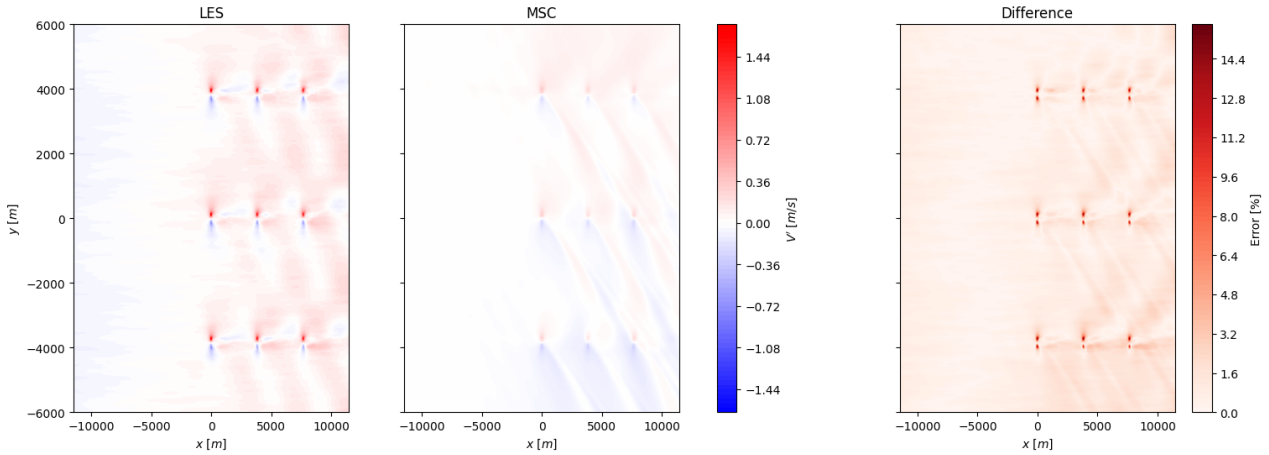

Figure C.8: Comparison of the LES and MSC spanwise velocity fields together with the percentual difference, which is scaled with the reference velocity, for simulation PD4LES and PDL8MSC respectively, which have a square farm with a power density of $2\,\mathrm{MW\,km^{-2}}$.

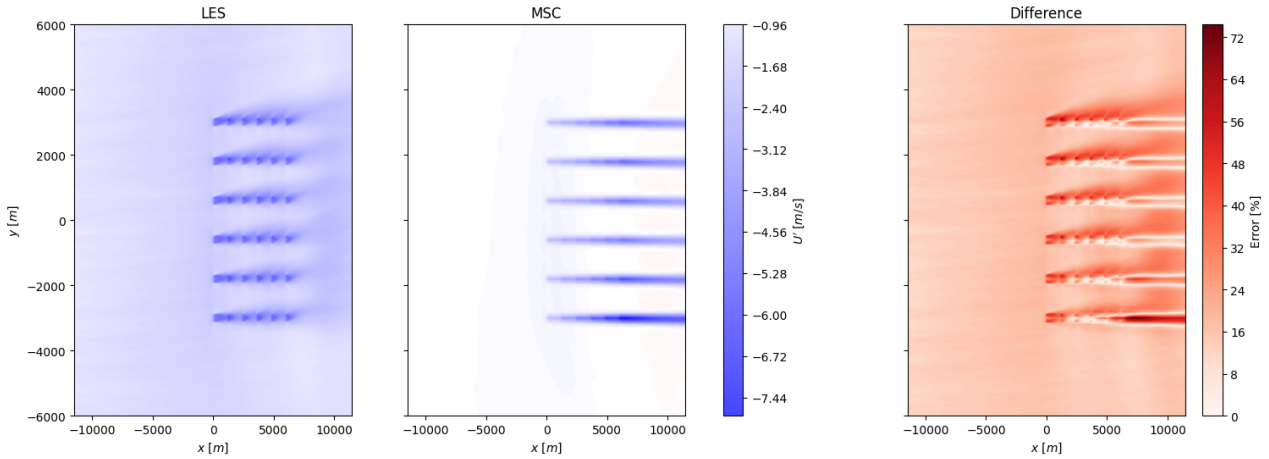

Figure C.9: Comparison of the LES and MSC streamwise perturbation velocity fields together with the percentual difference, which is scaled with the reference velocity, for simulation SFSNU1LES and SFSNU1MSC respectively, which have a square farm with a power density of $15\,\mathrm{MW\,km^{-2}}$.

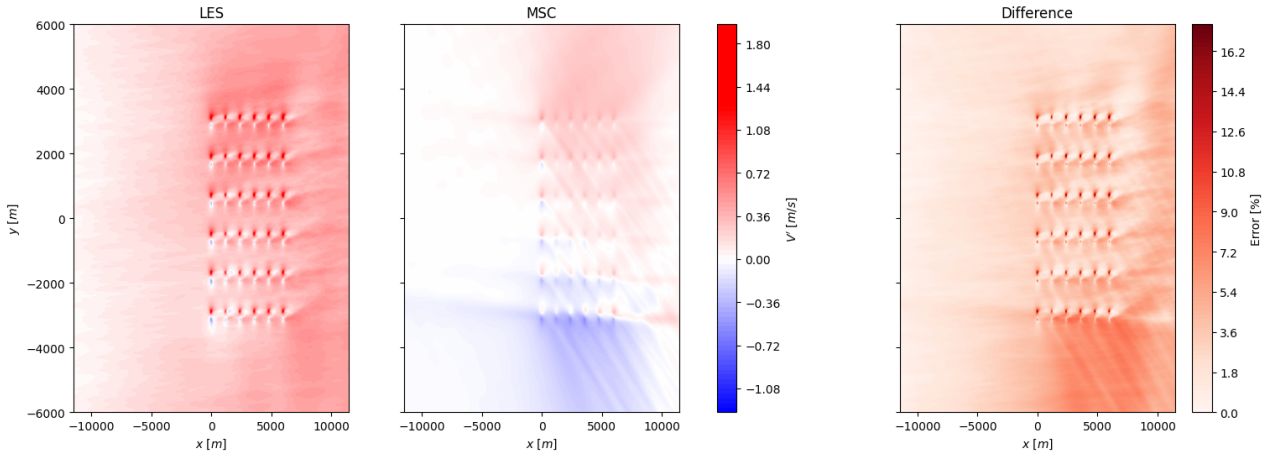

Figure C.10: Comparison of the LES and MSC spanwise velocity fields together with the percentual difference, which is scaled with the reference velocity, for simulation SFSNU1LES and SFSNU1MSC respectively, which have a square farm with a power density of $15\,\mathrm{MW\,km^{-2}}$.

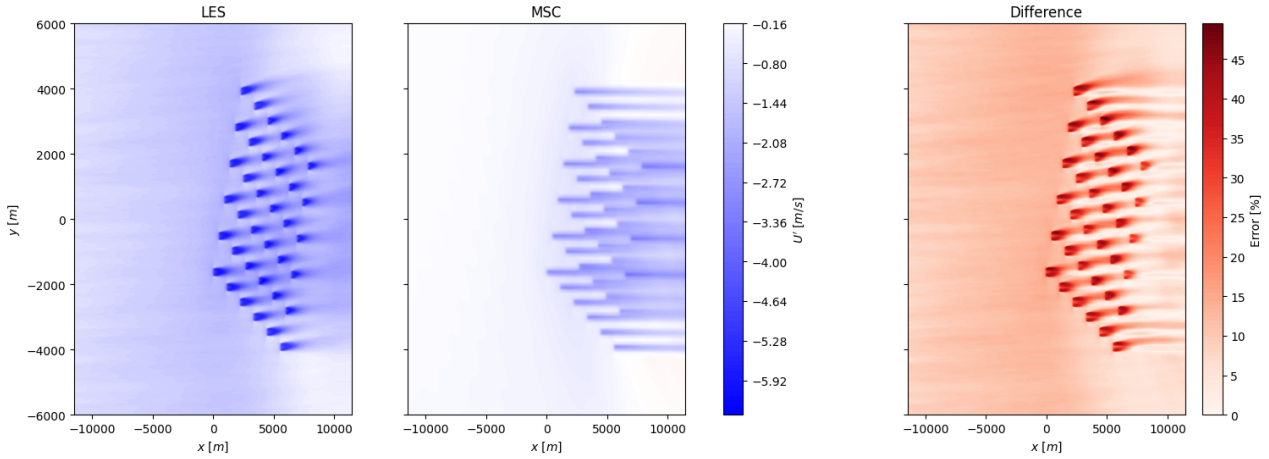

Figure C.11: Comparison of the LES and MSC streamwise perturbation velocity fields together with the percentual difference, which is scaled with the reference velocity, for simulation SFSNU2LES and SFSNU2MSC respectively, which have a square farm with a power density of $15\,\mathrm{MW\,km^{-2}}$.

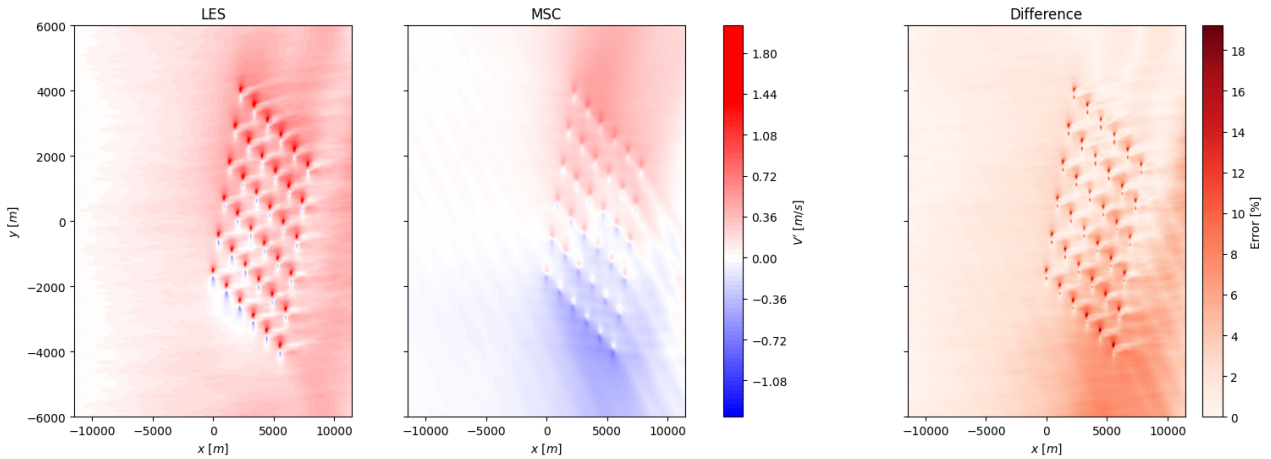

Figure C.12: Comparison of the LES and MSC spanwise velocity fields together with the percentual difference, which is scaled with the reference velocity, for simulation SFSNU2LES and SFSNU2MSC respectively, which have a square farm with a power density of $15\,\mathrm{MW\,km^{-2}}$.

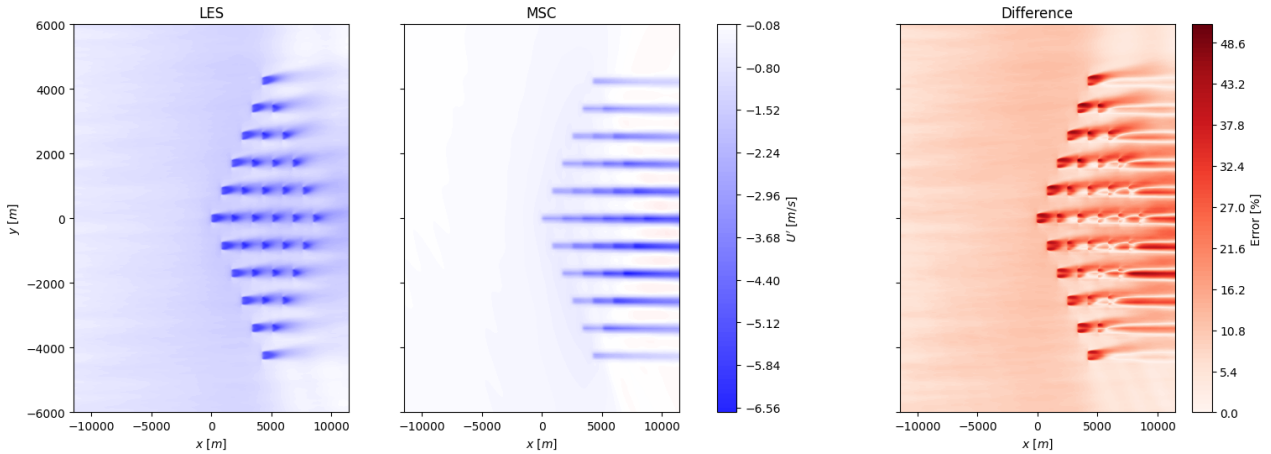

Figure C.13: Comparison of the LES and MSC streamwise perturbation velocity fields together with the percentual difference, which is scaled with the reference velocity, for simulation SFSNU3LES and SFSNU3MSC respectively, which have a square farm with a power density of $15\,\mathrm{MW\,km^{-2}}$.

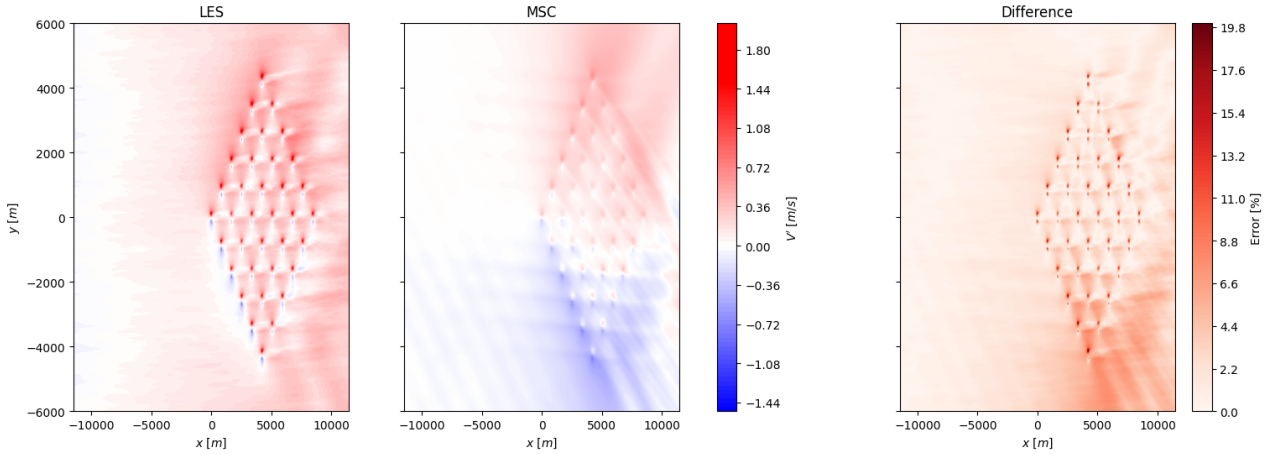

Figure C.14: Comparison of the LES and MSC spanwise velocity fields together with the percentual difference, which is scaled with the reference velocity, for simulation SFSNU3LES and SFSNU3MSC respectively, which have a square farm with a power density of $15\,\mathrm{MW\,km^{-2}}$.

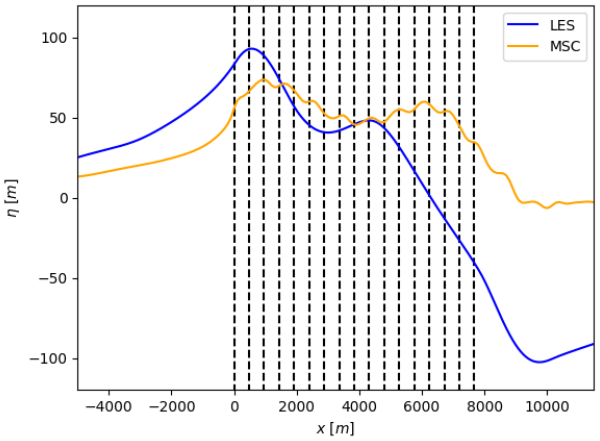

Figure C.15: Comparison of the LES and MSC atmospheric boundary layer displacement together with the percentual difference, which is scaled with the capping inversion height, for simulation PD1LES and PDL1MSC respectively, which have a square farm with a power density of $73\,\mathrm{MW\,km^{-2}}$. The turbine locations are indicated with dashed lines.

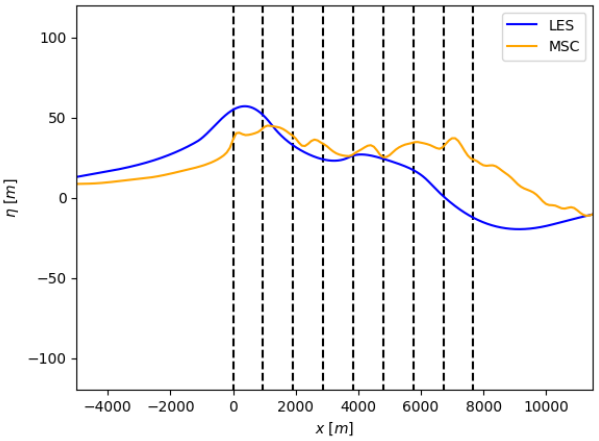

Figure C.16: Comparison of the LES and MSC atmospheric boundary layer displacement together with the percentual difference, which is scaled with the capping inversion height, for simulation PD2LES and PDL3MSC respectively, which have a square farm with a power density of $21\,\mathrm{MW\,km^{-2}}$. The turbine locations are indicated with dashed lines.

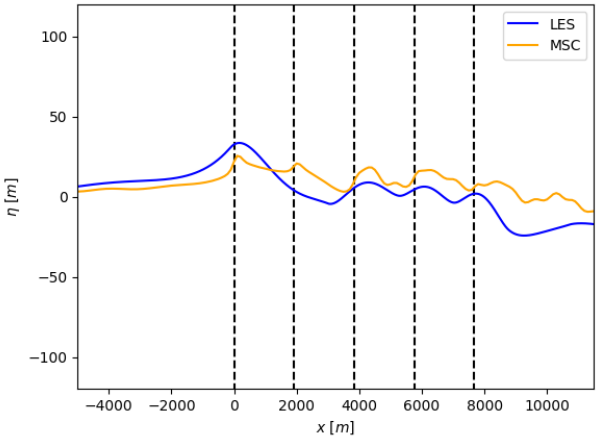

Figure C.17: Comparison of the LES and MSC atmospheric boundary layer displacement together with the percentual difference, which is scaled with the capping inversion height, for simulation PD3LES and PDL6MSC respectively, which have a square farm with a power density of $6\,\mathrm{MW\,km^{-2}}$. The turbine locations are indicated with dashed lines.

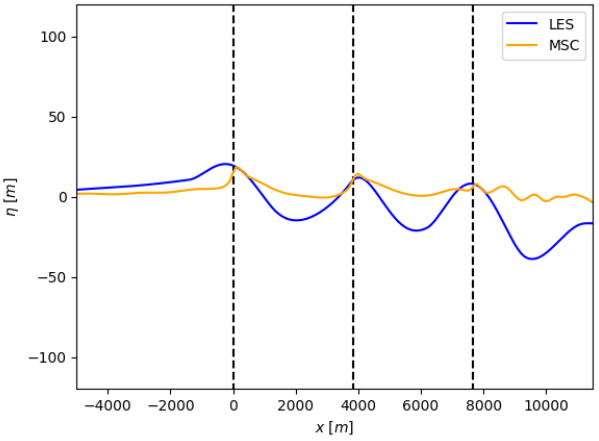

Figure C.18: Comparison of the LES and MSC atmospheric boundary layer displacement together with the percentual difference, which is scaled with the capping inversion height, for simulation PD4LES and PDL8MSC respectively, which have a square farm with a power density of $2\,\mathrm{MW\,km^{-2}}$. The turbine locations are indicated with dashed lines.

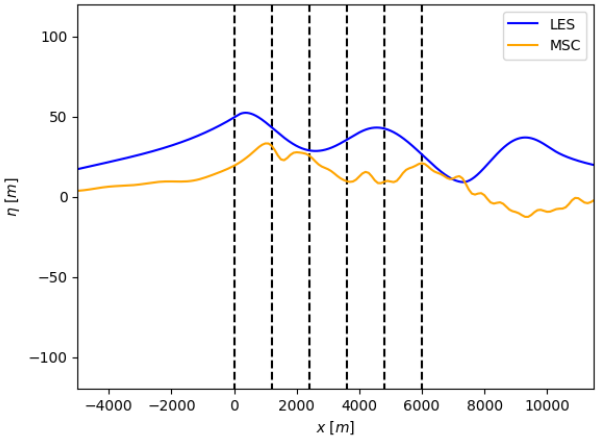

Figure C.19: Comparison of the LES and MSC atmospheric boundary layer displacement together with the percentual difference, which is scaled with the capping inversion height, for simulation SFSNU1LES and SFSNU1MSC respectively, which have a square farm with a power density of $15\,\mathrm{MW\,km^{-2}}$. The turbine locations are indicated with dashed lines.

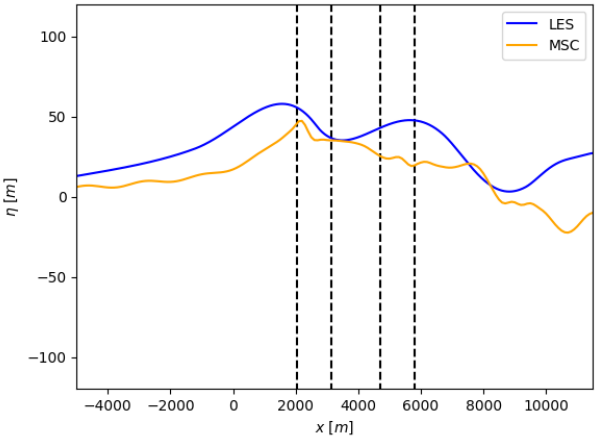

Figure C.20: Comparison of the LES and MSC atmospheric boundary layer displacement together with the percentual difference, which is scaled with the capping inversion height, for simulation SFSNU2LES and SFSNU2MSC respectively, which have a square farm with a power density of $15\,\mathrm{MW\,km^{-2}}$. The turbine locations of turbines that are located less than $500\,\mathrm{m}$ from the centerline are indicated with dashed lines.

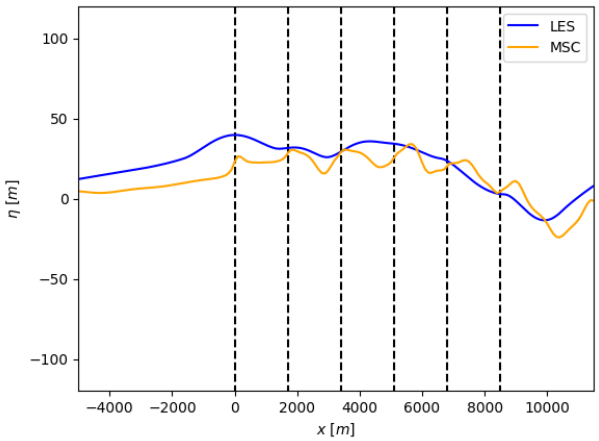

Figure C.21: Comparison of the LES and MSC atmospheric boundary layer displacement together with the percentual difference, which is scaled with the capping inversion height, for simulation SFSNU3LES and SFSNU3MSC respectively, which have a square farm with a power density of $15\,\mathrm{MW\,km^{-2}}$. The turbine locations of turbines that are located less than $500\,\mathrm{m}$ from the centerline are indicated with dashed lines.

Bibliography

Abkar, M., & Porté-Agel, F. (2015). Influence of atmospheric stability on wind-turbine wakes: A large-eddy simulation study. *Physics of fluids*, *27*(3).

Allaerts, D. (2016, November). *Large-eddy Simulation of Wind Farms in Conventionally Neutral and Stable Atmospheric Boundary Layers* [Doctoral dissertation].

Allaerts, D., Broucke, S. V., van Lipzig, N., & Meyers, J. (2018). Annual impact of wind-farm gravity waves on the Belgian–Dutch offshore wind-farm cluster. *Journal of Physics: Conference Series*, *1037*(7), 072006. https://doi.org/10.1088/1742-6596/1037/7/072006

Allaerts, D., & Meyers, J. (2015). Large eddy simulation of a large wind-turbine array in a conventionally neutral atmospheric boundary layer. *Physics of Fluids*, *27*(6).

Allaerts, D., & Meyers, J. (2016, January). Effect of Inversion-Layer Height and Coriolis Forces on Developing Wind-Farm Boundary Layers. In *34th Wind Energy Symposium*. American Institute of Aeronautics and Astronautics. https://doi.org/10.2514/6.2016-1989

Allaerts, D., & Meyers, J. (2017). Boundary-layer development and gravity waves in conventionally neutral wind farms. *Journal of Fluid Mechanics*, *814*, 95–130.

Allaerts, D., & Meyers, J. (2018). Gravity Waves and Wind-Farm Efficiency in Neutral and Stable Conditions. *Boundary-Layer Meteorology*, *166*(2), 269–299. https://doi.org/10.1007/s10546-017-0307-5

Allaerts, D., & Meyers, J. (2019). Sensitivity and feedback of wind-farm-induced gravity waves. *Journal of Fluid Mechanics*, *862*, 990–1028. https://doi.org/10.1017/jfm.2018.969

Archer, C. L., Vasel-Be-Hagh, A., Yan, C., Wu, S., Pan, Y., Brodie, J. F., & Maguire, A. E. (2018). Review and evaluation of wake loss models for wind energy applications. *Applied Energy*, *226*, 1187–1207. https://doi.org/10.1016/j.apenergy.2018.05.085

Baines, P. G. (1998). *Topographic Effects in Stratified Flows*. Cambridge University Press.

Barthelmie, R. J., Hansen, K., Frandsen, S. T., Rathmann, O., Schepers, J. G., Schlez, W., Phillips, J., Rados, K., Zervos, A., Politis, E. S., & Chaviaropoulos, P. K. (2009). Modelling and measuring flow and wind turbine wakes in large wind farms offshore. *Wind Energy*, *12*(5), 431–444. https://doi.org/10.1002/we.348

Birgin, E. G., Bustamante, L. H., Callisaya, H. F., & Martínez, J. M. (2013). Packing circles within ellipses. *International Transactions in Operational Research*, *20*(3), 365–389. https://doi.org/10.1111/itor.12006

Borrmann, R., Rehfeldt, K., Wallasch, A.-K., & Lüers, S. (2018, May). *Capacity Densities of European Offshore Wind Farms* (tech. rep.).

Bruyerre, P. (2022, December). *Retrofutur : Une autre histoire des machines à vent*.

Churchfield, M. J., Lee, S., Michalakes, J., & Moriarty, P. J. (2012). A numerical study of the effects of atmospheric and wake turbulence on wind turbine dynamics. *Journal of Turbulence*, *13*, N14. https://doi.org/10.1080/14685248.2012.668191

Churchfield, M. J., Lee, S., Moriarty, P., Martinez, L., Leonardi, S., Vijayakumar, G., & Brasseur, J. (2012, January). A Large-Eddy Simulation of Wind-Plant Aerodynamics. In *50th AIAA Aerospace Sciences Meeting including the New Horizons Forum and Aerospace Exposition*. American Institute of Aeronautics and Astronautics. https://doi.org/10.2514/6.2012-537

Davis, N. N., Badger, J., Hahmann, A. N., Hansen, B. O., Mortensen, N. G., Kelly, M., Larsén, X. G., Olsen, B. T., Floors, R., Lizcano, G., Casso, P., Lacave, O., Bosch, A., Bauwens, I., Knight, O. J., van Loon, A. P., Fox, R., Parvanyan, T., Hansen, S. B. K., … Drummond, R. (2023). The Global Wind Atlas: A High-Resolution Dataset of Climatologies and Associated Web-Based Application. https://doi.org/10.1175/BAMS-D-21-0075.1

Delft High Performance Computing Centre (DHPC). (2024). Delft Blue Supercomputer Phase 2.

Devesse, K., Lanzilao, L., Jamaer, S., Van Lipzig, N., & Meyers, J. (2022, February). Extending the applicability of a wind-farm gravity-wave model to vertically non-uniform atmospheres. https://doi.org/10.5194/wes-2021-138

Draxl, C., Worsnop, R. P., Xia, G., Pichugina, Y., Chand, D., Lundquist, J. K., Sharp, J., Wedam, G., Wilczak, J. M., & Berg, L. K. (2021). Mountain waves can impact wind power generation. *Wind Energy Science*, *6*(1), 45–60. https://doi.org/10.5194/wes-6-45-2021

Gaertner, E., Rinker, J., Sethuraman, L., Zahle, F., Anderson, B., Barter, G. E., Abbas, N. J., Meng, F., Bortolotti, P., Skrzypinski, W., Scott, G. N., Feil, R., Bredmose, H., Dykes, K., Shields, M., Allen, C., &

Viselli, A. (2020, March). *IEA Wind TCP Task 37: Definition of the IEA 15-Megawatt Offshore Reference Wind Turbine* (tech. rep. No. NREL/TP-5000-75698). National Renewable Energy Lab. (NREL), Golden, CO (United States). https://doi.org/10.2172/1603478

Germano, M., Piomelli, U., Moin, P., & Cabot, W. H. (1991). A dynamic subgrid-scale eddy viscosity model. *Physics of Fluids A: Fluid Dynamics*, *3*(7), 1760–1765. https://doi.org/10.1063/1.857955

Gill, A. E. (1982, December). *Atmosphere-Ocean Dynamics*. Elsevier Science.

Gossard, E. E., & Hooke, W. H. (1975). *Waves in the Atmosphere: Atmospheric Infrasound and Gravity Waves : Their Generation and Propagation*. Elsevier Scientific Publishing Company.

GWEC. (2023, August). Global Offshore Wind Report 2023.

Hartman, L. (2023). Wind Turbines: The Bigger, the Better.

Hess, G. D. (2004). The Neutral, Barotropic Planetary Boundary Layer, Capped by a Low-Level Inversion. *Boundary-Layer Meteorology*, *110*(3), 319–355. https://doi.org/10.1023/B:BOUN.0000007248.42321.d5

Interreg NorthSEE. (2020). Future Energy Industry Trends.

Johnstone, R., & Coleman, G. N. (2012). The turbulent Ekman boundary layer over an infinite wind-turbine array. *Journal of Wind Engineering and Industrial Aerodynamics*, *100*(1), 46–57. https://doi.org/10.1016/j.jweia.2011.11.002

Kainz, S., Quick, J., Souza de Alencar, M., Sanchez Perez Moreno, S., Dykes, K., Bay, C., Zaaijer, M. B., & Bortolotti, P. (2024, March). *IEA Wind TCP Task 55: The IEA Wind 740-10-MW Reference Offshore Wind Plants* (tech. rep. No. NREL/TP-5000-87923). National Renewable Energy Laboratory (NREL), Golden, CO (United States). https://doi.org/10.2172/2333634

Khan, M., Watson, S., Allaerts, D., & Churchfield, M. (2024). Recommendations on setup in simulating atmospheric gravity waves under conventionally neutral boundary layer conditions. *Journal of Physics: Conference Series*, *2767*, 092042. https://doi.org/10.1088/1742-6596/2767/9/092042

Khan, M. A., Allaerts, D., Watson, S., & Churchfield, M. (2024, March). Investigating the Relationship between Simulation Parameters and Flow Variables in Simulating Atmospheric Gravity Waves in Wind Energy Applications.

Klemp, J. B., & Lilly, D. K. (1978). Numerical Simulation of Hydrostatic Mountain Waves.

Lanzilao, L., & Meyers, J. (2024). A parametric large-eddy simulation study of wind-farm blockage and gravity waves in conventionally neutral boundary layers. *Journal of Fluid Mechanics*, *979*, A54. https://doi.org/10.1017/jfm.2023.1088

Lanzilao, L., & Meyers, J. (2021). Set-point optimization in wind farms to mitigate effects of flow blockage induced by atmospheric gravity waves. *Wind Energy Science*, *6*(1), 247–271. https://doi.org/10.5194/wes-6-247-2021

Lanzilao, L., & Meyers, J. (2022a). A new wake-merging method for wind-farm power prediction in the presence of heterogeneous background velocity fields. *Wind Energy*, *25*(2), 237–259. https://doi.org/10.1002/we.2669

Lanzilao, L., & Meyers, J. (2022b). Effects of self-induced gravity waves on finite wind-farm operations using a large-eddy simulation framework. *Journal of Physics: Conference Series*, *2265*(2), 022043. https://doi.org/10.1088/1742-6596/2265/2/022043

Lanzilao, L., & Meyers, J. (2023). An Improved Fringe-Region Technique for the Representation of Gravity Waves in Large Eddy Simulation with Application to Wind Farms. *Boundary-Layer Meteorology*, *186*(3), 567–593. https://doi.org/10.1007/s10546-022-00772-z

Lilly, D. K. (1992). A proposed modification of the Germano subgrid-scale closure method. *Physics of Fluids A: Fluid Dynamics*, *4*(3), 633–635. https://doi.org/10.1063/1.858280

Lubachevsky, B. D., & Graham, R. L. (1997). Curved Hexagonal Packings of Equal Disks in a Circle. *Discrete & Computational Geometry*, *18*(2), 179–194. https://doi.org/10.1007/PL00009314

Marek, P., Grey, T., & Hay, A. (2016). A study of the variation in offshore turbulence intensity around the British Isles.

Mehta, D., van Zuijlen, A. H., Koren, B., Holierhoek, J. G., & Bijl, H. (2014). Large Eddy Simulation of wind farm aerodynamics: A review. *Journal of Wind Engineering and Industrial Aerodynamics*, *133*, 1–17. https://doi.org/10.1016/j.jweia.2014.07.002

Meneveau, C., Lund, T. S., & Cabot, W. H. (1996). A Lagrangian dynamic subgrid-scale model of turbulence. *Journal of Fluid Mechanics*, *319*, 353–385. https://doi.org/10.1017/S0022112096007379

Monin, A. S., & Obukhov, A. M. (1954). Basic laws of turbulent mixing in the surface layer of the atmosphere. *24*(151), 163–187.

Munters, W., Meneveau, C., & Meyers, J. (2016). Shifted periodic boundary conditions for simulations of wall-bounded turbulent flows. *Physics of Fluids*, *28*(2), 025112. https://doi.org/10.1063/1.4941912

Nappo, C. J. (2013). *An Introduction to Atmospheric Gravity Waves*. Academic Press.

Netherlands Wind Energy Association. (2023). The North Seas Standard: enable growth with wind turbine standardization.

Nieuwstadt, F. T. M. (1983). On the solution of the stationary, baroclinic Ekman-layer equations with a finite boundary-layer height. *Boundary-Layer Meteorology*, *26*(4), 377–390. https://doi.org/10.1007/BF00119534

NREL. (2024). Offshore Wind.

Ollier, S. J., Watson, S. J., & Montavon, C. (2018). Atmospheric gravity wave impacts on an offshore wind farm. *Journal of Physics: Conference Series*, *1037*(7), 072050. https://doi.org/10.1088/1742-6596/1037/7/072050

Ollier, S. (2022, November). *Trapped lee wave interactions with an offshore wind farm* [Thesis]. Loughborough University. https://doi.org/10.26174/thesis.lboro.21583917.v1

Ollier, S. J., & Watson, S. J. (2023). Modelling the impact of trapped lee waves on offshore wind farm power output. *Wind Energy Science*, *8*(7), 1179–1200. https://doi.org/10.5194/wes-8-1179-2023

Ørsted. (2019). Making green energy affordable How the offshore wind energy industry matured – and what we can learn from it.

Panofsky, H. A. (1963). Determination of stress from wind and temperature measurements. *Quarterly Journal of the Royal Meteorological Society*, *89*(379), 85–94. https://doi.org/10.1002/qj.49708937906

Paulson, C. A. (1970). The Mathematical Representation of Wind Speed and Temperature Profiles in the Unstable Atmospheric Surface Layer.

Porté-Agel, F., Bastankhah, M., & Shamsoddin, S. (2020). Wind-Turbine and Wind-Farm Flows: A Review. *Boundary-Layer Meteorology*, *174*(1), 1–59. https://doi.org/10.1007/s10546-019-00473-0

Rampanelli, G., & Zardi, D. (2004). A Method to Determine the Capping Inversion of the Convective Boundary Layer. *Journal of Applied Meteorology and Climatology*, *43*(6), 925–933. https://doi.org/10.1175/1520-0450(2004)043<0925:AMTDTC>2.0.CO;2

Sachsperger, J., Serafin, S., & Grubišić, V. (2015). Lee Waves on the Boundary-Layer Inversion and Their Dependence on Free-Atmospheric Stability. *Frontiers in Earth Science*, *3*. https://doi.org/10.3389/feart.2015.00070

Sanchez Gomez, M., Lundquist, J. K., Mirocha, J. D., & Arthur, R. S. (2023). Investigating the physical mechanisms that modify wind plant blockage in stable boundary layers. *Wind Energy Science*, *8*(7), 1049–1069. https://doi.org/10.5194/wes-8-1049-2023

Shaw, W. J., Berg, L. K., Debnath, M., Deskos, G., Draxl, C., Ghate, V. P., Hasager, C. B., Kotamarthi, R., Mirocha, J. D., Muradyan, P., Pringle, W. J., Turner, D. D., & Wilczak, J. M. (2022). Scientific challenges to characterizing the wind resource in the marine atmospheric boundary layer. *Wind Energy Science*, *7*(6), 2307–2334. https://doi.org/10.5194/wes-7-2307-2022

Smith, R. B. (2010). Gravity wave effects on wind farm efficiency. *Wind Energy*, *13*(5), 449–458. https://doi.org/10.1002/we.366

Smith, R. B. (2022). A Linear Theory of Wind Farm Efficiency and Interaction. *Journal of the Atmospheric Sciences*, *79*(7), 2001–2010. https://doi.org/10.1175/JAS-D-22-0009.1

Stevens, R., Gayme, D., & Meneveau, C. (2013). Effect of turbine placement on the average power output of finite length wind farms. *International conference on aerodynamics of offshore wind energy systems and wakes (ICOWES2013)*.

Stipa, S. (2024). *Development of high and low fidelity models for wind farm - atmospheric boundary layer interaction* [Doctoral dissertation, University of British Columbia]. https://doi.org/10.14288/1.0442080

Stipa, S., Ahmed Khan, M., Allaerts, D., & Brinkerhoff, J. (2024). An LES Model for Wind Farm-Induced Atmospheric Gravity Wave Effects Inside Conventionally Neutral Boundary Layers. *Wind Energy Science Discussions*, 1–22. https://doi.org/10.5194/wes-2023-171

Stipa, S., Ajay, A., Allaerts, D., & Brinkerhoff, J. (2024a). TOSCA – an open-source, finite-volume, large-eddy simulation (LES) environment for wind farm flows. *Wind Energy Science*, *9*(2), 297–320. https://doi.org/10.5194/wes-9-297-2024

Stipa, S., Ajay, A., Allaerts, D., & Brinkerhoff, J. (2024b). The multi-scale coupled model: A new framework capturing wind farm–atmosphere interaction and global blockage effects. *Wind Energy Science*, *9*(5), 1123–1152. https://doi.org/10.5194/wes-9-1123-2024

Strickland, J. M. I., Gadde, S. N., & Stevens, R. J. A. M. (2022). Wind farm blockage in a stable atmospheric boundary layer. *Renewable Energy*, *197*, 50–58. https://doi.org/10.1016/j.renene.2022.07.108

Stull, R. B. (Ed.). (1988). *An Introduction to Boundary Layer Meteorology*. Springer Netherlands. https://doi.org/10.1007/978-94-009-3027-8

Sutherland, B. R. (2010, September). *Internal Gravity Waves*. Cambridge University Press.

Taylor, P. K., & Yelland, M. J. (2001). The Dependence of Sea Surface Roughness on the Height and Steepness of the Waves. *Journal of Physical Oceanography*, *31*(2), 572–590. https://doi.org/10.1175/1520-0485(2001)031<0572:TDOSSR>2.0.CO;2

UNFCCC secretariat. (2023, November). *Nationally determined contributions under the Paris Agreement* (tech. rep.).

University of Massachusetts Amherst. (2023). Wind Energy Center Alumni | Wind Energy Center.

Wilcox, D. C. (2006, November). *Turbulence Modeling for CFD* (3rd edition). D C W Industries.

Wu, K. L., & Porté-Agel, F. (2017). Flow Adjustment Inside and Around Large Finite-Size Wind Farms. *Energies*, *10*(12), 2164. https://doi.org/10.3390/en10122164

Zaaijer, M., & Viré, A. (2023, September). Introduction to wind turbines - Reader.

Zhang, M., & Stevens, R. J. A. M. (2018). Exploring a better turbine layout in vertically staggered wind farms. *Journal of Physics: Conference Series*, *1037*(7), 072041. https://doi.org/10.1088/1742-6596/1037/7/072041

Zilitinkevich, S. S., & Esau, I. N. (2002). On Integral Measures Of The Neutral Barotropic Planetary Boundary Layer. *Boundary-Layer Meteorology*, *104*(3), 371–379. https://doi.org/10.1023/A:1016540808958